CENTRO DE INVESTIGACIÓN Y DE ESTUDIOS AVANZADOS DEL INSTITUTO POLITÉCNICO NACIONAL

UNIDAD ZACATENCO

PROGRAMA DE DOCTORADO

NANOCIENCIAS Y NANOTECNOLOGÍA

Procesamiento de nanopartículas y películas delgadas de Cu_2ZnSnS_4 obtenidas por métodos químicos

Tesis que presenta:

Aruna Devi Rasu Chettiar

Para obtener el grado de:

Doctor en Ciencias

En la especialidad de

Nanociencias y Nanotecnología

Director de tesis: **Dr. Velumani Subramaniam**

México, Distrito Federal. Marzo, 2017

Resumen

Para resolver la crisis energética y la contaminación ambiental, es necesario desarrollar materiales fotovoltaicos (FV) que sean rentables, abundantes y con una alta eficiencia de conversión de energía. Los dispositivos fotovoltaicos de película delgada han sido atractivos debido a su bajo costo de manufactura, dado que requiere poco espesor (~ 1 a 2.5micras). Actualmente, los materiales absorbentes de CdTe y Cu (In, Ga) Se_2 (CIGS) son los materiales más utilizados en dispositivos fotovoltaicos de película delgada. Sin embargo, la participación de estas tecnologías en el mercado está limitada debido a la toxicidad del Cd y a la escasez de metales tales como el Te, Ga e In. Para superar estas dificultades, el material absorbente a base de zinc, cobre, estaño y azufre (Cu_2ZnSnS_4 ó CZTS) ha surgido como una tecnología prometedora dado que está compuesto de elementos abundantes, menos tóxicos y de bajo costo.

Recientemente la eficiencia más alta (12.6%) de los dispositivos fotovoltaicos PV de película delgada basados en CZTS se ha logrado utilizando un enfoque basado en la hidracina. Sin embargo, este método no es adecuado para la fabricación a gran escala porque la preparación de la solución del precursor de la hidracina debe ser preparada en una caja con ambiente de nitrógeno para evitar el peligro de una reacción, por la naturaleza altamente tóxica e inestable de la hidracina. Por lo tanto, con el objetivo de minimizar la toxicidad, hemos desarrollado un método para preparar películas de CZTS basadas en nanopartículas sintetizadas por el método de soluciones, no utiliza ningún solvente tóxico como la hidracina. Recientemente, la síntesis basada en nanopartículas ha demostrado la eficiencia del poder de conversión de las celdas solares hasta un 9.0% empleando solventes relativamente benignos con el medio ambiente.

El objetivo del presente trabajo de investigación es preparar películas de CZTS usando tintas basadas en nanopartículas (Nps). En este trabajo,

sintetizamos Nps de CZTS basándonos en dos enfoques diferentes, a saber, calentamiento e inyección caliente. Utilizando el enfoque de calentamiento, las Nps de CZTS se sintetizaron a una temperatura de reacción relativamente baja (220^{o}C) usando un único disolvente. En lo que respecta a nuestra búsqueda en la literatura, no existe un reporte de síntesis a baja temperatura de la fase pura de Nps de kesterita CZTS usando un único disolvente con el enfoque de calentamiento. En este enfoque, se sintetizaron Nps de CZTS estequiométricas y fuera de la estequiometría (pobre en Cu, rica en Zn). Además, se investigó la influencia de los parámetros de reacción tales como la temperatura y el tiempo de síntesis de las Nps estequiométricas, mediante una caracterización estructural, morfológica, de composición y propiedades ópticas. Además, basándose en la evolución dependiente del tiempo, se propone el mecanismo de crecimiento plausible para la formación de Nps de CZTS. De las diversas propiedades, percibimos que ambos, temperatura de reacción y tiempo, juegan un papel determinante para alcanzar la fase pura de Nps de kesterita CZTS con composición y morfología controlada. Entonces, la condición optimizada de 220^{o}C durante 4 h, se utilizó para sintetizar Nps de CZTS (pobre en Cu, rica en Zn), que mejora la eficiencia de los dispositivos fotovoltaicos. Posteriormente, las Nps se dispersan en hexanotiol para depositar películas delgadas por el método del doctor blade. Las películas son recocidas bajo condiciones atmosféricas para evaporar el disolvente y el carbono en la película. Por otra parte, las películas son recocidas bajo una atmósfera de argón/selenio para mejorar sus propiedades. Las películas selenizadas (CZTSSe) exhibieron una mejor movilidad y fotoconductividad, en comparación con la película recocida, esto debido a un incremento en el tamaño de grano. Después de la selenización, el ancho de banda prohibida se reduce de 1.5 hasta 1.09 eV, debido a la sustitución de átomos de azufre por átomos de selenio.

Utilizando el enfoque de inyección caliente, se sintetizaron Nps de CZTS pobres en Cu, ricas en Zn. Además, se modificaron los parámetros de

reacción tales como la temperatura y el tiempo, para estudiar sus influencias sobre las propiedades estructurales, morfológicas, composicionales y ópticas. Basándose en los experimentos dependientes del tiempo, se propone el mecanismo de crecimiento, el cual reveló que la fase evolucionó de Cu_2S al compuesto intermedio Cu_2SnS_3 y a la kesterita CZTS. Además, la tinta de CZTS se formuló usando las Nps sintetizadas, y las películas delgadas se depositaron por el método del doctor blade. En consecuencia, los procesos de recocido y selenización se llevan a cabo para mejorar las propiedades de las películas. Las películas selenizadas revelaron una mejora en la fotoconductividad, en comparación con las películas recocidas. A partir de los resultados, se concluye que las películas preparadas a partir del método de calentamiento demostraron una fotoconductividad mejorada en comparación con las películas obtenidas por inyección caliente. Además, el enfoque de calentamiento es adecuado para la aplicación a gran escala. Por lo tanto, las películas de CZTS selenizadas se pueden emplear como una capa absorbente en los dispositivos fotovoltaicos basados en película delgada de bajo costo.

Palabras clave: CZTS, nanopartículas, calentamiento, inyección caliente, película delgada, doctor blade, CZTSSe, bajo costo.

Abstract

To resolve the energy crisis and an environmental pollution, it is necessary to develop high conversion efficiency photovoltaic devices (PV) based on absorber materials which are cost-effective and earth abundant. Thin film PV devices have gained much attraction due to their low manufacturing cost as it requires low material usage (thicknesses in the range of ~1 to 2.5 μm). Currently, CdTe and Cu(In, Ga)Se_2 (CIGS) are the most important absorber materials in thin film PV devices. However, their shares in the PV market are limited because of the toxicity of Cd and scarcity of metals like Te, Ga, and In. To overcome this difficulty, PV device based on copper zinc tin sulfide (Cu_2ZnSnS_4 or CZTS) emerges as a promising absorber material and it is composed of abundant, non-toxic and inexpensive elements.

Recently, the highest efficiency (12.6%) of CZTS based thin film PV devices has been achieved using hydrazine-based approach. Nevertheless, this approach is not suitable for large-scale fabrication because the preparation of hydrazine precursor solution needs to be performed in a nitrogen-filled glove box to avoid the danger of the reaction as hydrazine is highly toxic and hazardously unstable. In contrast, nanoparticles synthesized by a solution process doesn't use any toxic solvents like hydrazine. Recently, nanoparticles based approach demonstrated the power conversion efficiency of the solar cell as high as 9.0% using relatively environmental benign solvents.

The aim of the present work is to prepare CZTS films using nanoparticles (Nps) based ink. Herein, we synthesize CZTS Nps by two different approaches, namely heating-up and hot-injection. Using heating-up approach, CZTS Nps were synthesized at relatively low reaction temperature (220˚C) using a single solvent. To the best of our knowledge, there is no report for low-temperature synthesis of pure phase kesterite CZTS Nps using a single solvent with the heating-up approach. In this approach, CZTS Nps were synthesized with

stoichiometric and off-stoichiometric (Cu-poor, Zn-rich) composition. Besides, the influence of reaction parameters such as temperature and time on the synthesis of stoichiometric Nps are investigated by examining their structural, morphological, compositional and optical properties. Furthermore, based on the detailed time-dependent evolution, plausible growth mechanism is proposed for the formation of CZTS Nps. From the various properties, we perceive that both, reaction temperature and time, play a determining role to attain pure phase kesterite CZTS Nps with controlled composition and morphology. Then, the optimized condition of 220˚C for 4 h, was used to synthesize Cu-poor, Zn-rich composition of CZTS Nps which enhances the efficiency of the CZTS solar cell. Subsequently, the Nps are dispersed in hexanethiol to be deposited as thin films by doctor blade method. The films are annealed under the atmospheric condition to evaporate the solvent and carbon in the film. Furthermore, annealed films are selenized under argon/selenium atmosphere to enhance their properties. The selenized films (CZTSSe) exhibited better mobility and photoconductivity, as compared to annealed film, due to an increment in the grain size. After selenization, the band gap is decreased from 1.5 to 1.09 eV, due to the replacement of sulfur atoms by selenium atoms.

Using hot-injection approach, Cu-poor, Zn-rich composition of CZTS Nps were synthesized. Moreover, the reaction parameters such as temperature and time are varied to study their influences on the structural, morphological, compositional and optical properties. Based on the time-dependent experiments, growth mechanism is proposed, which revealed that the compositional phase evolved from Cu_2S through the Cu_2SnS_3 intermediate compound to kesterite CZTS Nps. Furthermore, CZTS ink is formulated using synthesized Nps, and thin films are deposited by doctor blade method. Consequently, annealing and selenization processes are carried out to improve the film properties. Selenized film revealed an improvement in the photoconductivity as compared to annealed film. From the result, we conclude that films prepared from heating-up method

demonstrated enhanced photoconductivity than the films obtained by hot-injection-approach. Furthermore, the heating-up approach is well suitable for large area application. Hence, the selenized CZTS film will be employed as an absorber layer in low-cost thin film solar cell.

Keywords: CZTS, nanoparticles, heating-up, hot-injection, thin film, doctor-blade, CZTSSe, low-cost.

Acknowledgement

Sometimes I look back at these last four years of graduate school, it is a great fortune for me to be able to work as a student in Center for Research and Advanced Studies of the National Polytechnic Institute (CINVESTAV-IPN), were I managed to channel the energy, intellect, and support of everyone around me into a coherent curriculum vitae, in the process of doing my PhD.

This thesis is a culmination of a perfect working relationship with my supervisor, Prof. Dr. Velumani Subramaniam, to whom I am eternally grateful. He provided unreserved support during my PhD and generously paved the way for my development as a research scientist. Perhaps most importantly, for the comments and suggestions during every meeting, for spending time on discussion and helpful suggestions with me throughout this work on my thesis.

I would like to acknowledge and express my sincere gratitude to the committee members: Dra. María de la Luz Olvera Amador, Dr. Mauricio López Ortega, Dr. Arturo Maldonado Alvarez, from Solid State Electronics Section (SEES), Department of Electrical Engineering, CINVESTAV-IPN and external examiner Dr. Jose Chavez Carvayar, IIM-UNAM, Mexico City for their support, valuable time spent for in-depth study of my thesis and providing a suitable comments and suggestions which improved the quality of the thesis.

I am thankful to Nanoscience and Nanotechnology program coordinator Dr. Jose Gerardo Cabanas Moreno, for his support. And also thank program secretaries especially Alma Mercedes Zamudio Martínez, Jessica Marquez Duenas, María Ofelia Muñoz Ramírez for their continuous assistance.

Many others have contributed to the scientific content of this thesis. I want to thank Dr. Osvaldo Vigil-Galán, Dr. Fabián Andrés Pulgarín Agudelo and Ms.Miriam Nicolas Departamento de Física, Instituto Politécnico Nacional, Mexico for their valuable collaboration and contribution to use their selenization furnace.

I am also greatly indebted to the many people such as the professors and secretaries in various departments who in some way contributed to the progress and publication of the work contained herein. I really appreciate the collaborations of technicians, professors and auxillaries to work with them and helping in technical difficulties by characterizing and analysing the samples which made my work. Dr. Jaime Santoyo Salazar (Physics), Dr. Jorge Roque De La Puente (LANE, FESEM and EDS analysis), M. en I. Alvaro Ángeles Pascual, Dr. Daniel Bahena Urruibe (LANE, HRTEM analysis), Dr. Sergio Tomas (Physics, XPS analysis), M. en C. Miguel Galván Arellano (SEES, Raman spectroscopy and I-V measurement), Miguel Ángel Luna Arias (Hall Effect measurement), Ing. Angela Gabriela López Fabián (SEES, UV-Visible-NIR spectroscopy), M. en C. Adolfo Tavira Fuentes (SEES, XRD analysis), Miguel Luna (SEES, Thickness measurements), Norma Iris (SEES, Thermal evaporation of Au contacts), Josué Romero Ibarra (UNAM, FESEM) and Marcela Guerrero (Physics, XRD powder analysis).

Last and by no means the least, I am really grateful and thankful to the Consejo Nacional De Ciencia Y Tecnología (CONACYT) for providing me with a scholarship, CEMIE-Sol P26 for their financial support. And, I also thank Sistema de Información Académica (SINAC) from CINVESTAV-IPN for supporting financially to attend both national and international conferences like IMRC, Cancun and MRS, USA which made myself to realise the current status and advances in my field.

It's my pleasure to express my sincere gratitude to Mrs. Malathy Velumani for her continuous inspiration and care. I would also like to express my gratitude to my group members Dr. Pablo Itzam Reyes, Dr. Rohini Mohan, Dr. Goldie Oza, Dr. Victor Ishrayelu, M. en C. Latha Marasamy, M. en C. Ravichandren Manisekaren for sharing their precious experience, creating a lively and enjoyable workplace, and being truly remarkable friends. Special thanks to Dr. Pablo Itzam Reyes for his technical help. My deepest gratitude to

my best friend M. en C. Latha Marasamy, for being a constant presence during my many times of stress, excitement, frustration and celebration. Without her support, I couldn´t even imagine my Ph.D.

It is only right for me now to pay homage to my beloved parents for their overwhelming love, support and encouragement through all moments of my life. Thank you both for giving me the strength to chase my dream. My lovable siblings deserve my whole-hearted thanks as well.

Thank you all!

Contents

List of tables

List of figures

List of Acronyms/Abbreviations

Acronym	Definition of Acronym
PVs	Photovoltaics
Solar cell	Photovoltaic cell
mc-Si	Multicrystalline silicon
CdS	Cadmium sulfide
CdTe	Cadmium telluride
$CuInGaSe_2$ (CIGS)	Copper indium gallium diselenide
In	Indium
Te	Tellurium
TW	Terawatt
SSCs	Sensitized solar cells
Cu_2ZnSnS_4 (CZTS)	Copper zinc tin sulfide
V_{oc}	Open circuit voltage
J_{sc}	Short circuit current density
FF	Fill factor
η	Efficiency
ZnS	Zinc-blende
$CuInS_2$ (CIS)	Copper indium sulfide
ST	Stannite
KS	Kesterite
SnS	Tin sulfide
H_2S	Hydrogen sulfide
PCE	Power conversion efficiency
CVD	Chemical vapor deposition

PLD	Pulsed laser deposition
N_2	Nitrogen
KCN	Potassium cyanide
SLG	Soda lime glass
TEM	Transmission electron microscopy
I-V	Current-voltage
SLG	Soda lime glass
DI	De-ionized
S	Sulfur
Se	Selenium
CBD	Chemical bath deposition
XRD	X-ray diffraction
ICDD	International Center for Diffraction Data
JCPDS	Joint Committee on Powder Diffraction Standards
D	Crystallite size
FWHM	Full Width Half Maximum
FE-SEM	Field emission scanning electron microscopy
EDAX	Energy dispersive analysis of X-rays
TEM	Transmission electron microscopy
HR-TEM	High resolution transmission electron microscopy
HAADF-STEM	High-angle annular dark field scanning transmission electron microscopy
ADF	Annular dark field
µl	Micro litre
XPS	X –ray photoelectron spectroscopy
UV-Vis-NIR	Ultraviolet-visible-near infrared
t	Thickness

ρ	Resistivity
Nps	Nanoparticles

Chapter 1
Introduction

1.1. Need for renewable energy

Energy shortage and environment pollution have been the "bottle-necks" of development for the human society in this century. Therefore, new approaches that can generate energy in a sustainable way, have gradually gained the attention around the world. One of the best-known ways of achieving this, is by exploiting renewable energy resources. Renewable energy is an energy which can be obtained from natural resources that are continuously replenished, such as sunlight, wind, rain, tides, waves and geothermal heat. These energy sources have gained significant public interest as an alternative energy source for the future. Also, renewable energy sources produce energy from clean, sustainable resources such as solar radiation with less environmental impact. Another major benefit of using renewable energy sources is energy security and independence.

With renewable energy resources, energy is harvested from the source available at the site. An example of this is solar energy, where electricity is generated directly from the solar radiation incident on the panels.

1.2. Importance of solar energy

Current trends suggest solar energy will play a vital role in future energy production. Indeed, solar energy alone has the capacity to meet all the planet's energy needs for the foreseeable future. The sun deposits ~120,000 terawatt (TW) TW of electromagnetic radiation on the surface of the Earth, far exceeding human needs even in the most aggressive energy demand scenarios. Covering just 0.16 % of the land on Earth with 10 % efficient solar conversion systems [1] would provide 20 TW power, which is nearly twice the world's present consumption rate, Fig.1.1 of fossil energy (or equivalent of 20,000 1-GWe nuclear fission plants)

[2,3]. These comparisons illustrate the incredible magnitude of the solar resource, providing an energy stream far more potent than present-day human technology can achieve. A solar energy source provides pollution-free, self-contained, reliable, quiet, long-term, maintenance-free, and unlimited operation at moderate costs. The estimated world net renewable electricity generation by energy sources from 2010 to 2040 can be seen in Table 1.1. The table shows that electricity generation by solar energy will increase from 34 billion kilowatt-hours in 2010 to 452 billion kilowatt-hours in 2040 with an average annual percentage growth of 9.1 percent, which is the fastest growth rate when compared to other renewable energy resources. These figures indicate the large potential of solar energy to become one of the leading renewable sources in electricity generation.

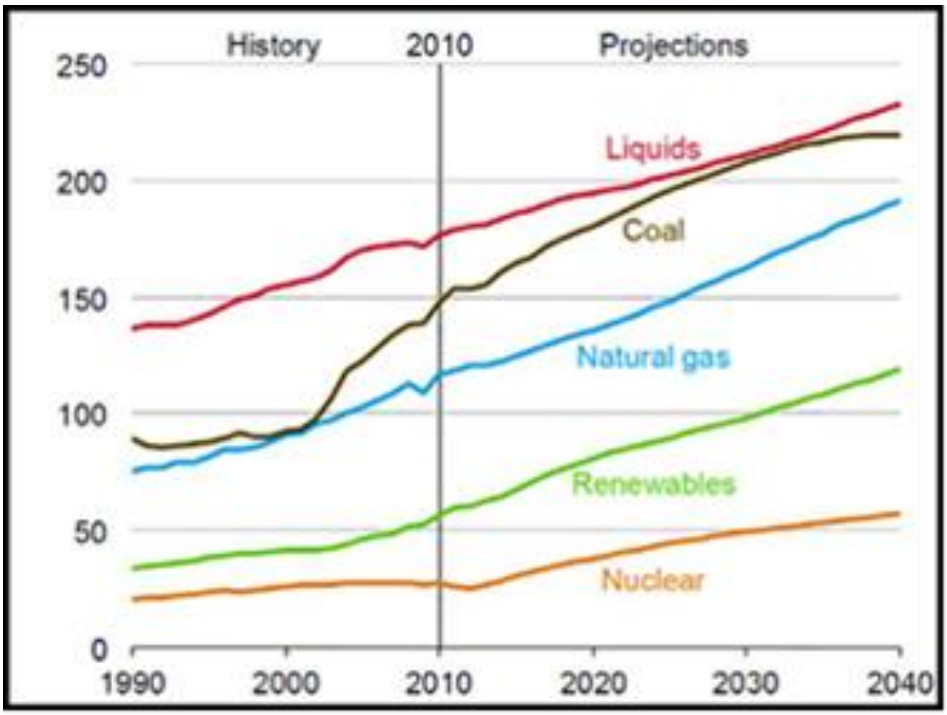

Fig.1.1. World energy consumption by fuel type, 1990-2040.

Table 1.1 World net renewable electricity generation by energy source, 2010-2040 (billion kilowatt-hours).

World	2010	2015	2020	2025	2030	2035	2040	Average annual percentage growth (%)
Hydroelectric	3402	3805	4452	4762	5177	5692	6232	2.0
Wind	342	767	1136	1383	1544	1694	1839	5.8
Geothermal	66	112	133	146	171	195	220	4.1
Solar	34	157	240	288	327	394	452	9.1
Other	332	427	549	643	729	800	858	3.2
Total	4175	5267	6509	7222	7948	8775	9601	2.8

1.3. Solar Photovoltaics

Solar photovoltaics (PVs) directly convert solar radiation to electricity through the excitation of electrons in a semiconductor material to generate electric current. Solar power has been increased rapidly with the increase in the installation capacity by 50% per year worldwide over the last decade. The power generated by PVs reached almost 100 TW in 2013. The total installed capacity of PV increased by 43%, reaching 29.4 GW in 2013, representing 15% of the total growth in the global power generation capacity (Fig.1.2) [4].

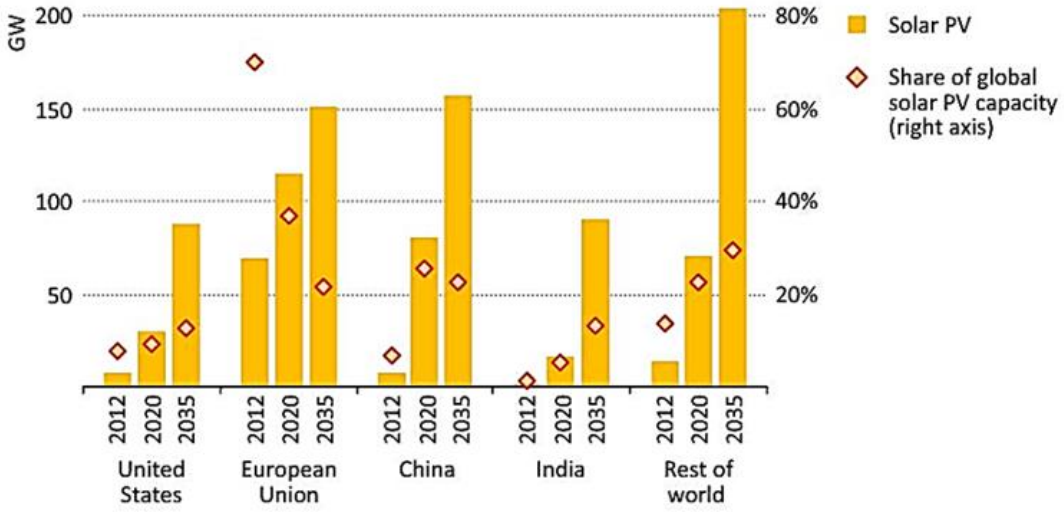

Fig. 1.2. Installed solar PV capacity by region in the New Policies Scenario.

1.4. Working principles of solar cells

A solar cell (also known as photovoltaic cell) is a device that converts light energy directly into electricity based on the photovoltaic effect, which was first observed by Alexandre-Edmond Becquerel in 1839 [5]. Its working principles as shown in Fig. 1.3 can be divided into four steps:

- First of all, a light absorbing material absorbs a photon, exciting an electron in absorber material from its ground state to an excited state.
- Second, an electron-hole charge carrier pair is generated, with the electron (negative charge carrier) in the conduction band and the hole (positive charge carrier) in the valence band (ground state).
- Then, the positive and negative charge carriers are separated and move towards opposite electrical contacts. After that, they travel through to reach the current collector of an external electrical circuit and do work at an electrical 'load'.
- Finally, the negative charge carriers arrive back at the absorber, where they recombine with the positive charge carrier and return to the ground state [6].

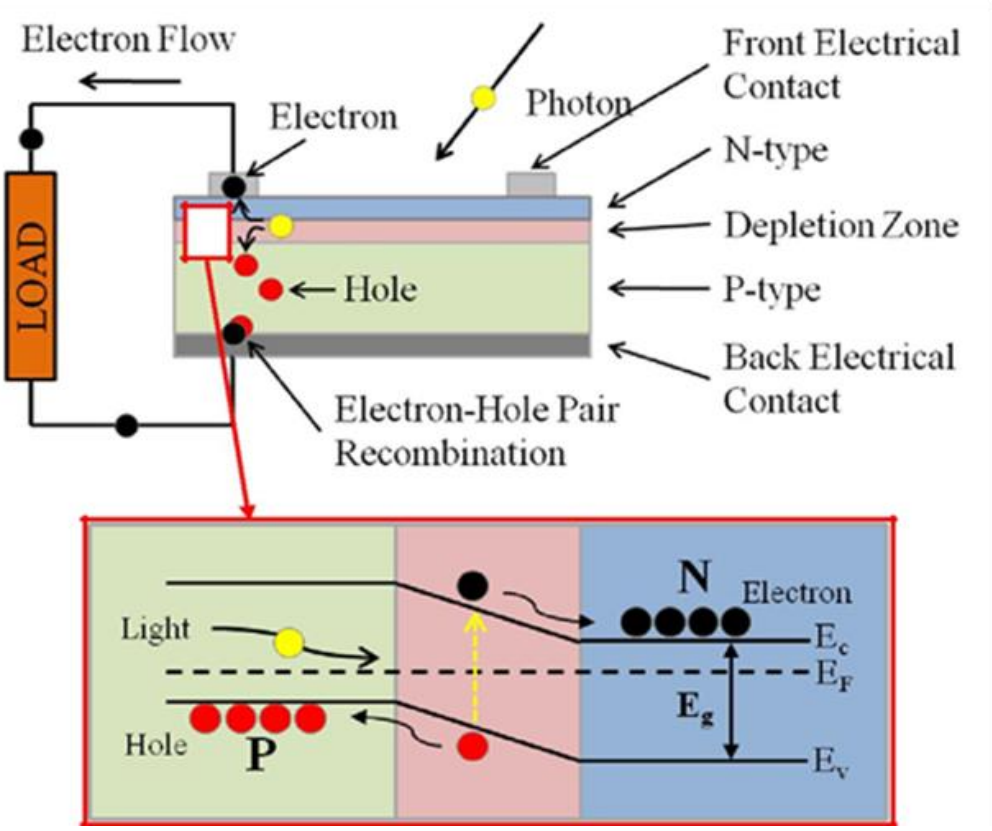

Fig.1.3. Diagram of a solar PV cell absorbing a photon and generating an electron-hole pair. Enlarged is the energy band diagram of a p-n junction.

1.5. Generation of solar cells

1.5.1. First generation solar cells

The first generation solar cells are based on monocrystalline and multicrystalline silicon, which is a semiconductor with an indirect energy bandgap of 1.12 eV [7]. The efficiency of the first reported (1941) solar cell based on multicrystalline silicon (mc-Si) was about 1% [8]. Over the years, the efficiency of Si solar cells evolved rapidly, approaching its theoretically predicted maximum of about 32% [9- 11]. Silicon-based PV is still the dominant technology in the solar field, accounting more than 90% of total production. However, the price of electricity produced by PV is still high as compared to other sources. One of the factors contributing to the high production cost of Si solar cells is the amount of material used. About 61% of the solar cell price is accounted by the Si

wafer [12, 13]. Due to the relatively small absorption coefficient of silicon (100 cm^{-1}), the device must have a thickness of about 100–200 μm to absorb most of the incident solar radiation and provide reasonable mechanical strength. Reducing the wafer thickness, less expensive material usage could be the solutions to decrease the cost of PV-produced energy [14-16].

1.5.2. Second generation solar cells

The second generation solar cells is based on thin-film technology. It has emerged as an alternative to the conventional Si cells. Thin-film PV provides a solution to reduce the amount of material used by employing direct-bandgap semiconductors with higher absorption coefficients. Thus, the total thickness of the solar cell is in the range of a few microns. The device is fabricated on inexpensive substrates (e.g., glass, plastic, metal foils) to provide the necessary mechanical strength. Moreover, the synthesis process does not require a high degree of purity, unlike the case of Si cells.

Therefore, the synthesis process of thin-film PV devices using different kinds of deposition methods is simpler and less expensive. Thin-film solar cells are based generally on heterojunctions using differently doped, dissimilar materials. A thin n-type semiconductor as a buffer layer is deposited on top of a p-type semiconductor, to form the p-n junction. A p-type material is preferred for the active absorbing layer, where the electron-hole pairs are generated. The diffusion length of electrons in a p- type semiconductor is larger than the diffusion length of holes in an n-type semiconductor. The n-type layer must be thin and made of a wide-band material to enable the incident light to pass through to the absorber layer. For that, a cadmium sulfide (CdS) layer about 50 μm thickness with an energy bandgap of 2.4 eV is commonly used [17-19].

Cadmium telluride (CdTe) and copper indium-gallium diselenide, $Cu(InGe)Se_2$ (CIGS) are two strong representative materials for thin-film solar cells that show device efficiencies comparable to those of mc-Si cells. CdTe has

long been recognized as an optimal candidate for thin-film PV applications because it is a chemically stable semiconductor compound with large absorption coefficient (>10^4 cm^{-1}) and a direct bandgap of about 1.45 eV [20, 21]. CIGS is a quaternary semiconductor absorber material and it exhibits direct bandgap and high optical absorption coefficient. The band gap can be tuned from 1.04 to 1.68 eV with varying In/Ga ratio [22]. Both materials have reached the commercialization stage for mass production.

Unfortunately, there are drawbacks to both of these technologies. Cadmium is toxic and there are issues around the potential scarcity, and consequent volatility in cost, of both indium (In) and tellurium (Te) [23]. This can be seen in Fig. 1.4, which shows that tellurium is about as scarce as gold. The world trading price of In and Ga is around $700/Kg and $1700/Kg at their peak demand, which imposes a serious concern on the production scale of PV technologies using these materials. To overcome the possible future effects of 'In' scarcity on TW-scale consumption, it has been projected that CIGS can be replaced by kesterite CZTS.

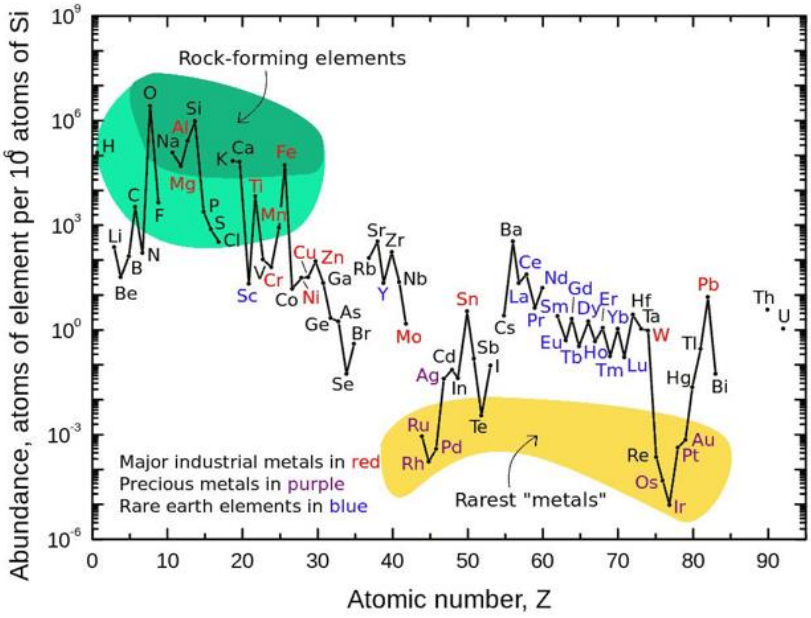

Fig. 1.4. Relative abundance of various elements in the earth's crust.

1.5.3. Third generation solar cells

Third generation solar cells have the feature of high power conversion efficiency and low cost. Therefore, abundance, availability of materials and the ease of processing for device fabrication become very important as they largely determine the production cost. Various advanced technologies and cutting-edge materials have been exploited for 3rd generation solar cells.

For example, solution-processed PV devices such as sensitized solar cells (SSCs), Cu_2ZnSnS_4 (CZTS) and polymer organic solar cells hold much promise owing to low cost fabrication. In particular, CZTS is considered as one of the most promising light absorber materials for the next generation thin film PV, due to low raw material cost and toxicity. The availability of copper, zinc, tin and sulfur in the earth's crust are 50, 75, 2.2 and 260 ppm respectively. All the constituents of CZTS are abundant in the earth's crust. It is expected to have a very promising future, although most of the work is still in the laboratory or testing stage [24-26].

Table 1.2 shows the different solar cells with efficiency.

Classification	η (%)	Area (cm^2)	Voc (V)	Jsc (mA/cm^2)	FF (%)	References
Si (crystalline)	25.1	4.0	0.706	42.70	82.8	27
CdTe	22.1	0.47	0.887	31.69	78.5	28
CIGS	22.6	0.50	0.741	37.8	80.6	29
CZTS	9.2	0.24	0.747	19.5	63.2	30
CZTSSe	12.6	0.42	0.513	35.21	69.8	31
Multi junction (GaAs) Solar cell	46.0	0.05	-	-	-	32

V_{oc} (Open circuit voltage); J_{sc} (Short circuit current density); FF (Fill factor); η (Efficiency).

1.6. Objectives of the thesis work

The main objectives of this thesis dissertation are summarized as below:

(i) Understanding the effect of key synthesis parameters on the formation of CZTS nanoparticles, are synthesized by two different approaches such as
   - Heating-up and
   - Hot-injection.

(ii) Formulation of CZTS ink using synthesized nanoparticles by two different approaches.

(iii) Deposition of CZTS films by doctor-blade method and study the properties of the films.

(iv) Performing the heat treatment (selenization) for CZTS films.

(v) Investigate the effect of selenization on the properties of CZTS films.

The effect of key reaction parameters including temperature, time are investigated in-detail to achieve better control over the phase pure, size, shape and composition of the nanoparticles. The growth and formation mechanism are proposed based on our research findings.

The concentration of ink was varied to accomplish the crack free CZTS films. Influence of selenization temperatures on the properties of the films were investigated.

1.7. Thesis Organization

This thesis is organized as below: **Chapter 1** provides an introduction to information on the needs of renewable energy in resolving the world energy crisis, and the advantages of solar photovoltaic over other types of renewable sources. This chapter contains the advantages of CZTS absorber material as well as the research objectives and thesis organization.

Chapter 2 describes the materials properties, deposition methods of CZTS films and the importance of present work.

Chapter 3 explains the experimental procedure for the CZTS nanoparticles synthesis, preparation of CZTS and CdS films. Besides, the principles of the characterization techniques used to analyze the nanoparticles and films are briefly described.

Chapter 4 presents the results of the CZTS nanoparticles prepared by heating-up process and discusses aspects of them in greater detail.

Chapter 5 elucidates the results and discussions of the properties of CZTS films obtained from the heating-up synthesis of CZTS nanoparticles.

Chapter 6 exhibits the results and discussions of hot-injection synthesis of CZTS nanoparticles.

Chapter 7 summarizes the highlights of the results.

References

[1] U. S. E. I. Administration, International Energy Outlook (2013), U.S. Department of Energy, Washington, DC.

[2] R. F. Service, Is it time to shoot for the sun? Science, 309 (2005), pp. 548–551.doi: 10.1126/science.309.5734.548.

[3] http://www.sc.doe.gov/bes/reports/files/SEU_rpt.pdf, Report of the Basic Energy Sciences Workshop on Solar Energy Utilization, US-DOE, April 18–21. 2005.

[4] O. Publishing and I. E. Agency, OECD Publishing, Paris, 2013.

[5] E. Becquerel, Mémoire sur les effets électriques produits sous 'influence des rayons solaires, Comptes Rendus, 9(1839), 561–567.

[6] J. S. Fonash, Solar Cell Device Physics, Elsevier printing press, Oxford, UK, 2nd edition, 2010.

[7] D. M. Chapin, C. S. Fuller, G. L. Pearson, A New Silicon p-n Junction Photocell for Converting Solar Radiation into Electrical Power, 25 (1954), 676 doi: 10.1063/1.1721711.

[8] M. A. Green, The path to 25% silicon solar cell efficiency: History of silicon cell evolution, Prog. Photovolt, 17 (2009), 183-189, doi: 10.1002/pip.892.

[9] K. Masuko, M. Shigematsu, T. Hashiguchi, D. Fujishima, M. Kai, N. Yoshimura, T. Yamanishi, Achievement of more than 25% conversion efficiency with crystalline silicon heterojunction solar cell, J. Photovolt, 4 (2014), 1433-1435 doi: 10.1109/jphotov.2014.2352151

[10] Trina Solar Announces New Efficiency Record of 21.25% Efficiency for Multicrystalline Silicon Solar Cell. (2015, November 9) Retrieved from http://www.trinasolar.com/us/about-us/newinfo_978.html.

[11] M. A. Green, K. Emery, Y. Hishikawa, W. Warta, E. D. Dunlop, Solar cell efficiency tables (Version 47). Prog. Photovolt, 24 (2015), 3-11, doi: 10.1002/pip.2728.

[12] International Technology Roadmap for Photovoltaic (ITRPV): Results 2015. (2016, March) Retrieved from http://www.itrpv.net/Reports/Downloads.

[13] R. W. Miles, K. M. Hynes, I. Forbes, Photovoltaic solar cells: An overview of state-of-the-art cell development and environmental issues, Prog. Photovolt, 51 (2005), 1-42, doi: 10.1016/j.pcrysgrow.2005.10.002.

[14] F. Meillaud, M. Boccard, G. Bugnon, M. Despeisse, S. Hänni, F. J Haug, C. Ballif, Recent advances and remaining challenges in thin-film silicon photovoltaic technology, Mat.Today, 18(2015), 378-384, doi: 10.1016/j.mattod.2015.03.002.

[15] D. E. Carlson, C. R. Wronski, Amorphous silicon solar cell. App.Phy. Letters, 28 (1976), 671-673, doi: http://dx.doi.org/10.1063/1.88617.

[16] D. L. Staebler, C. R. Wronski, Reversible conductivity changes in discharge- produced amorphous Si. App. Phy. Letters, 31(1977), 292-294 doi: 10.1063/1.89674.

[17] N. Romeo, A. Bosio, D. Menossi, A. Romeo, M. Aramini, Last Progress in CdTe/CdS Thin Film Solar Cell Fabrication Process. Ener. Proced, 57(2014), 65-72, http://dx.doi.org/10.1016/j.egypro.2014.10.009.

[18] J. Britt, C. Ferekides, Thin- film CdS/CdTe solar cell with 15.8% efficiency, Appl. Phy. Letters, 62(1993), 2851-2852, doi: 10.1063/1.109629.

[19] P. V. Meyers, Design of a thin film CdTe solar cell. Solar Cells, 23(1988), 59-67, http://dx.doi.org/10.1016/0379-6787(88)90007-5.

[20] Z. Bai, J. Yang, D. Wang, Thin film CdTe solar cells with an absorber layer thickness in micro-and sub-micrometer scale, Appl. Phy. Letters, 99(2011), 143502, doi: http://dx.doi.org/10.1063/1.3644160.

[21] N. Romeo, A. Bosio, A. Romeo, An innovative process suitable to produce high-efficiency CdTe/CdS thin-film modules, Solar. Ener. Mat. Solar Cells, 94 (2010), 2-7, http://dx.doi.org/10.1016/j.solmat.2009.06.001.

[22] K. Ramanathan, M.A. Contreras, C.L. Perkins, S. Asher, F.S Hasoon, J. Keane, D. Young, M. Romero, W. Metzger, R. Noufi, J. Ward, Properties of 19.2% efficiency ZnO/CdS/$CuInGaSe_2$ thin- film solar cells, Prog. Photovolt, 11 (2003), 225-230, doi: 10.1002/pip.494.

[23] C. Candelisea, J. F. Speirsa, J.K Robert, Materials availability for thin film (TF) PV technologies development: A real concern? Renewable and Sustainable Energy Reviews, 15 (2011), 4972–4981, doi: 10.1016/j.rser.2011.06.012.

[24] J. Paier, R. Asahi, A. Nagoya, G. Kresse, Cu_2ZnSnS_4 as a potential photovoltaic material: a hybrid Hartree-Fock density functional theory study, Phy. Rev B, 79(2009), 115126, doi: 10.1103/PhysRevB.79.115126.

[25] S. Schorr, H. J Hoebler, M. Tovar, (2007). A neutron diffraction study of the stannite-kesterite solid solution series. Eur.J.Mineralogy,19(2007), 65-73, doi: 10.1127/0935-1221/2007/0019-0065.

[26] C. Persson, Electronic and optical properties of Cu_2ZnSnS_4 and $Cu_2ZnSnSe_4$, J. Appl. Phy, 107(2010), 3710, doi: http://dx.doi.org/10.1063/1.3318468.

[27] K. Yamamoto, 25.1% efficiency Cu metallized heterojunction crystalline Si solar cell. 25th International Photovoltaic Science and Engineering Conference, Busan, Korea, November 2015.

[28] https://renewablesnow.com/news/first-solar-hits-efficiency-of-22-1-with-cdte-research-cell-514244/

[29] P. Jackson, R. Wuerz, D. Hariskos, E. Lotter, W. Witte, M. Powalla, Effects of heavy alkali elements in Cu(In,Ga)Se_2 solar cells with efficiencies up to 22.6%, Phys. Status Solidi RRL 10(2016) 583–586, doi:10.1002/pssr.201600199.

[30] K. Sun , C. Yan, F. Liu, J. Huang, F. Zhou, J. A. Stride, M. Green, X. Hao, Over 9% Effi cient Kesterite Cu_2ZnSnS_4 Solar Cell Fabricated by Using Zn_{1-}

$_x$Cd$_x$S Buffer Layer, Adv. Energy Mater. 6 (2016), 1600046, doi: 10.1002/aenm.201600046.

[31] W. Wang, M.T. Winkler, O. Gunawan, T. Gokmen, T. K. Todorov, Y. Zhu, D. B. Mitzi, Device Characteristics of CZTSSe Thin-Film Solar Cells with 12.6% Efficiency, Adv. Ener. Mater, 4(2014), doi: 10.1002/aenm.201301465.

[32] Press Release, Fraunhofer Institute for Solar Energy Systems, 1 December 2014 (accessed at on 7 December 2014).

[33] http://www.ise.fraunhofer.de/en/press-and-media/pressreleases/press-releases-2014/new-world-record-for-solar-cellefficiency-at-46-percent

Chapter 2
Material properties and deposition methods of CZTS Thin films

2.1. Material properties of CZTS

2.1.1 Structural properties

The quaternary compound Cu_2ZnSnS_4 can be derived from II-VI compounds such as zinc-blende (ZnS). By replacing two group-II atoms with one group-I and one group-III atoms, we obtain an I-III-VI_2 semiconductor such as the Cu-based chalcopyrite $CuInS_2$ (CIS). Then, by replacing half of the In atoms with group-II atoms such as Zn and the other half with group-IV atoms such as Sn, we can produce Cu_2ZnSnS_4 (CZTS). Similarly, the $Cu_2ZnSnSe_2$ compound can be derived from CuInSe. Fig. 2.1 illustrates the derivation of CZTS from ZnS.

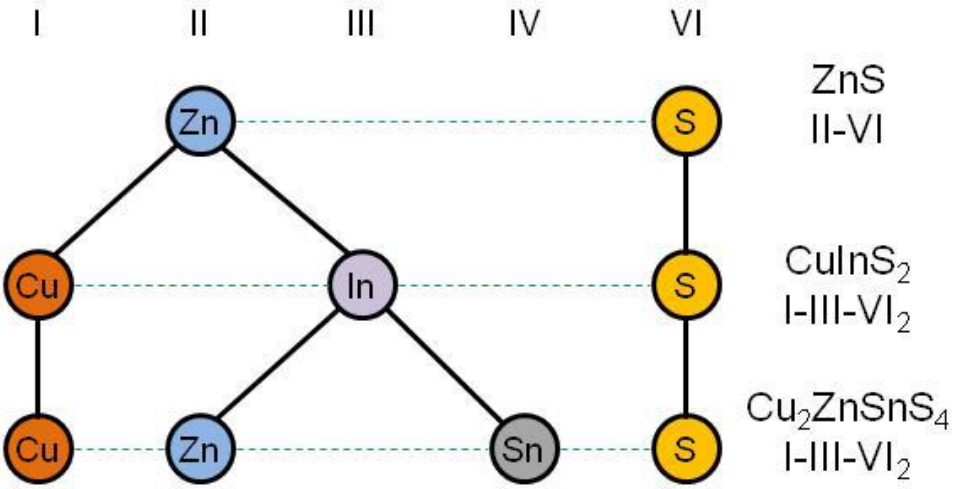

Fig. 2.1. Derivation of the quaternary CZTS compound from binary and ternary compounds.

Crystallographically, CZTS has two principal structures, known as stannite (ST) and kesterite (KS) type. These two structures are very similar except the different arrangements of 'Cu' and 'Zn' atoms (Fig.2.2). However, CZTS material usually appears in kesterite phase because it is thermodynamically more stable as compared to stannite type [1–4]. Washio et al. [5] investigated the relationship between composition and kesterite crystal structure of CZTS thin films. They choose three Cu/(Zn+Sn) composition ratios of about 1.2 (non-photovoltaic composition ratio), 1.0 (non-photovoltaic composition ratio), and 0.8 (photovoltaic composition ratio).

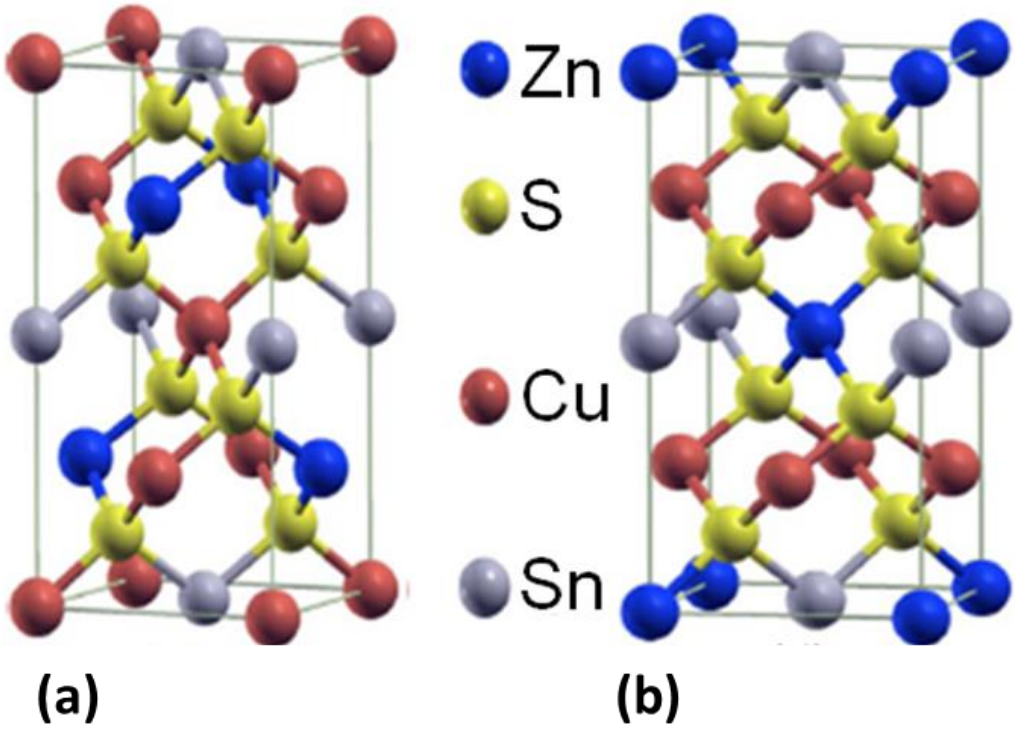

Fig. 2.2. CZTS unit cells of (a) kesterite-type and (b) stannite-type structures.

It was found that when Cu/Zn+Sn ratio is 0.8, 'Cu' substitutes for 'Zn' at the 2d site and/or 'Zn' substitutes for 'Cu' at the 2c site. They claimed that high performance of CZTS thin films in photovoltaic activity is due to the kesterite

crystal structure. Calculated and experimentally measured values for the lattice constant 'a' of the KS and ST tetragonal unit cells are on the order of 5.4 Å, whereas the ratio c/a is close to 2.

2.1.2. Phase diagram of CZTS

In the Cu_2ZnSnS_4 unit cell, one finds 2 Cu, 1 Zn, 1 Sn and 4 S atoms. If an absorber layer has the same elemental 2:1:1:4 composition ratio, or is close to this ratio, it is referred to as stoichiometric. Deviations from the 2:1:1:4 stoichiometry can lead to the formation of new unit cells with differing compositions. If one tracks the various formed unit cells as a function of composition, a so-called phase diagram is obtained. When growing compound materials, one major challenge lies in controlling the composition and staying in the stoichiometric area of the phase diagram. Deviations from stoichiometry can lead to the formation of unwanted phases with deviating composition and crystal structure. Alternatively, several phases with differing composition can co-exist.

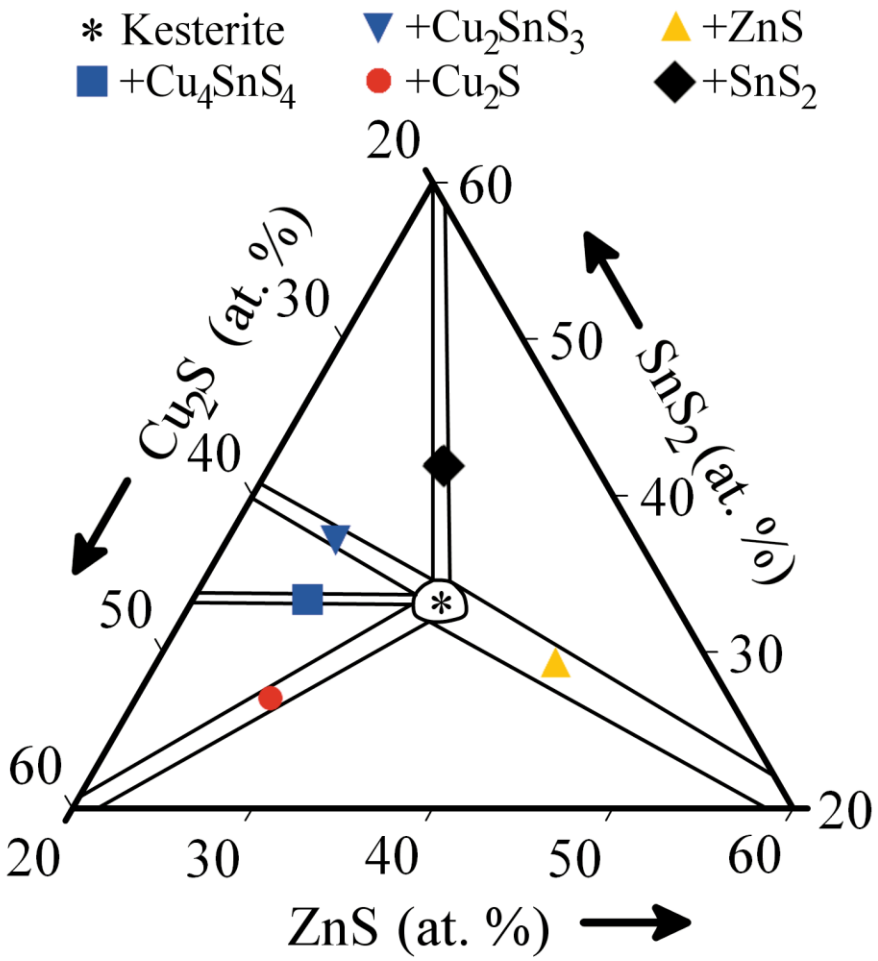

Fig.2.3. Ternary phase diagram shows the expected secondary phases at 400°C.

A comprehensive analysis of the Cu_2X-ZnX-SnX_2 pseudo-ternary system (where X could be S or Se) was carried out by Olekseyuk *et al* [6], who presented a phase diagram for the system at 400°C (Fig.2.3). Cu_2ZnSnX_4 as a single phase is present only within a rather narrow range of compositions, which is indicated with an asterisk at the centre of the plot. In all other regions of the phase diagram there are up to two additional secondary phases present, always alongside CZTSSe. The unwanted phases, further referred to as secondary phases, can alter the local electrical properties of thin film solar cells and should be avoided.

2.1.3. Electrical properties

Doping of CZTS material occurs by internal defects. First principle theoretical calculations of the formation energy and the transition energy levels for a series of intrinsic point defects and defect complexes in CZTS shows that 'Cu' atoms sitting on the places of 'Zn' atoms (CuZn antisite) causes p-type conductivity which has a lower formation energy and relatively deeper acceptor level compared to the 'Cu' vacancy [7]. All donor defects have higher formation energy, consistent with the experimental verification of p-type conductivity. The low formation energy of acceptor defects makes n-type doping difficult in CZTS. Most of the reported resistivity values of CZTS thin films vary from ~10^{-3} Ω.cm to 10^{1} Ω.cm [8,9] but resistivity values as high as 10^{4} Ω.cm were also reported [10]. The hole concentration was reported to vary from 10^{16} cm^{-3} to 10^{18} cm^{-3} [11,12] while mobility values were in the range of 1 to 10 $cm^{2} \cdot V^{-1} \cdot s^{-1}$ [13,14].

2.1.4. Optical properties

Theoretically the band gap of stoichiometric kesterite CZTS is calculated to be 1.5 eV by Chen et al [15]. The bandgap reported for CZTS prepared from various deposition techniques varied from 1.4 eV to 1.55 eV [16–18]. The band gap can be tuned from 1.5 (pure sulfide) and 1.0 eV (pure selenide), by varying the sulfur-to-selenium ratio in the related alloy $Cu_2ZnSn(S_xSe_{1-x})_4$ (CZTSSe) [19]. The optical absorption coefficient (α) of CZTS is larger than 10^{-4} cm^{-1} in the visible region of the electromagnetic spectrum [20,21] enabling the absorption of the incident light with energies higher than the bandgap in only a few microns.

2.2. CZTS thin films deposition techniques

The increasing awareness of CZTS as a potentially ideal candidate as photovoltaic absorber material is mainly due to the abundance and variety of routes that have been developed for thin film deposition. To determine the most promising technique for the fabrication of thin films solar cells, the overriding criteria are that the deposition can be completed at low cost while maintaining

high deposition or processing rate with high yield and reproducibility. There exists a wide range of vacuum and non-vacuum based techniques. For deposition techniques, one key barrier toward a reliable and low cost process is the complexity for preparing pure phase thin films. A second common theme generally encountered is the challenge of compositional control during deposition of thin films. Despite these challenges, reasonably successful thin film deposition and device fabrication has been demonstrated for CZTS using both vacuum and non-vacuum deposition techniques.

2.2.1. Vacuum-based deposition techniques

The vacuum based deposition approaches mainly involve thin film deposition using sputtering and evaporation. CZTS thin films are typically fabricated at high temperature from stacks of metals, metal sulfides, or a combination of these two. These deposition techniques have been widely employed in thin film solar cells, as they are capable of delivering timed elemental fluxes while providing a good opportunity to fabricate high uniformity, good quality thin film devices.

2.2.1.1 Sputtering

The first CZTS thin films were prepared by Ito and Nakazawa in 1988 by using an atom beam sputtering method [22]. They reported CZTS cadmium tin oxide heterojunction based devices using CZTS with bandgap of 1.45 eV. However, no efficiency data of these devices were provided, although a V_{oc} of 165 mV was demonstrated. The most successful sputtering route to fabrication of CZTS devices has been developed by Professor Katagiri's group. Using RF co-sputtering of Cu and binary SnS (tin sulfide) and ZnS materials in H_2S (hydrogen sulfide) atmosphere, a 5.74% efficient solar cell was demonstrated in 2007 [23]. By soaking the absorber in deionized water prior to CdS deposition, this resulted in preferential etching of surface oxide contamination, which is believed to lead

to improvement in the FF and J_{sc} of the device due to decreased series resistance [24]. This development has led to the current record performance of sputtered CZTS devices with 6.77% efficiency. Katagiri et al. also reported that the best composition range of Zn/Sn and Cu/(Zn+Sn) ratio was around 1.25 and 0.9, respectively, through investigating the effect of different elemental ratios in CZTS on device performance [25]. In addition, lower H_2S concentration used in the annealing process was suggested to reduce the wear of the sulfurization chamber as H_2S concentration was found to have little effect on device properties.

2.2.1.2. Evaporation

Evaporation was the principal deposition technique used in the early work on preparing CZTS thin films [26]. The first functional evaporated CZTS device with 0.66% PCE (power conversion efficiency) was reported by Katagiri et al. in 1997 by sulphurisation of a stack of Cu/Sn/Zn in a N_2+H_2S (5%) atmosphere at 500 °C [27]. Further refinements of the sequential evaporation and reactive annealing approach included the introduction of ZnS, as opposed to Zn, for the bottom precursor metal layer and increase in the substrate temperature to 400 °C during precursor layer deposition. This has led to improved device performance with 2.62% efficiency [28]. Further optimization of the annealing chamber, and deposition of CdS, and doping CZTS films with Na resulted in solar cells with 5.45% efficiency [29].

In 2010, researchers in IBM fabricated CZTS films through co-evaporation from Cu, Zn, Sn and S sources on a relatively low (110 °C) substrate temperature, followed by annealing on a hot plate at 540 °C for a few minutes. This method yields a pure CZTS thin film solar cell with 6.8% efficiency (V_{oc}, J_{sc} and FF of 587 mV, 17.8 mA/cm^2 and 65%, respectively) [30]. A slight modification in the thermal treatment procedure by increasing the substrate temperature to 150 °C and a post-deposition annealing at 570 °C for 5 mins have led to an up-to-date,

highest performance co-evaporated CZTS solar cell with 8.4% efficiency (V_{oc}= 661 mV, Jsc = 19.5 mA/cm2, FF= 65.8%)[31].

2.2.1.3. Chemical vapor deposition (CVD)

Aerosol assisted CVD was first employed by Ramasamy et al. to fabricate CZTS thin film which used a toluene solution containing diethyldithiocarbamate complexes of Cu, Zn and an alkyl derivative of Sn [32]. The three complexes were found to decompose at 280- 300°C to form pure phase CZTS. Washio et al. have introduced an open atmosphere CVD to synthesise CZTS thin film using $Cu(C_5H_7O_2)_2$, $Zn(C_5H_7O_2)_2$, $Sn(C_5H_7O_2)_2$, followed by sulphurisation of the oxide thin films in an N_2+H_2S (5%) atmosphere at 520-560°C for 3h [33]. The sulphurised CZT(S,O) film exhibited optical bandgap energy of 1.57 eV. Although oxygen was found in the film even after sulphurization process, the fabricated devices yielded a PCE of 6.03%.

2.2.1.4. Pulsed laser deposition (PLD)

The first PLD-based CZTS solar cell was fabricated by employing KrF laser pulses to ablate a CZTS target with the substrate maintained at room temperature during the deposition, followed by post annealing in N_2 atmosphere for an hour. The 500°C annealed films gave 1.74% efficient solar cells. Using the similar film deposition method and tuning the annealing condition by heating the films in a N_2 (nitrogen) + H_2S (5%) atmosphere at 400 °C for an hour, the CZTS device efficiency was further improved to 3.14% [34].

2.2.2. Non vacuum-based deposition techniques

Although vacuum-based deposition approaches provide a good opportunity to fabricate high quality thin film devices, they normally undergo relatively large consumption of energy, long deposition and annealing time, suffer from low material utilization and the issue of element volatility [35].

Hence, non-vacuum based approaches are preferable, to reduce the production cost and have the potential to produce photovoltaic devices on a large scale. These approaches including electrodeposition, spray pyrolysis, sol-gel spin coating, hot-injection, solvothermal and hydrothermal have been extensively explored to synthesize CZTS thin films.

2.2.2.1. Spray pyrolysis

Spray pyrolysis was one of the earliest methods used to prepare CZTS thin films under non-vacuum conditions. In this approach, CZTS thin films were prepared by spraying an aqueous solution of metal chlorides and thiourea in deionized water onto heated glass substrates at 280-360°C [36] Cu_xS (x = 1-2) was found in Cu-rich films whereas Zn-poor films contained a Cu_2SnS_3 impurity. Thermal deposition of related thiourea-metal halide complexes was further investigated by Madarász et al. while Kumar et al. produced a pure phase CZTS without post-annealing process, through modification of the precursor concentration and using a substrate temperature of 370°C [8,37]. In a recent report, an aqueous solution that contains stannic chloride has been found to be able to yield larger grains and better crystallinity of CZTS than the solution containing stannous chloride [13]. Htay et al. have discovered that a CZTS/ZnO heterojunction structured solar cell generates larger V_{oc} but lower J_{sc} as compared to a CZTS/CdS structured solar cell due to the wider bandgap of ZnO, which induces a higher built-in potential [38]. The authors also reported that the decease of J_{sc} could be related to the recombination of minority carriers at CZTS/ZnO interface. The CZTS/ZnO based structure yielded 4.29% efficient device while CZTS/CdS device yielded an efficiency of 4.32%.

2.2.2.2. Electrochemical deposition

CZTS synthesised by electrodeposition was firstly reported by sulfurizing a metal stack of Zn/Sn/Cu (Cu on bottom) layers in an argon atmosphere at 550

°C for 2 h, leading to a PCE of 0.8% [39]. The low efficiency was found to be attributed to a high series resistance (10 Ω cm^2) and high shunt conductance of 7 mS cm^{-2} in the dark (20 mS cm^{-2} under AM 1.5 conditions), as well as substantial recombination in the space charge region. A further improvement in the device performance was obtained by changing the sequence of metal stacks and improving the homogeneity of the electrodeposited film using a rotating disc electrode as well, as etching the film by potassium cyanide (KCN) to remove impurities. This has led to the energy conversion efficiency of the solar cell to 3.2% [40]. Co-electrodeposition of Cu-Zn-Sn films followed by the sulfurization method has been reported by Araki et al. A slightly Zn-rich film yielded a 3.16% efficiency with the CZTS device [41]. It is worth noting that no phase separation was observed in the co-electrodeposited film after the annealing process. A 3.4% efficiency solar cell was fabricated through a similar electrodeposition process but with an optimized annealing process by heating Cu-Zn-Sn films in Ar + H_2S (5%) atmosphere for 8 h. An electrodeposited CZTS solar cell with 7.3% efficiency was recently reported by Ahmed et al [42]. In this report, a two-step annealing process was proposed: (i) low temperature annealing at 210-350°C to form a uniform alloy, followed by (ii) a high temperature annealing at 585°C in a sulfur rich environment for 15 mins. The champion device had a V_{oc}, J_{sc} and FF of 567 mV, 22 mA/cm^2, 58.1%, respectively. The low fill factor was suspected to be due to the high resistance at the back contact, arising from the MoS_2 formed during the sulfurization step.

2.2.2.3. Sol-gel based approach

A sol-gel based synthesis of CZTS thin films was reported in 2007 [43]. Metal acetate and chloride sources, 2-methoxyethanol and monoethanolamine were used as the solvent and stabilizer in the sol-gel synthesis, respectively. The films were made by spin-coating the sol-gel solution and drying them in the air at 300 °C. Then they were sulphurised at 500 °C in a N_2 + H_2S (5%) atmosphere

for 1 h. The resulting films had a nearly stoichiometric composition with bandgap of 1.49 eV. Using a similar sol-gel approach, a device with a structure of soda lime glass (SLG)/Mo/CZTS/CdS/Al:ZnO/Al yielded 1.01% PCE [44] By varying the ratio of Cu/(Zn+Sn) and Zn/Sn to 0.8 and 1.15, respectively, the solar cell efficiency was improved to 2.03% [43]. In later reports, the same group has indicated that annealing at higher than 450 °C and with H_2S concentration of 3% is preferable for larger grain growth [45,46].

2.2.2.4. Hydrazine based approach

In 2010, IBM T. J. Watson Research Center developed an approach to make CZTSSe ink from a dissolved metal sulfide and metal selenide in hydrazine solution. In this approach, the dissolved components acted as a binders which eliminated the need for an organic binding agent and the solid particles acted as stress relief centers, which prevented film cracking. Spin coating of the developed slurries to make films followed by a short heat treatment at 540 °C led to the formation of a CZTSSe film with a uniform pure phase and good grain structure. CZTSSe devices based on SLG/Mo/CZTSSe/CdS/ZnO/ITO structure have been fabricated with PCE of 9.66% [47]. The device efficiency was later improved to 10.1% in 2011, 11.1% in 2012 by improving device characteristics (larger grain size and void reduction, leading to higher fill factor and short circuit current) and 12.6% in 2013 by modifying the device architecture (thinner CdS and transparent conducting layers) [48–50].

2.2.2.5. Nanoparticles-based approach

In 2009, Steinhagen et al. [51] reported on the synthesis of CZTS nanoparticles by adopting a one-pot technique where all the precursors (Cu, Zn, Sn metal salts and elemental sulfur) and oleylamine were mixed together at room temperature and then heated to 280 °C to allow the formation of CZTS nanoparticles. CZTS thin films were deposited by spraying of the CZTS nanoparticle dispersed in toluene onto the ITO coated glass substrates. Solar cells

with a superstrate structure (ITO/ZnO/CdS/CZTS/Au) fabricated from the as-deposited CZTS sample showed efficiencies of 0.23%. In the same year, Guo et al. [52] also reported on the synthesis of CZTS nanoparticles with a stoichiometry of $Cu_{2.12}Zn_{0.84}Sn_{1.06}S_4$ using a hot-injection approach where Cu, Zn, Sn metal salts and elemental sulfur were used as precursor while oleylamine was used as both solvent and surfactant. The CZTS thin films were deposited by drop casting of the CZTS nanoparticle dispersed in toluene onto a Mo coated SLG substrate and sequentially annealed between 400 and 500 °C in Se-containing atmosphere for 20 min. The sample annealed at 500 °C gave the best solar cells with conversion efficiencies of 0.8 %. Later on, they optimized Cu-poor, Zn-rich composition of the CZTS nanoparticles and achieved 7.2% efficiencies using doctor-blade method [53]. Most recently, Miskin et al reported 9.0% efficiency which is the record efficiency of nanoparticles based approach [54].

Most recently, heating up method was used to prepare the CZTS nanoparticles and a few reports existing in the literature. Jasieniak et al. [55] reported a one-pot heating-up synthesis for the preparation of CZTS nanoparticles using binary sulfur precursors. Sungjee Kim et al. [56] prepared CZTS nanoparticles by heating-up method using a mixture of oleic acid and oleylamine under a vacuum atmosphere. Nevertheless, they used multi-solvents with quite expensive precursors and it possesses relatively high temperature (>250˚C). Therefore, a facile and inexpensive precursors at relatively low-temperature synthesis are highly demanded to prepare high quality, monodisperse kesterite CZTS nanoparticles. Also, utilization of single solvent is highly recommended to synthesize CZTS nanoparticles for solar cell applications. Because these nanoparticles will be used to deposit as a thin film and then annealed at high temperatures. Multi-solvent usage in the nanoparticles synthesis increases the carbon contamination in the film. Thus, carbon inhibits the grain growth while film annealed at high temperatures which would affect

the solar cell performance. In this regard, we propose a facile one-pot heating up synthesis at relatively low temperature (220 °C) using single solvent and vacuum free atmosphere to prepare kesterite CZTS nanoparticles for the first time. Besides, we synthesized CZTS nanoparticles by hot-injection process. The experimental procedure for heating-up and hot-injection process can be seen in chapter 3.

References

[1] K.-H. Seol, Jae-Seung and Lee, Sang-Yul and Lee, Jae-Choon and Nam, Hyo-z Duk and Kim, Electrical and optical properties of Cu_2ZnSnS_4 thin films prepared by rf magnetron sputtering process, Solar Energy Materials and Solar Cells. 75 (2003) 115–162.

[2] T. Tanaka, T. Nagatomo, D. Kawasaki, M. Nishio, Q. Guo, A. Wakahara, A. Yoshida, H. Ogawa, Preparation of Cu_2ZnSnS_4 thin films by hybrid sputtering, Journal of Physics and Chemistry of Solids. 66 (2005) 1978–1981. doi:10.1016/j.jpcs.2005.09.037.

[3] S. Schorr, Structural aspects of adamantine like multinary chalcogenides, Thin Solid Films. 515 (2007) 5985–5991. doi:10.1016/j.tsf.2006.12.100.

[4] D.M. Tabbens, G. Gurieva, S. Levcenko, T. Unold, S. Schorr, Temperature dependency of Cu/Zn ordering in CZTSe kesterites determined by anomalous diffraction, Physica Status Solidi (B) Basic Research. 253 (2016) 1890–1897. doi:10.1002/pssb.201600372.

[5] T. Washio, H. Nozaki, T. Fukano, T. Motohiro, K. Jimbo, H. Katagiri, Analysis of lattice site occupancy in kesterite structure of Cu_2ZnSnS_4 films using synchrotron radiation x-ray diffraction, Journal of Applied Physics. 110 (2011) 74511. doi:10.1063/1.3642993.

[6] I.D. Olekseyuk, I. V. Dudchak, L. V. Piskach, Phase equilibria in the Cu_2S-ZnS-SnS_2 system, Journal of Alloys and Compounds. 368 (2004) 135–143. doi:10.1016/j.jallcom.2003.08.084.

[7] S. Chen, J.H. Yang, X.G. Gong, A. Walsh, S.H. Wei, Intrinsic point defects and complexes in the quaternary kesterite semiconductor Cu_2ZnSnS_4, Physical Review B - Condensed Matter and Materials Physics. 81 (2010) 35–37. doi:10.1103/PhysRevB.81.245204.

[8] Y.B.K. Kumar, P.U. Bhaskar, G.S. Babu, V.S. Raja, Effect of copper salt and thiourea concentrations on the formation of Cu_2ZnSnS_4 thin films by spray pyrolysis, Physica Status Solidi (A) Applications and Materials Science. 207 (2010) 149–156. doi:10.1002/pssa.200925194.

[9] R. Lydia, P.S. Reddy, Effect of pH on the Characteristics of Cu_2ZnSnS_4 Nanoparticles, 2013 (2013) 1–6.

[10] H. Katagiri, N. Sasaguchi, S. Hando, S. Hoshino, J. Ohashi, T. Yokota, Preparation and evaluation of Cu_2ZnSnS_4 thin films by sulfurization of E-B evaporated precursors, Solar Energy Materials and Solar Cells. 49 (1997) 407–414. doi:10.1016/S0927-0248(97)00119-0.

[11] P.A. Fernandes, P.M.P. Salomé, A.F. Da Cunha, B.A. Schubert, Cu_2ZnSnS_4 solar cells prepared with sulphurized dc-sputtered stacked metallic precursors, Thin Solid Films. 519 (2011) 7382–7385. doi:10.1016/j.tsf.2010.12.035.

[12] V.G. Rajeshmon, C.S. Kartha, K.P. Vijayakumar, Spray pyrolysed Cu_2ZnSnS_4 solar cell using cadmium free buffer layer, AIP Conference Proceedings. 1349 (2011) 683–684. doi:10.1063/1.3606042.

[13] V.G. Rajeshmon, C.S. Kartha, K.P. Vijayakumar, C. Sanjeeviraja, T. Abe, Y. Kashiwaba, Role of precursor solution in controlling the opto-electronic properties of spray pyrolysed Cu_2ZnSnS_4 thin films, Solar Energy. 85 (2011) 249–255. doi:10.1016/j.solener.2010.12.005.

[14] F. Liu, Y. Li, K. Zhang, B. Wang, C. Yan, Y. Lai, Z. Zhang, J. Li, Y. Liu, In situ growth of Cu_2ZnSnS_4 thin films by reactive magnetron co-sputtering, Solar Energy Materials and Solar Cells. 94 (2010) 2431–2434. doi:10.1016/j.solmat.2010.08.003.

[15] S. Chen, X.G. Gong, A. Walsh, S.H. Wei, Crystal and electronic band structure of Cu_2ZnSnX_4 (X=S and Se) photovoltaic absorbers: First-principles insights, Applied Physics Letters. 94 (2009) 2–5. doi:10.1063/1.3074499.

[16] K. Moriya, J. Watabe, K. Tanaka, H. Uchiki, Characterization of Cu_2ZnSnS_4 thin films prepared by photo-chemical deposition, Physica Status Solidi (C) Current Topics in Solid State Physics. 3 (2006) 2848–2852. doi:10.1002/pssc.200669588.

[17] Y. Krockenberger, I. Fritsch, G. Cristiani, A. Matveev, L. Alff, H.U. Habermeier, B. Keimer, Epitaxial growth of Na_xCoO_2 thin films by pulsed laser deposition, Thin Solid Films. 486 (2005) 170–173. doi:10.1016/j.tsf.2004.11.231.

[18] T. Prabhakar, J. Nagaraju, Ultrasonic spray pyrolysis of CZTS solar cell absorber layers and characterization studies, Conference Record of the IEEE Photovoltaic Specialists Conference. (2010) 1964–1969. doi:10.1109/PVSC.2010.5616709.

[19] F. Liu, F. Zeng, N. Song, L. Jiang, Z. Han, Z. Su, C. Yan, X. Wen, X. Hao, Y. Liu, Kesterite $Cu_2ZnSn(S,Se)_4$ Solar Cells with beyond 8% Efficiency by a Sol-Gel and Selenization Process, ACS Applied Materials and Interfaces. 7 (2015) 14376–14383. doi:10.1021/acsami.5b01151.

[20] Y.B. Kishore Kumar, G. Suresh Babu, P. Uday Bhaskar, V. Sundara Raja, Preparation and characterization of spray-deposited Cu_2ZnSnS_4 thin films, Solar Energy Materials and Solar Cells. 93 (2009) 1230–1237. doi:10.1016/j.solmat.2009.01.011.

[21] H. Katagiri, K. Jimbo, W.S. Maw, K. Oishi, M. Yamazaki, H. Araki, A. Takeuchi, Development of CZTS-based thin film solar cells, Thin Solid Films. 517 (2009) 2455–2460. doi:10.1016/j.tsf.2008.11.002.

[22] K. Ito, T. Nakazawa, Electrical and Optical Properties of Stannite-Type Quarternary Semiconductor Thin Films, Japanese Journal of Applied Physics. 27 (1988) 2094–2097. doi:10.1143/JJAP.27.2094.

[23] F. Liu, K. Zhang, Y. Lai, J. Li, Z. Zhang, Y. Liu, Growth and Characterization of Cu_2ZnSnS_4 Thin Films by DC Reactive Magnetron

Sputtering for Photovoltaic Applications, Electrochemical and Solid-State Letters. 13 (2010) H379–H381. doi:10.1149/1.3481764.

[24] R. Touati, M. Ben Rabeh, M. Kanzari, ScienceDirect E-MRS Spring Meeting 2013 Symposium D -Advanced Inorganic Materials and Structures for Structural and Optical Properties of the New Absorber Cu_2ZnSnS_4 Thin Films Grown by Vacuum Evaporation Method, Energy Procedia. 44 (2014) 44–51. doi:10.1016/j.egypro.2013.12.008.

[25] H. Katagiri, K. Jimbo, M. Tahara, H. Araki, K. Oishi, The influence of the composition ratio on CZTS-based thin film solar cells Hironori Katagiri, Kazuo Jimbo, Masami Tahara, Hideaki Araki and Koichiro Oishi Nagaoka National College of Technology, 888 Nishikatakai, Nagaoka, Niigata 940-8532, Japan, Materials Research Society Symposium Proceedings Vol. 1165. 1165 (2009) 1165-M04-1. doi:10.1016/j.solmat.2011.05.050.

[26] T. Tanaka, D. Kawasaki, M. Nishio, Q. Guo, H. Ogawa, Fabrication of Cu_2ZnSnS_4 thin films by co-evaporation, Physica Status Solidi (C) Current Topics in Solid State Physics. 3 (2006) 2844–2847. doi:10.1002/pssc.200669631.

[27] T. Kobayashi, K. Jimbo, K. Tsuchida, S. Shinoda, T. Oyanaoi, H. Katagiri, Investigation of Cu_2ZnSnS_4-based thin film solar cells using abundant materials, Japanese Journal of Applied Physics, Part 1: Regular Papers and Short Notes and Review Papers. 44 (2005) 783–787. doi:10.1143/JJAP.44.783.

[28] H. Katagiri, K. Saitoh, T. Washio, H. Shinohara, T. Kurumadani, S. Miyajima, Development of thin film solar cell based on Cu_2ZnSnS_4 thin films, Solar Energy Materials and Solar Cells. 65 (2001) 141–148. doi:10.1016/S0927-0248(00)00088-X.

[29] B. A. Schubert, B.Marsen, S. Cinque, T. Unold, R. Klenk, S. Schorr and H-W. Schoc, Cu_2ZnSnS_4 thin film solar cells by fast coevaporation, Prog. Photovolt: Res. Appl. 19 (2011) 93–96. doi: 10.1002/pip.976.

[30] O. Gunawan, T.K. Todorov, D.B. Mitzi, Loss mechanisms in hydrazine-processed $Cu_2ZnSn(Se,S)_4$ solar cells., Applied Physics Letters. 97 (2010) 233506. doi:10.1063/1.3522884.

[31] B. Shin, O. Gunawan, Y. Zhu, N. A. Bojarczuk, S. Jay Chey and Supratik Guha, Thin film solar cell with 8.4% power conversion efficiency using an earth-abundant Cu_2ZnSnS_4 absorber, Prog. Photovolt: Res. Appl. 21 (2013) 72–76. doi: 10.1002/pip.1174.

[32] K. Ramasamy, M.A. Malik, P. O'Brien, The chemical vapor deposition of Cu2ZnSnS4 thin films, Chemical Science. 2 (2011) 1170. doi:10.1039/c0sc00538j.

[33] T. Washio, T. Shinji, S. Tajima, T. Fukano, T. Motohiro, K. Jimbo, H. Katagiri, 6% Efficiency Cu2ZnSnS4-based thin film solar cells using oxide precursors by open atmosphere type CVD, Journal of Materials Chemistry. 22 (2012) 4021. doi:10.1039/c2jm16454j.

[34] A. V. Moholkar, S.S. Shinde, A.R. Babar, K.U. Sim, H.K. Lee, K.Y. Rajpure, P.S. Patil, C.H. Bhosale, J.H. Kim, Synthesis and characterization of Cu_2ZnSnS_4 thin films grown by PLD: Solar cells, Journal of Alloys and Compounds. 509 (2011) 7439–7446. doi:10.1016/j.jallcom.2011.04.074.

[35] A. Weber, R. Mainz, H.W. Schock, On the Sn loss from thin films of the material system Cu-Zn-Sn-S in high vacuum, Journal of Applied Physics. 107 (2010). doi:10.1063/1.3273495.

[36] N. Nakayama, K. Ito, Sprayed films of stannite Cu_2ZnSnS_4, Applied Surface Science. 92 (1996) 171–175. doi:10.1016/0169-4332(95)00225-1.

[37] J. Madarász, P. Bombicz, M. Okuya, S. Kaneko, Thermal decomposition of thiourea complexes of Cu(I), Zn(II), and Sn(II) chlorides as precursors for the spray pyrolysis deposition of sulfide thin films, Solid State Ionics. 141–142 (2001) 439–446. doi:10.1016/S0167-2738(01)00740-8.

[38] M.T. Htay, Y. Hashimoto, N. Momose, K. Sasaki, H. Ishiguchi, S. Igarashi, K. Sakurai, K. Ito, A cadmium-free Cu_2ZnSnS_4/ZnO hetrojunction solar cell prepared by practicable processes, Japanese Journal of Applied Physics. 50 (2011) 1–4. doi:10.1143/JJAP.50.032301.

[39] J.J. Scragg, P.J. Dale, L.M. Peter, G. Zoppi, I. Forbes, New routes to sustainable photovoltaics: Evaluation of Cu_2ZnSnS_4 as an alternative absorber material, Physica Status Solidi (B) Basic Research. 245 (2008) 1772–1778. doi:10.1002/pssb.200879539.

[40] J.J. Scragg, D.M. Berg, P.J. Dale, A 3.2% efficient Kesterite device from electrodeposited stacked elemental layers, Journal of Electroanalytical Chemistry. 646 (2010) 52–59. doi:10.1016/j.jelechem.2010.01.008.

[41] D. Colombara, A. Crossay, L. Vauche, S. Jaime, M. Arasimowicz, P.P. Grand, P.J. Dale, Electrodeposition of kesterite thin films for photovoltaic applications: Quo vadis, Physica Status Solidi (A) Applications and Materials Science. 212 (2015) 88–102. doi:10.1002/pssa.201431364.

[42] S. Ahmed, K.B. Reuter, O. Gunawan, L. Guo, L.T. Romankiw, H. Deligianni, A High Efficiency Electrodeposited Cu_2ZnSnS_4 Solar Cell, Advanced Energy Materials. 2 (2012) 253–259. doi:10.1002/aenm.201100526.

[43] K. Tanaka, Y. Fukui, N. Moritake, H. Uchiki, Chemical composition dependence of morphological and optical properties of Cu_2ZnSnS_4 thin films deposited by sol-gel sulfurization and Cu_2ZnSnS_4 thin film solar cell efficiency, Solar Energy Materials and Solar Cells. 95 (2011) 838–842. doi:10.1016/j.solmat.2010.10.031.

[44] K. Tanaka, M. Oonuki, N. Moritake, H. Uchiki, Cu_2ZnSnS_4 thin film solar cells prepared by non-vacuum processing, Solar Energy Materials and Solar Cells. 93 (2009) 583–587. doi:10.1016/j.solmat.2008.12.009.

[45] K. Maeda, K. Tanaka, Y. Nakano, H. Uchiki, Annealing temperature dependence of properties of Cu_2ZnSnS_4 thin films prepared by sol-gel

sulfurization method, Japanese Journal of Applied Physics. 50 (2011). doi:10.1143/JJAP.50.05FB08.

[46] K. Maeda, K. Tanaka, Y. Fukui, H. Uchiki, Influence of H_2S concentration on the properties of Cu_2ZnSnS_4 thin films and solar cells prepared by sol-gel sulfurization, Solar Energy Materials and Solar Cells. 95 (2011) 2855–2860. doi:10.1016/j.solmat.2011.05.050.

[47] T.K. Todorov, K.B. Reuter, D.B. Mitzi, High-efficiency solar cell with earth-abundant liquid-processed absorber, Advanced Materials. 22 (2010) 156–159. doi:10.1002/adma.200904155.

[48] D. Aaron R. Barkhouse, O. Gunawan, T. Gokmen, T. K. Todorov, D. B. Mitzi, Device characteristics of a 10.1% hydrazine-processed $Cu_2ZnSn(Se,S)_4$ solar cell, Prog. Photovolt: Res. Appl. 20 (2012) 6–11. doi: 10.1002/pip.1160.

[49] M.T. Winkler, W. Wang, O. Gunawan, H.J. Hovel, T.K. Todorov, D.B. Mitzi, Optical designs that improve the efficiency of $Cu_2ZnSn(S,Se)_4$ solar cells, Energy & Environmental Science. 7 (2014) 1029. doi:10.1039/c3ee42541j.

[50] W. Wang, M.T. Winkler, O. Gunawan, T. Gokmen, T.K. Todorov, Y. Zhu, D.B. Mitzi, Device characteristics of CZTSSe thin-film solar cells with 12.6% efficiency, Advanced Energy Materials. 4 (2014) 1–5. doi:10.1002/aenm.201301465.

[51] C. Steinhagen, M.G. Panthani, V. Akhavan, B. Goodfellow, B. Koo, B.A. Korgel, Synthesis of Cu_2ZnSnS_4 Nanocrystals for Use in Low-Cost Photovoltaics, (2009) 12554–12555.

[52] Q. Guo, H.W. Hillhouse, R. Agrawal, Synthesis of Cu_2ZnSnS_4 Nanocrystals Ink and Its Use for Solar Cells, Journal of the American Chemical Society. 131 (2009) 4–5. doi:10.1021/ja904981r.

[53] R.A. Qijie Guo, Grayson M. Ford, Wei-Chang Yang, Bryce C. Walker, Eric A. Stach, Hugh W. Hillhouse, Fabrication of 7.2% Efficient CZTSSe Solar Cells

Using CZTS Nanocrystals.pdf, J. Am. Chem. Soc. 132 (2010) 17384–17386. doi:10.1021/ja108427b.

[54] C. K. Miskin, W-C. Yang, C. J. Hages, N. J. Carter, C. S. Joglekar, E. A. Stach, R. Agrawal, 9.0% efficient $Cu_2ZnSn(S,Se)_4$ solar cells from selenized nanoparticle inks, Prog. Photovolt: Res. Appl. 23 (2015) 654–659. doi: 10.1002/pip.2472.

[55] A.S.R. Chesman, N.W. Duffy, S. Peacock, L. Waddington, N. a S. Webster, J.J. Jasieniak, Non-injection synthesis of Cu_2ZnSnS_4 nanocrystals using a binary precursor and ligand approach, Rsc Advances. 3 (2013) 1017–1020. doi:10.1039/c2ra21530f.

[56] Y. Park, H. Jin, J. Park, S. Kim, Simultaneous phase and size control in the synthesis of Cu_2SnS_3 and Cu_2ZnSnS_4 nanocrystals, CrystEngComm. 16 (2014) 8642–8645. doi:10.1039/C4CE01079E.

Chapter 3

Experimental and characterization techniques

In this chapter, the experimental methods and characterizations techniques used in this thesis work, described in detail. Herein, we discuss about preparation of CZTS powder, ink formulation, deposition and selenization of CZTS films and deposition of CdS films. We used several characterization techniques such as XRD, Raman, FE-SEM, TEM, EDS, XPS, UV-VIS-NIR, hall measurement and current-voltage (I-V) measurement to investigate the properties of CZTS powders and films.

3.1. Experimental

We prepared CZTS films from nanoparticles based approach (Fig. 3.1**)** which includes several steps as following:

1. Synthesize of CZTS nanoparticles,
2. Formulation of ink using CZTS nanoparticles,
3. Deposition CZTS ink on glass substrate,
4. Annealing of CZTS films in air, and
5. Selenization of CZTS films under Ar/Se atmosphere.

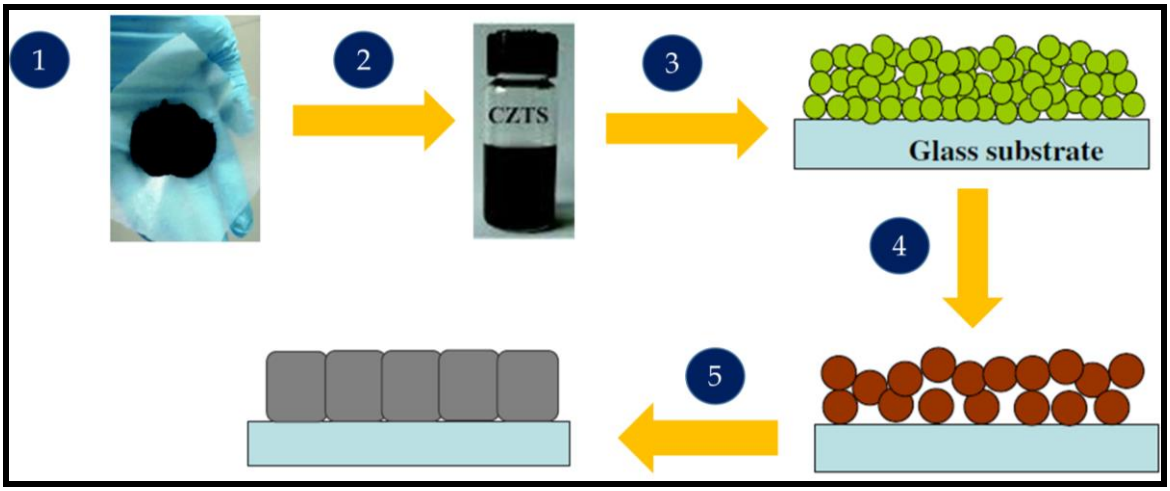

Fig. 3.1. Steps involve in CZTS film preparation process.

3.1.1. Synthesis of CZTS nanoparticles

We have synthesized CZTS nanoparticles (Nps) by two different approaches such as heating-up and hot-injection approach. The detailed explanations are given below.

3.1.1.1. Synthesis of CZTS nanoparticles by heating-up approach

Copper (II) chloride ($CuCl_2$) (99.999%), zinc acetate ($Zn(Ac)_2$) (99.99%), tin (II) chloride ($SnCl_2$) (99.99%), oleylamine (OLA) (technical grade, 70%), chloroform (99.80%) and ethanol (99.90%) were purchased from Sigma-Aldrich. Sulfur powder (99.99%) was purchased from Alfa-Aesar. All the reagents were used without further purification.

CZTS Nps were synthesized by heating-up method. In a typical reaction, 2 mmol of $CuCl_2$, 1 mmol of $Zn(Ac)_2$, 1 mmol of $SnCl_2$ and 4 mmol of sulfur powder were added into 10 mL of OLA at room temperature [1]. Then, the reaction mixture was heated to 220°C and the reaction was maintained at this temperature for 4 h under nitrogen atmosphere. Once the reaction finished, the temperature was cooled down to room temperature. When the temperature reached to 100°C, chloroform was added to the reaction mixture to quench the reaction and ethanol was further added to precipitate the Nps. And then, the

reaction mixture was collected and centrifuged at 4500 rpm for 20 mins. Afterwards, the supernatant was discarded which contains a solvent, by-products, and unreacted precursors. Then, the reaction mixture was washed with chloroform and ethanol (1:1 ratio) followed by centrifugation process for several times to get high purity of the Nps. The final product was dried at 100°C for 3 h in an oven and then used for various characterization.

- The experiments were repeated at various reaction temperatures such as 180, 200, 220 and 240°C with a constant reaction time of 4 h.
- To monitor the growth of the Nps, aliquots were withdrawn from the reaction mixture with a syringe at 220°C for different times (5 mins, 10 mins, 20 mins, 30 mins, 1 h, 2 h, 4 h and 8 h).
- Furthermore, the optimum temperature of 220°C was used to prepare Cu-poor, Zn-rich composition of Nps which is optimal for solar cell applications. For this purpose, 1.74:1.12:0.98:4 ratio of Cu, Zn, Sn and S precursors were taken and OLA (10 mL) was used as a solvent. Washing procedure are same as mentioned above.

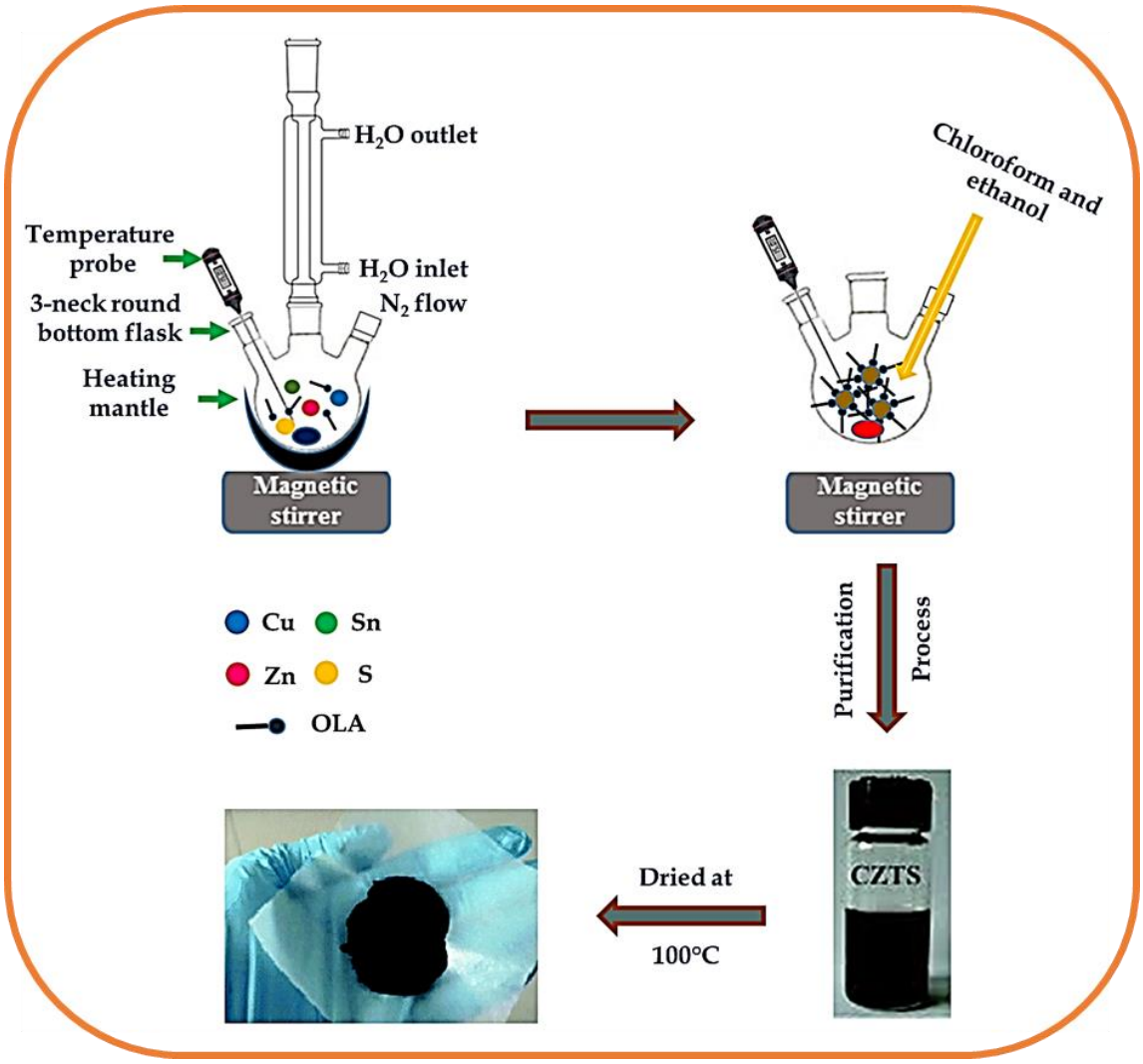

Fig. 3.2. Experimental procedure for synthesis of CZTS nanoparticles by heating-up approach.

3.1.1.2. Synthesis of CZTS nanoparticles by hot-injection approach

CZTS Nps were synthesized by hot-injection approach. In a typical experiment, 1.79 mmol of $CuCl_2$, 1.16 mmol of $Zn(Ac)_2$ and 0.95 mmol of $SnCl_2$ into 10 ml OLA. The mixture was heated to ~160°C with mild magnetic stirring for 30 mins. Then the temperature was raised to 220°C at which point 4 ml of 1 M solution of sulfur dissolved in oleylamine was injected into the reaction mixture. The mixture was maintained at 220 °C for 2 h. When the temperature reached to

100°C, chloroform and ethanol were injected to the reaction mixture. The washing procedure are same as mentioned above.

- The above experiments were repeated for several reaction temperatures such as 180, 200, 220 and 240°C with constant reaction time of 2 h.
- To study the growth mechanism of the Nps, aliquots were taken from the reaction mixture with a syringe at 220°C for different time from 5 mins to 4 h.

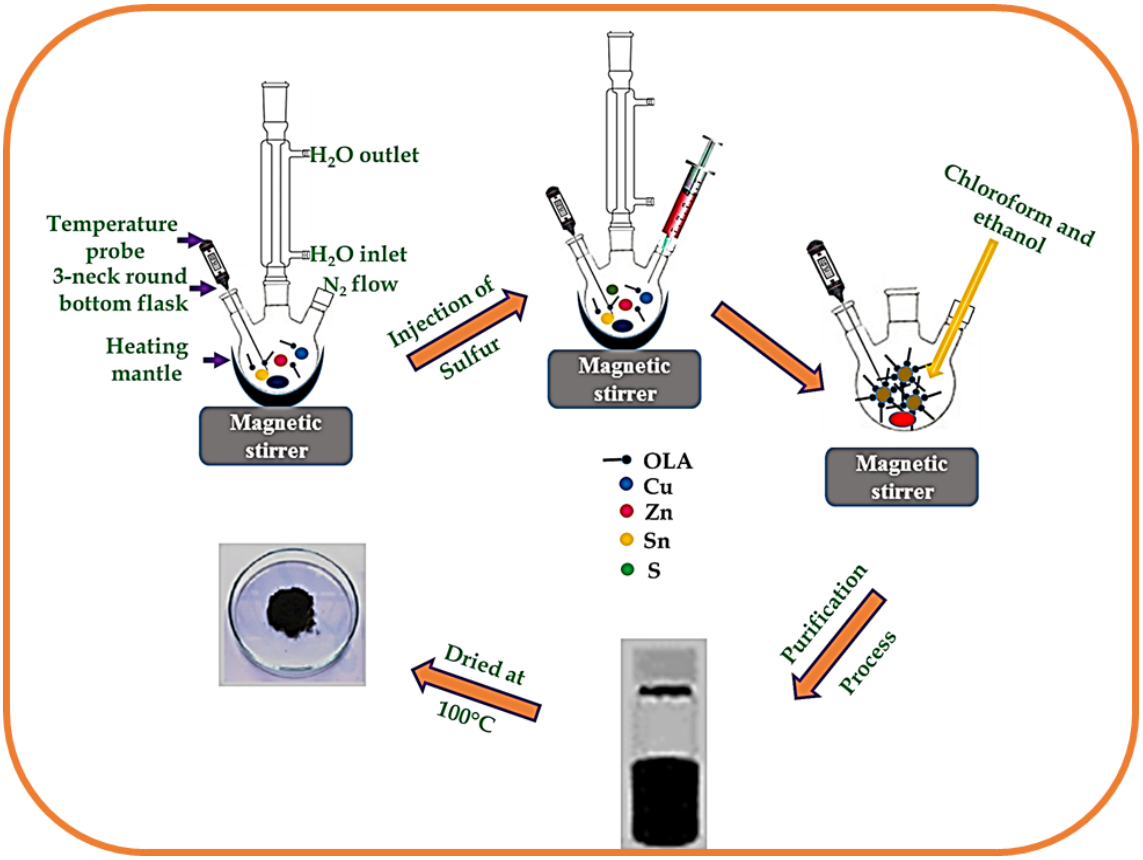

Fig. 3.3. Experimental procedure for CZTS nanoparticles synthesis by hot-injection approach.

3.1.2. Formulation of ink using CZTS nanoparticles

CZTS ink was formulated by dispersing synthesized CZTS nanoparticles in hexanethiol [2] (purity; 95%) and sonicated for 60 mins. The most important parameter of CZTS powder concentration was varied such as 0.1, 0.075 and 0.050 g in 1 mL hexanethiol. The prime motive of varying the CZTS powder concentration was to obtain crack free films.

3.1.3. Deposition of CZTS films

3.1.3.1. Substrate

There are several substrate materials that are suitable for CZTS solar cells. Today, the "standard" substrate is soda-lime glass (SLG), which allowed champion efficiencies. SLG is a suitable substrate for CZTS solar cells mainly because it has a well matched thermal expansion coefficient, exhibits a smooth surface, is cheap, and releases Na into the CZTS. Drawbacks are its loss of rigidity above 550- 600 °C, and possible property variations from factory to factory and sometimes even across one substrate. However, for laboratory cells rigidity loss is usually not a problem, while the property variations mainly concern Na (and K) out-diffusion during CZTS deposition. The SLG substrates used for this thesis had a thermal expansion coefficient of 9×10^{-6} K^{-1}.

3.1.3.2. Cleaning of substrate

The typical substrate cleaning procedure for all substrates was washing the samples with soap and de-ionized (DI) water. Then the samples were cleaned in an ultrasonic bath first in a mixture of acetone and 2-propanol and afterwards in methanol. Between all steps and at the end, the samples were thoroughly rinsed with DI water. Finally, the substrates were dried in a jet of nitrogen gas. Surface treatment of the cleaned substrates was carried out in a solution of H_2SO_4 (> 95%, Aldrich) and H_2O_2 (50%, Botica Moderna) (2:1) for 2 to 3 min. Finally, the substrates were dried in nitrogen gas before film preparation.

3.1.3.3. Deposition of CZTS ink

The deposition process of CZTS ink is shown in Fig. 3.4. CZTS Nps were used to deposit thin films by doctor-blade method. CZTS ink was formulated by varying powder concentration of 0.1 g, 0.075 g and 0.05 g in 1 mL hexanethiol. Then, the ink was coated onto soda-lime glass substrates by the doctor-blade method to form densely packed Nps thin film. A layer of scotch tape was used as the spacer for thin film preparation. Two coatings were applied to get uniform film thickness.

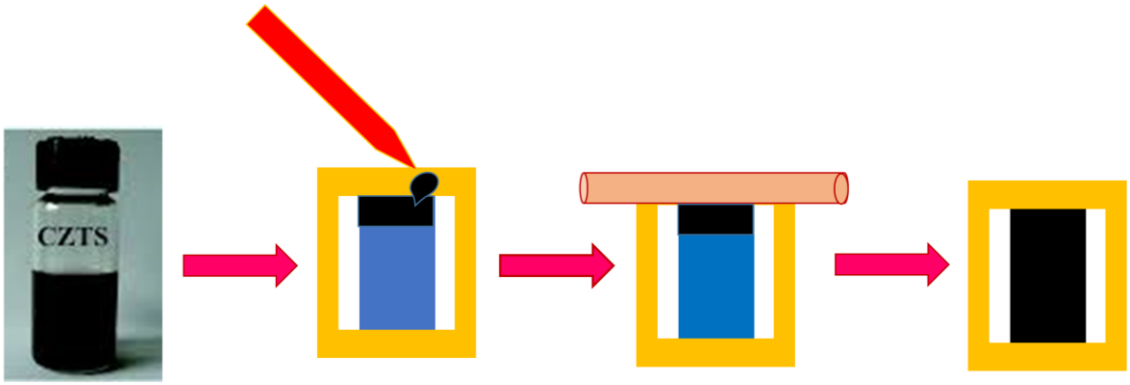

Fig.3.4. Preparation of CZTS film process.

3.1.4. Annealing of CZTS films (Step 4)

3.1.4.1. Air annealing

The furnace used for air annealing is shown in Fig. 3.5. After each coating, the film was annealed at 350 and 400^{0}C for 1 min in the pre-heated oven to evaporate the carbon and solvent.

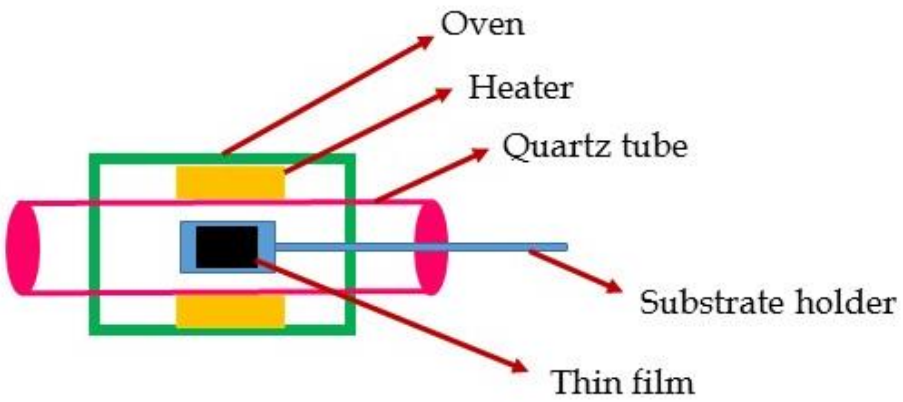

Fig.3.5. Air annealing of CZTS film.

3.1.4.2. Annealing under Ar/Se atmosphere

The annealed CZTS films were selenized under selenium atmosphere to replace the majority of sulfur (S) atoms with selenium (Se) atoms. The 50 mg of Se and 5 mg of tin (to avoid the tin loss) powder were introduced into the graphite box along with CZTS film and loaded into the furnace. Fig. 3.6 shows the photograph of furnace and graphite box. A two-step selenization was carried out using partially closed graphite box under argon atmosphere. In the first step, the film annealed at 400^0C for 30 mins in order to incorporate the Se into the CZTS crystal lattice. During the second step, the temperature was further increased to 500^0C for 15 mins to facilitate the recrystallization and enhance grain growth. The ramp of temperature was 20^0C/min. The selenization temperature in the second step was varied such as 500, 525 and 550^0C by keeping the constant time of 15 mins.

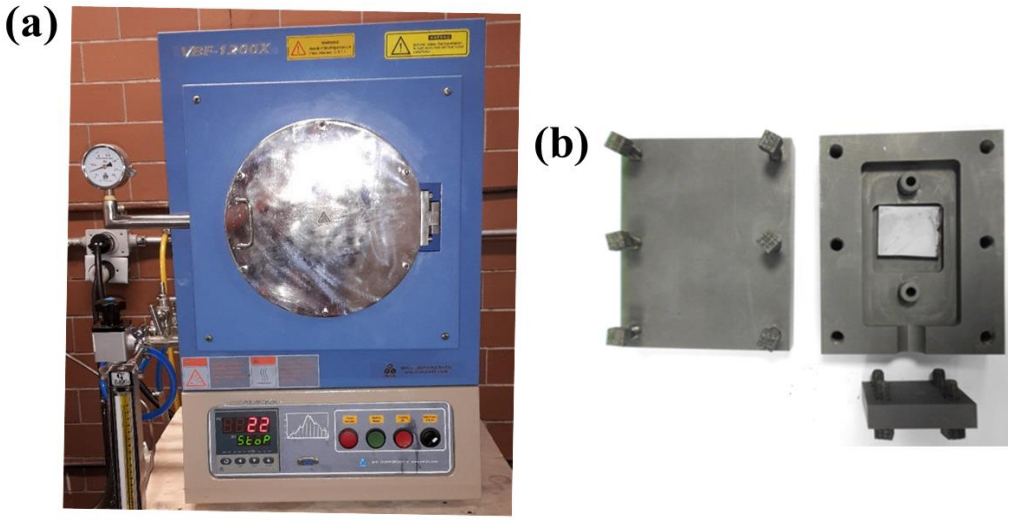

Fig. 3.6. Photograph a) selenization furnace and (b) graphite box.

3.2. Characterization techniques

3.2.1. X-ray diffraction spectroscopy (XRD)

X-ray diffractometer consists of three parts namely a basic diffraction unit, acounter goniometer and an electronic circuit panel with an automatic recorder as shown in Fig. 3.8. Collimated X-ray beam produced at a rating of 40 KV-20 mA is allowed to be incident on the sample and the diffracted rays are received by a proportional (or scintillation) counter through a crystal monochromater or a Ni-filter for CuKα_2 radiation (λ=1.5444 Å). In the present work, CZTS films were analyzed by using PANalytical Xpert X-Ray Diffractometer with CuKα1 (λ=1.5406 Å) in the θ-2θ mode with step size of 0.039.

Fig. 3.8. System view of XRD measurement.

Fig.3.9. illustrates the diffraction of X-rays by a crystal. A diffractometer basically consists of an X-ray source, sample stage, and detector to measure the reflected rays. The intensities of the diffracted beam at different angles is measured by the detector and is represented in a diffraction pattern as a function of 2θ, whereas 2θ, the diffraction angle, is the angle between the transmitted beam and the diffracted beam. The main goal of using XRD in our work was to identify the crystalline phases in our samples. Determining the phases is obtained by comparing the experimentally measured data with standard data published by the International Center for Diffraction Data (ICDD), previously known as the Joint Committee on Powder Diffraction Standards (JCPDS), and matching the positions of the peaks in the diffractogram to those in the database.

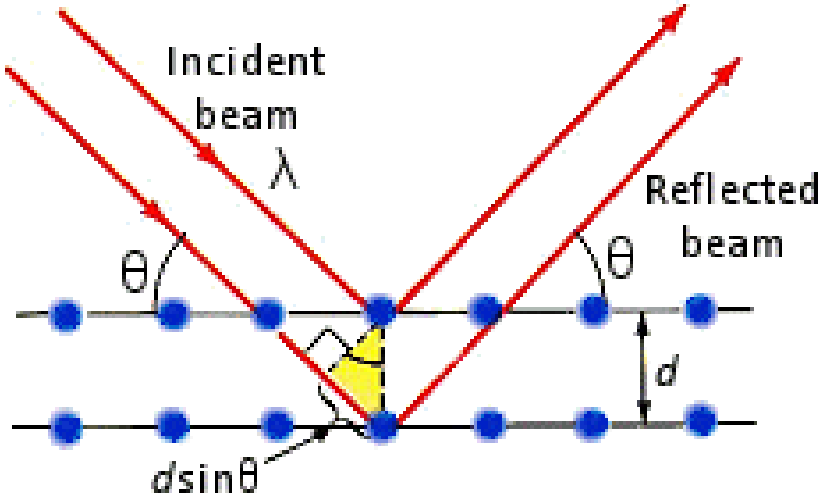

Fig. 3.9. Illustration of the interaction between X-rays and crystallographic planes.

The interplanar distance d can be calculated from known diffraction angle θ using the Bragg's relation,

$$n\lambda = 2d\ sin\theta \qquad ------ 3.1$$

where, n is the order of diffraction, λ is the wavelength of X-ray radiation, d is the interplanar distance and θ is the angle of incidence.

Crystallite sizes (D) are calculated using the Scherrer's formula, [3]

$$D = \frac{K\lambda}{\beta\ cos\theta} \qquad ------ 3.2$$

where, K is a constant (0.9), λ is the X-ray wavelength (1.5406 Å), β is the Full Width Half Maximum (FWHM) and θ is the diffraction angle.

The lattice constants ***a*** and ***c*** are calculated using the following formula: [4]

$$\frac{1}{d^2} = \frac{h^2+k^2}{a^2} + \frac{l^2}{c^2} \qquad ------ 3.3$$

3.2.2. Raman spectroscopy

Raman spectroscopy uses the Raman effect to characterize the chemical composition and structure of materials. Raman spectroscopy is used in this work as a complementary technique for XRD to identify secondary phases in the CZTS compound.

When a material is illuminated, the incident light can be scattered, absorbed, or pass through the material. Initially, a molecule is most probably in the ground electronic state. If the photon energy matches the energy gap between the ground state and an excited state of the molecule, the photon can be absorbed, transferring its energy to the molecule, and the molecule moves to an electronic excited state. If, on the other hand, the energy of the incident photon is less than the bandgap of the material, the photon will interact with the molecule and scatter from it. In this case, when a monochromatic light with frequency υ_0 (usually a laser) illuminates a sample, the largest part of the scattered light experiences no change in its frequency (no change in the photon wavelength λ_0 or energy hv_0). This kind of scattering is referred to as elastic or Rayleigh scattering. However, a small portion of the scattered photons experiences a frequency shift (gain or loss of energy). This type of scattering is called inelastic or Raman scattering. Comparing both scattering processes, about one photon from every 10^6–10^8 scattered photons would be Raman scattered [5]. The frequency shift of the scattered photons results from exciting the vibrational state of the material molecules by the incident photons so that energy transfer occurs between the molecules and photons. Depending on the direction of energy transfer (from the molecule to the photons or from the photons to the molecule), we differentiate between two types of Raman scattering—namely, Stokes and anti-Stokes scattering. Fig. 3.10 illustrates the energy-level diagram of the three types of scattering.

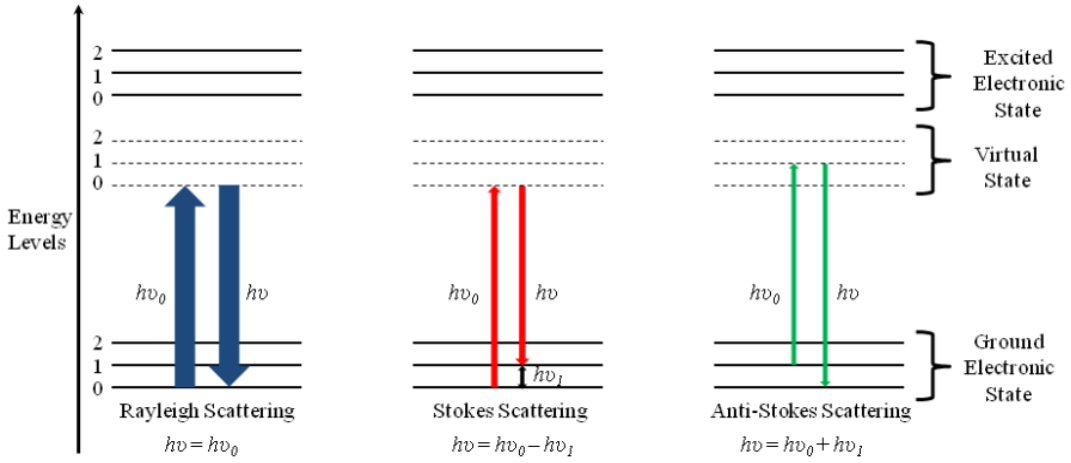

Fig. 3.10. Illustration of the energy-level diagram for Rayleigh scattering, Stokes Raman scattering, and anti-Stokes Raman scattering.

Absorbing the incident photon, the molecule will be excited from the vibrational ground state to a virtual vibrational state for a very short time, and then it falls back to the ground state, emitting a photon.

- If the molecule returns back to the same state it starts from, no energy transfer will occur, and consequently, the emitted photon scatters with the same frequency as of the incident photon (Rayleigh scattering).
- If the molecule falls back to a vibrational mode higher than the state it starts from, energy transfer occurs from the photon to the vibrational mode of the molecule, and consequently, the emitted photon scatters with downshifted frequency (Stokes Raman scattering).
- If the molecule starts from an excited vibrational state and falls back to a lower energy state, energy transfer occurs from the molecule to the photon, so that its frequency is upshifted (anti-Stokes Raman scattering).

Because the frequency shift of the Raman scattered light is related to the transitions between the vibrational modes in the scattering molecule, the energy spectrum of the Raman scattered radiation (Raman spectrum) can be used to identify the material.

Raman analysis were carried out for CZTS films using Horiba–Jobin Yvon equipment (Fig 3.11) with 632 nm wavelength red emission laser.

Fig. 3.11. Horiba–Jobin Yvon LabRAM HR800 equipment.

3.2.3. Field emission scanning electron microscopy (FE-SEM)

FE-SEM technique analyses the surface characteristics such as morphology and chemical composition of the sample thanks to a high-energy beam of electrons. The electrons interact with the atoms which make up the sample giving rise to informative signals (Fig. 3.12) on the sample's topographical information, elemental composition and homogeneity etc. A FE-SEM differs from usual SEM technique by the use of field-emission cathode as electron gun providing narrow probing beams at low currents as well as high electron energy beam under high vacuums (10^{-1} Torr). With such instrumental parameters, analyses are realized by improved spatial resolution and minimized sample charging as well as less damage.

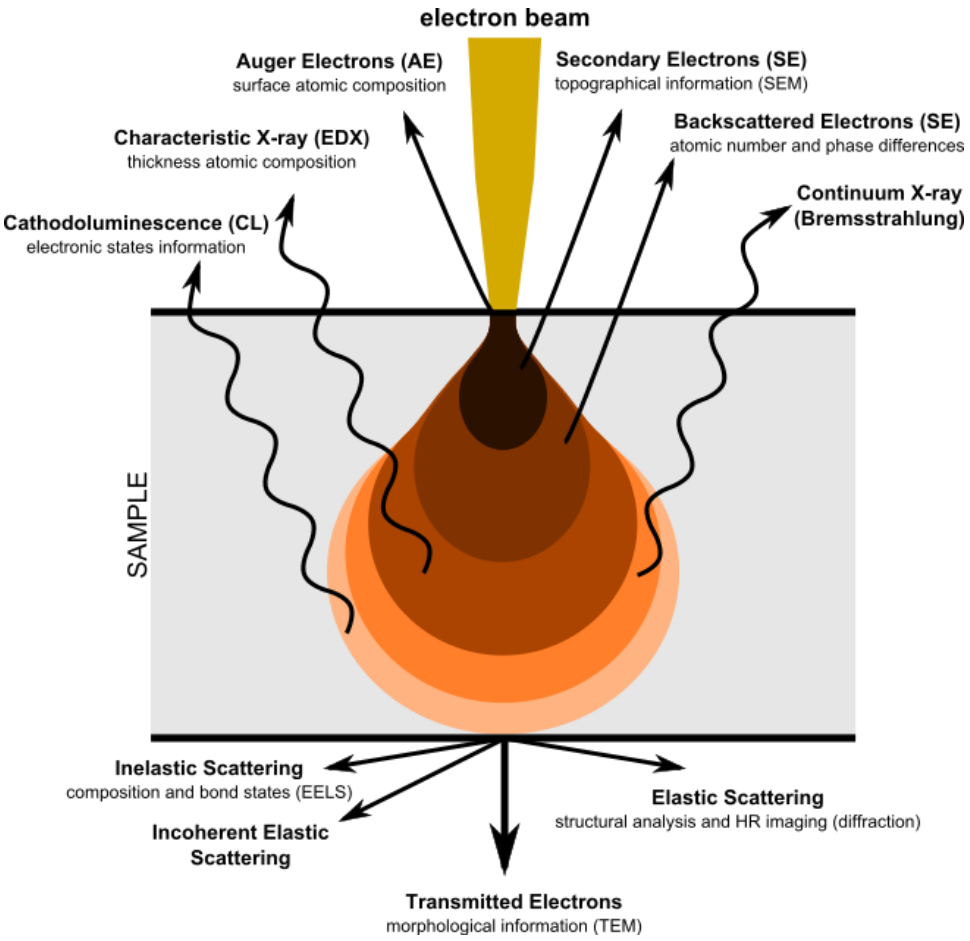

Fig. 3.12. Types of emission from a specimen surface excited by the primary incident.

In the present work, surface morphology of the CZTS thin films and cross sectional images were analysed by a Carl Zeiss AURIGA FESEM workstation as shown in Fig. 3.13.

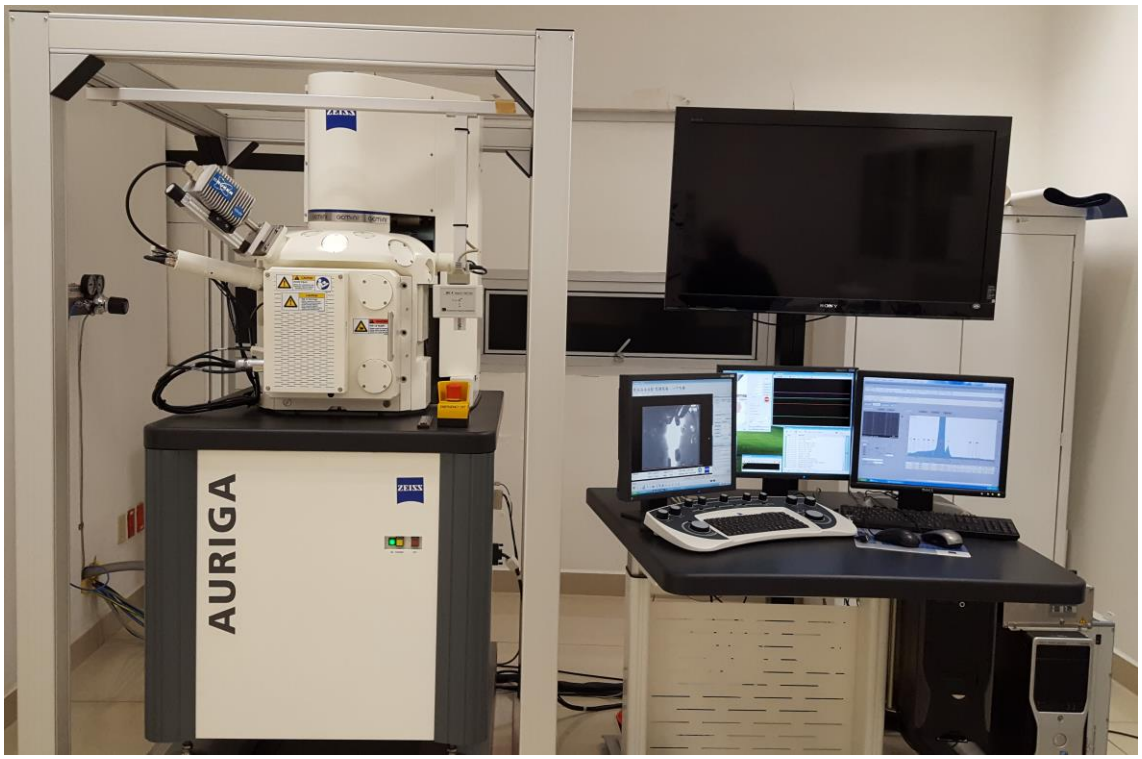

Fig. 3.13. Carl Zeiss AURIGA FESEM workstation.

3.2.4. Energy dispersive X-ray analysis spectroscopy (EDAX)

Energy dispersive X-Ray analysis spectroscopy is a powerful chemical analysis technique. It normally uses in conjunction with FE-SEM. When beam of electron bombard with the sample, x-rays will be emitted from the sample whose energy is characteristic of the material from which it is emitted. EDAX X-ray detector measures the relative abundance of X-rays versus its energy. Detector is normally a Li-drifted Si, solid state device. The Detector creates charge pulse proportional to the energy of emitted Xrays which is then converts to voltage signal by a charge sensitive preamplifier. Later, it is sent to multichannel analyser where it is sorted by voltage. EDAX spectrum of Xray energy versus counts is quantitatively evaluated to determine the elemental composition of the sample. In principle, EDAX can identify all elements from atomic number 4 to 92. Fig. 3.14 shows an EDAX spectrum of a CZTS sample, where the abscissa

represents the X-ray energy in eV and the ordinate axis represents the number of counts.

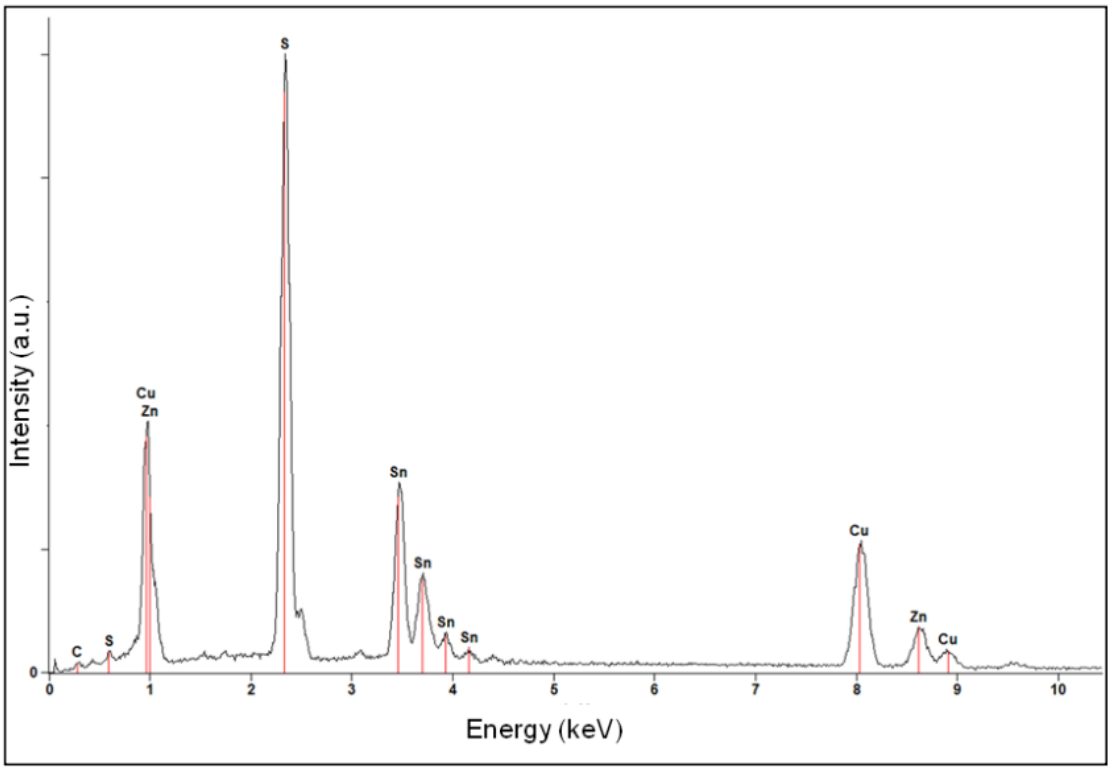

Fig. 3.14. Energy-dispersive X-ray spectrum of a CZTS sample.

The chemical composition of the CZTS samples was measured using energy dispersive analysis of X-ray spectroscopy (EDAX) (XFlash Detector 5010) in the FE-SEM at 15 kV.

3.2.5. Transmission electron microscopy (TEM)

TEM is one of the widely used microscopy technique which is based on an electron beam transmitted through a sample. To make it simple, the transmitted electrons interact with the sample as they pass through it and an image is formed. Then the image is magnified and focused in an imaging device usually in a digital camera. TEMs are usually capable of imaging at a very high resolution than other microscopes. At smaller magnifications TEM image contrast is due to absorption of electrons by the material, depending on the

thickness and constituents of the sample. At higher magnifications (HRTEM), complex wave interactions modulate the image intensity. And using the alternate modes of TEM, it allows identifying chemical elements, crystal orientation, and electronic structure as well as the imaging [6].

The high-angle annular dark field scanning transmission electron microscopy (HAADF-STEM) is one of the high-resolution microscopy techniques that benefits most from the most recent improvement of the aberration corrector [7]. Therefore, the HAADFSTEM technique has attracted enormous attention for its various applications such as tomography [8], size and thickness measurement usually at atomic scale, structure characterization [9] and composition measurement. This technique uses a sharply focused beam to scan across the sample and the annular dark field (ADF) detector collects only the scattered electrons from the sample. Thus the resulting image contrast is always referred as Z-contrast [10].

TEM images (Fig. 3.15) were taken on a HRTEM (JEOL, JEM-ARM200F) equipped with HAADF-STEM detector and Oxford XMax 80 Energy Dispersive analysis of X-Ray (EDAX). The sample was prepared in such a way that aggregation in the grid was avoided. Then, 10 µl (micro litre) of the sample were dispersed in 100 µl of isopropanol, which was sonicated for 30 mins; then a drop of sonicated nanoparticles dispersion was placed onto the amorphous carbon-coated 200 mesh copper grid (Ted Pella, Inc.). Finally, the sample was allowed to dry at ambient temperature before it was loaded into the microscope.

Fig. 3.15. TEM instrument for morphology analysis, EDS and HAADF-STEM techniques.

3.2.6. X-ray photoelectron spectroscopy (XPS)

XPS is used to study the electronic state of the surface of a NPs by employing photon-ionization and energy-dispersive analysis of the emitted photoelectrons (3.16). And also it allows calculating the concentrations of

different elements in the sample quantitatively by comparing the peak area of respective elements [11].

In this thesis, the XPS analysis was performed using a K-Alpha X-ray Photoelectron Spectrometer (XPS) System (Surface Analysis, Thermo Scientific). Monochromated, Microfocused Al K_α was used as an X-ray source type. The binding energy of C1s carbon was used for calibration. The spectrum was obtained via collecting electrons ejected from core level by incident X-ray photons.

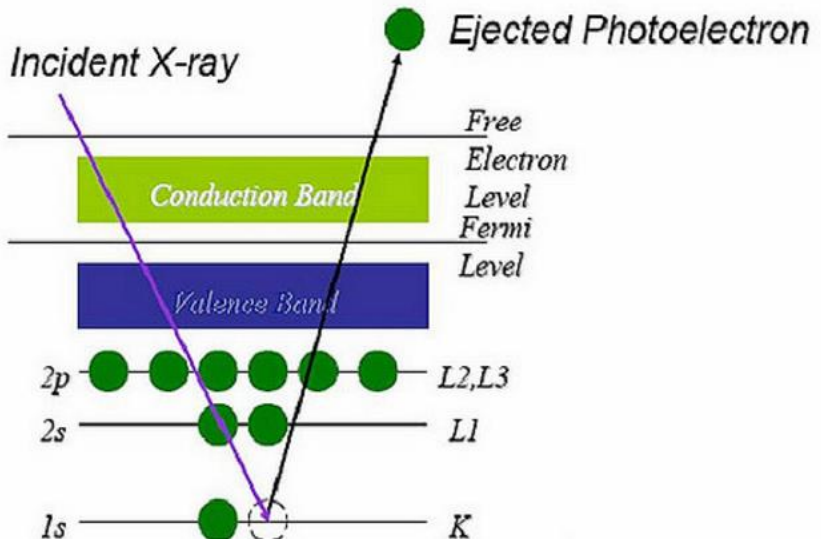

Fig. 3.16. Principles of x-ray photoelectron spectroscopy (XPS).

3.2.7. Ultraviolet-visible-near infrared (UV-Vis-NIR) spectroscopy

UV-Vis-NIR spectroscopy analysis is a non- destructive and fast optical characterization technique. This technique investigates the material property through its interaction with light (200-2200 nm) by measuring the intensity of light transmitted, reflected or absorbed by the material using spectrophotometer. A UV-Vis-NIR spectrophotometer consists of couple of light sources, diffraction grating based monochromator, sample chamber and one or two detectors. Light

from the source first passes through the diffraction grating where it gets separated into component wavelength. Now, the monochromatic beam passes through the slit to the sample and get reflected by the mirror and reaches the detector. Detector converts the light into current signal that is readable by a computer [12].

UV-Vis-NIR spectrum of a sample gives a plot of wavelength of incident light versus intensity of transmitted, reflected or absorbed light. UV-Vis-NIR transmittance spectrum is useful to obtain absorption coefficient, extinction coefficient, thickness, refractive index and bandgap of material.

From the transmittance spectrum of a film, absorbance coefficient is calculated using the following expression,

$$\propto = \frac{1}{t} \, ln \frac{1}{T} \quad ------ 3.4$$

Where, t is the thickness of the film and T is the transmittance.

The type of bandgap of material is determined from the transition probability given by

$$\propto h\nu^{p} = A\left(h\nu - E_g\right) \quad ------ 3.5$$

where A is a constant and p is a variable

If, p=2, the transition between the bands are allowed direct band gap transitions.

If p =2/3, the transition is prohibited direct band gap.

If p=1/2, the transition is allowed indirect band gap.

If p=1/3, the transition is prohibited indirect band gap.

To find bandgap of a direct bandgap semiconductor material, a graph of hυ over $(\alpha h\upsilon)^2$ has to be plotted and then a straight line to this is fitted. The constant of this equation is E_g. But in the case of indirect bandgap material a graph of hυ over $(\alpha h\upsilon)^{1/2}$ has to be plotted and do the same to get E_g.

In the present work, UV-Vis-NIR absorption spectra of CZTS film is analysed as a function of wavelength 400-2000 nm using JASCO V-670 UV-Vis-

NIR spectrophotometer from SEES as shown in Fig. 3.17. Spectral distributions of transmittance are determined at room temperature. Substrate absorption was corrected by introducing an uncoated clean glass in the reference beam.

Fig. 3.17. JASCO V-670 UV-VIS-NIR Spectrophotometer.

3.2.8. Van der Pauw Method and Hall studies

Van der Pauw method is employed to measure the resistivity of samples. It is one of the most widely used technique to determine average resistivity of thin films. It can be used to measure samples of arbitrary shape if thickness of sample is uniform, point contacts are placed on the edges of the sample and sample is homogenous [13]. A schematic of sample with contacts 1, 2, 3 and 4 in Van der Pauw configuration is shown in Fig. 3.18. Van der Pauw showed a relation to find sheet resistance of the sample using two characteristic resistances R_A and R_B.

$$exp\left(-\frac{\pi R_A}{R_S}\right)+\left(-\frac{\pi R_B}{R_S}\right)=1 \quad ------ \quad 3.6$$

Where, R_s denotes the sheet resistance.

To determine R_A, a current I is forced through the sample between two neighbouring contacts, 1 and 2 as in Fig. 3.18 and the voltage is measured

between the other two contacts 3 and 4. Then the measurement is repeated for other pairs of contacts to find R_B.

$$R_A = \frac{V_{43}}{I_{12}} \; and \; R_B = \frac{V_{14}}{I_{23}} \; ------ 3.7$$

Resistivity (ρ) is obtained from the sheet resistance and thickness (t) of the sample using the relation,

$$\rho = R_S t \; ------ 3.8$$

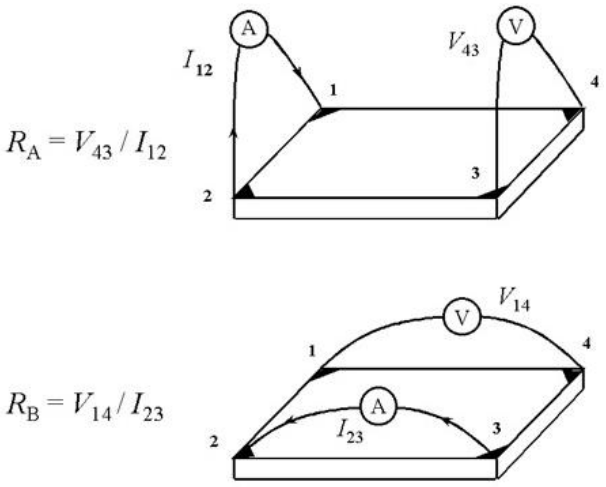

Fig. 3.18. Schematic diagram of a Van der Pauw configuration used in the determination of the two characteristic resistances R_A and R_B [14].

Hall effect is used to find out the carrier concentration, carrier mobility and type of conductivity of a semiconductor material. According to Hall effect, if the current density j_x passes through two non-neighbouring contacts 1 and 3 in presence of magnetic induction B_z, and an electric field E_y, the Hall coefficient R_H is defined by the equation

$$R_H = \frac{E_y}{j_x B_Z} \; j_x \; B_z ------ 3.9$$

The sign of R_H depends on the type of conductivity of material. If R_H is negative, it indicates that E_y is along -y direction and electric current carriers are electrons. If R_H is positive, it indicates that E_y is along +y direction and electric current carriers are holes.

According to Drude model, R_H can be expressed as

$$R_H = \frac{1}{ne} \quad ------3.10$$

Where, e is the electric charge and n is the concentration of charge carriers.
Mobility of charge carriers can determine if n and resistivity values are known [14].

$$\mu = \frac{1}{en\rho} \quad ------3.11$$

Hall measurement system Lakeshore 8407 from SEES with an applied magnetic field of 15 KG at room temperature has been used to analyze conductivity type, carrier concentration, mobility of carrier and resistivity of selenized films (Fig. 3.19). To measure Hall effect, 100 nm thick circular gold (Au) contacts are deposited on the CZTS film by thermal evaporation method.

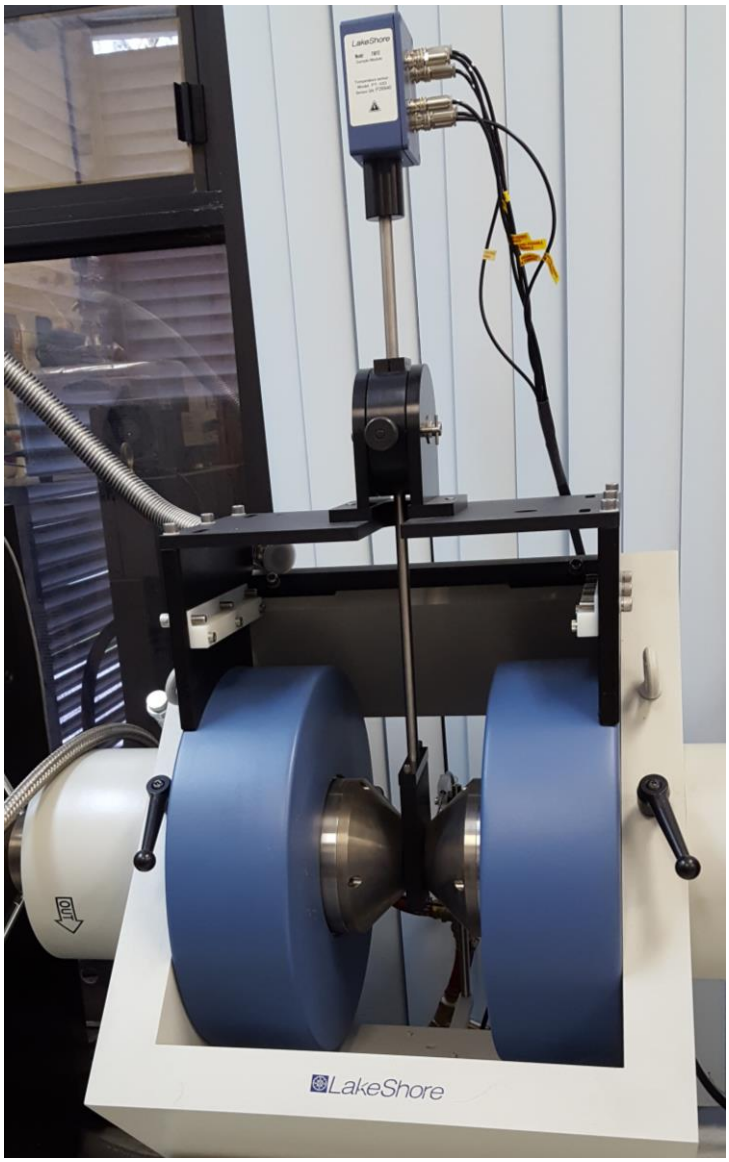

Fig. 3.19. Lakeshore 8407 Hall measurement system.

3.2.9. Current-voltage (I-V) characteristics

The current-voltage curve (I-V) of CZTS and CZTSSe films were collected with standard I-V measurement equipment of Keithley 4200-SCS with a bias voltage between -10 to +10 V. The I-V curves were done in dark and under an illumination of light with the intensity of 300 W. Gold (Au) contacts with the thickness of 100 nm were deposited by evaporation technique. A voltage is

applied across the two Au contacts. The resulting current flowing across the film between two contacts were measured.

Fig. 3.20. Keithley 4200-SCS semiconductor characterization system.

References

[1] R.A. Devi, M. Latha, M. Rohini, P. Reyes-Figueroa, S. Velumani, A.T. Fuentes, M.G. Arellano, F.J.R. Aponte, J. Santoyo-Salazar, Facile one pot synthesis of single phase kesterite CuZnSnS4 nanocrystals, 2016 13th Int. Conf. Electr. Eng. Comput. Sci. Autom. Control. (2016) 1–4. doi:10.1109/ICEEE.2016.7751250.

[2] M. Powalla, B. Dimmler, Scaling up issues of CIGS solar cells, Thin Solid Films. 361 (2000) 540–546. doi:10.1016/S0040-6090(99)00849-4.

[3] A. Monshi, M.R. Foroughi, M.R. Monshi, Modified Scherrer equation to estimate more accurately nano-crystallite size using XRD, World J. Nano Sci. Eng. 2 (2012) 154. doi:10.4236/wjnse.2012.23020.

[4] A. Ben Marai, J. Ben Belgacem, Z. Ben Ayadi, K. Djessas, S. Alaya, Structural and optical properties of CuIn1-xGaxSe2 nanoparticles synthesized by solvothermal route, J. Alloys Compd. 658 (2016) 961–966. doi:10.1016/j.jallcom.2015.10.287.

[5] H.M. Mansour, A.J. Hickey, Raman characterization and chemical imaging of biocolloidal self-assemblies, drug delivery systems, and pulmonary inhalation aerosols: a review., AAPS PharmSciTech. 8 (2007) E99. doi:10.1208/pt0804099.

[6] F.Y. Cheng, C.H. Su, Y.S. Yang, C.S. Yeh, C.Y. Tsai, C.L. Wu, M.T. Wu, D. Bin Shieh, Characterization of aqueous dispersions of Fe3O4 nanoparticles and their biomedical applications, Biomaterials. 26 (2005) 729–738. doi:10.1016/j.biomaterials.2004.03.016.

[7] M. Latha, R.A. Devi, S. Velumani, G. Oza, P. Reyes-Figueroa, M. Rohini, I.G. Becerril-Juarez, J. Yi, Synthesis of CuIn1-xGaxSe2 Nanoparticles by Thermal Decomposition Method with Tunable Ga Content, J. Nanosci. Nanotechnol. 15 (2015) 8388–8394. doi:10.1166/jnn.2015.11473.

[8] A.H. Habib, C.L. Ondeck, P. Chaudhary, M.R. Bockstaller, M.E. McHenry,

Evaluation of iron-cobalt/ferrite core-shell nanoparticles for cancer thermotherapy, J. Appl. Phys. 103 (2008) 7–10. doi:10.1063/1.2830975.

[9] A.S. Lübbe, C. Bergemann, H. Riess, F. Schriever, P. Reichardt, K. Possinger, M. Matthias, B. Dörken, F. Herrmann, R. Gürtler, P. Hohenberger, N. Haas, R. Sohr, B. Sander, a J. Lemke, D. Ohlendorf, W. Huhnt, D. Huhn, Clinical experiences with magnetic drug targeting: a phase I study with 4'-epidoxorubicin in 14 patients with advanced solid tumors., Cancer Res. 56 (1996) 4686–93. http://www.ncbi.nlm.nih.gov/pubmed/8840985.

[10] R.A. Devi, M. Latha, S. Velumani, G. Oza, P. Reyes-Figueroa, M. Rohini, I.G. Becerril-Juarez, J.-H. Lee, J. Yi, Synthesis and Characterization of Cadmium Sulfide Nanoparticles by Chemical Precipitation Method, J. Nanosci. Nanotechnol. 15 (2015) 8434–8439. doi:10.1166/jnn.2015.11472.

[11] M. Rohini, P. Reyes, S. Velumani, M. Latha, G. Oza, I. Becerril-Juarez, R. Asomoza, Parametric optimization of mechanochemical process for synthesis of Cu(In, Ga)0.5Se2 nanoparticles, Mater. Sci. Semicond. Process. (2015) 1–8. doi:10.1016/j.mssp.2015.02.046.

[12] A. Oudhia, {UV}-{VIS} spectroscopy as a nondestructive and effective characterization tool for {II}-{VI} compounds, Recent Res. Sci. Technol. 4 (2012) 109–111.

[13] L.J. van der Pauw, A method of measuring the resistivity and Hall coefficient on lamellae of arbitrary shape, Philips Tech. Rev. 20 (1958) 220–224. doi:537.723.1:53.081.7+538.632:083.9.

[14] A.A. Ramdan, R.D. Gould, A. Ashour, "On the Van der Pauw method of resistivity measurements", Thin Solid Films 239 (1994) 272-275 doi: 004060909490863X.

Chapter 4

Heating-up synthesis of CZTS nanoparticles

In this chapter, we synthesize kesterite CZTS nanoparticles (Nps) by heating-up approach at relatively low reaction temperature (220°C) using single solvent and vacuum free atmosphere. Herein, we discuss about the stoichiometric ($Cu_{2.05}Zn_{1.06}Sn_{0.91}S_{3.96}$) and off-stoichiometric ($Cu_{1.82}Zn_{1.17}Sn_{1.01}S_{3.98}$ (Cu-poor Zn-rich)) composition of CZTS Nps. Moreover, the influence of reaction temperature and time on the structural, morphological, compositional and optical properties are investigated. Besides, based on the detailed time dependent evolution, plausible growth mechanism is proposed for the CZTS Nps.

4.1. Results and discussions for stoichiometric nanoparticles

4.1.1 Influence of reaction temperature

4.1.1.1 Structural properties

XRD patterns of CZTS Nps synthesized at different reaction temperature are shown in Fig. 4.1(a). From the XRD pattern, (112), (020), (220) and (312) planes were observed for all the samples which correspond to kesterite crystal structure of CZTS (JCPDS 01-075-4122). Also, a sample synthesized at 180°C showed (102) plane of Cu_2S phase at 2θ value of 27.32^0 which is due to incomplete reaction at this temperature. As the reaction temperature increases, Cu_2S phase disappeared. As can be seen in Fig. 4.2, Full-width half maximum (FWHM) decreased from 0.64 to 0.3° with increases in the reaction temperature. This behavior indicates the increment in the crystallite and grain size.

The crystallite size was calculated using the Scherrer formula as follows,

$$D = \frac{k\lambda}{\beta cos\theta} \quad \text{----------►} \quad (1)$$

The calculated crystallite size was found to increase from 12.74 to 27.50 nm with increases in the reaction temperature. These results consistent with FE-SEM images which shows an increment in the grain size as a function of reaction temperature.

Raman measurements were carried out to further confirm the phase purity of CZTS Nps since the XRD measurements are unable to distinguish the kesterite CZTS from tetragonal CTS and cubic ZnS due to their similar diffraction peaks. Raman spectra of CZTS Nps synthesized at different reaction temperature are shown in Fig. 4.1(b). The spectra showed a prominent peak at around 334 cm^{-1} and also two shoulder peaks at 285 and 373 cm^{-1}, correspond to kesterite crystal structure of CZTS [1]. The peak at 334 cm^{-1} represents the A_1 symmetry of CZTS and this mode is originated from the pure anionic mode in which S atoms are in motion while Cu, Zn and Sn atoms being at rest. The peak at 285 cm^{-1} is related to the vibration of Zn and S atoms with some contributions from Cu atoms in the CZTS lattice. The peak at 373 cm^{-1} is attributed to the vibration of Sn and S atoms in the CZTS lattice [2–4]. In addition to that, the samples synthesized at 180 and 200°C showed peaks at 477 and 296 cm^{-1} which ascribed to Cu_2S and (Cu_2SnS_3) CTS phases, respectively [5–7]. When the reaction temperature increased to 220°C, secondary phases vanished completely and pure phase of CZTS was obtained. Further increasing the reaction temperature to 240°C, a significant difference was not observed. Thus, the structural analysis revealed that the secondary and ternary phases were observed at low reaction temperatures and the pure phase CZTS obtained after 200°C.

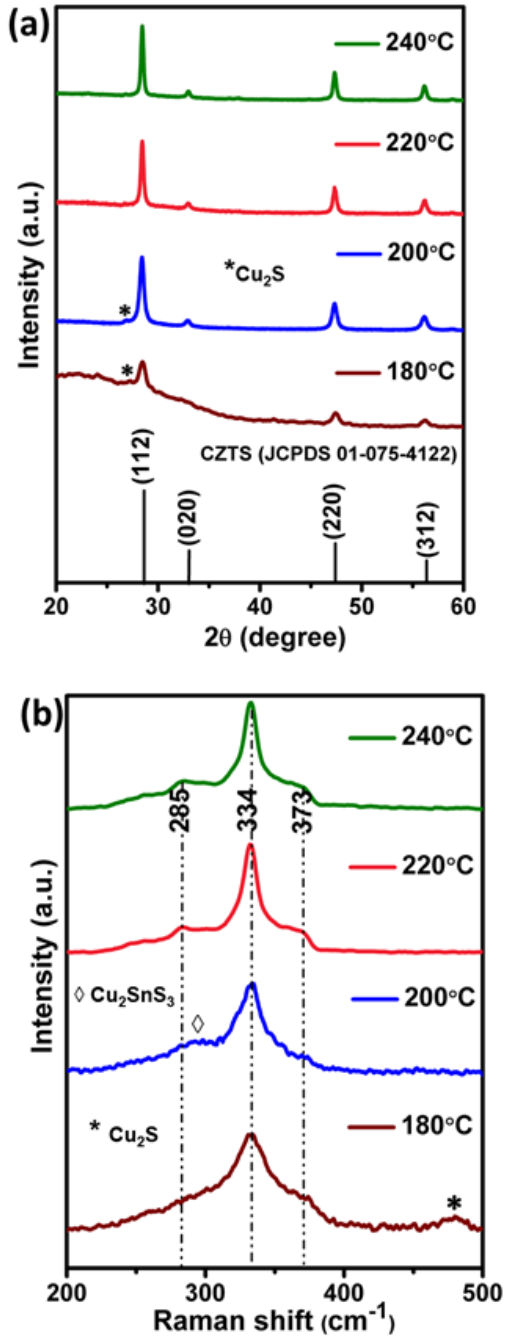

Fig.4.1. (a) XRD pattern and (b) Raman spectra of CZTS Nps synthesized at different reaction temperature.

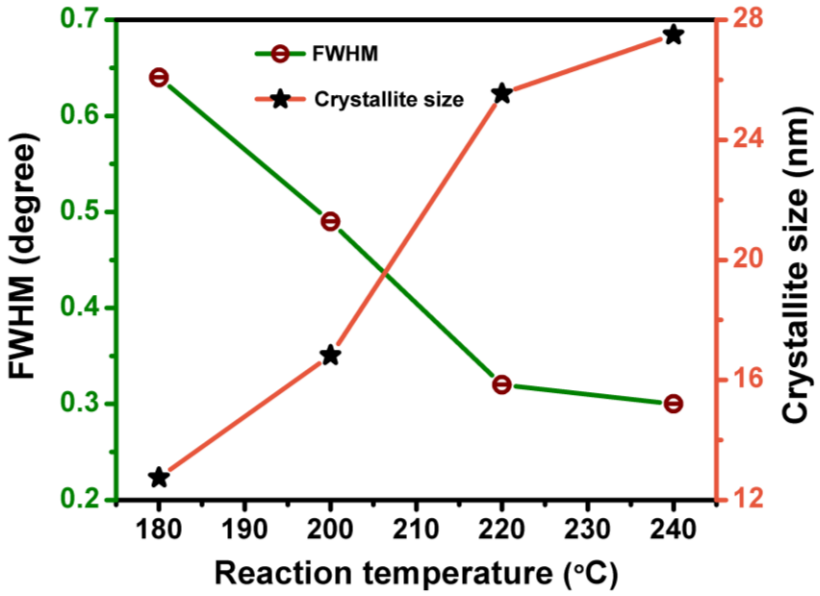

Fig.4.2. Changes in FWHM and crystallite size as a function of reaction temperature.

4.1.1.2 Morphological and compositional properties

FE-SEM images of CZTS Nps synthesized at different reaction temperature are shown in Fig. 4.3. An inhomogeneous size of the particles were observed at low reaction temperatures from 180 to 200°C. As compared to other temperatures, particles were seen distinctively at 220°C. It is worth to mention that generally kesterite CZTS Nps have a polydisperse size distribution [8,9]. This could be due to the fast reaction rate when the S is used as the precursor in which growth and nucleation occur at the same time. Moreover, with increases in the reaction temperature, size of the particles increased from 15 to 45 nm because ions have a greater reactivity at high reaction temperatures which assists the growth of particles.

EDAX analysis was used to investigate the elemental compositions of CZTS Nps synthesized at different reaction temperature. Fig. 4.4 shows the elemental compositions and compositional ratios of Cu/(Zn+Sn) and Zn/Sn. The elemental composition was varied as a function of reaction temperature as shown in Fig. 4.4(a). As the reaction temperature increases, the amount of S

increases while the amount of Cu decreases. When the temperature was less than 220°C, Cu- and Sn- rich composition was observed. As can be seen in Fig. 4.4(b), Cu/(Zn+Sn) ratio decreases while Zn/Sn ratio increases with respect of reaction temperature. Because of these compositional changes, Cu_2S and CTS phases were observed from the structural analysis at low reaction temperatures (180 to 200°C). When the reaction temperature increased to 220°C, stoichiometric composition of CZTS was obtained which is close to the targeted value of 2:1:1:4. Thus, the structural, morphological and compositional analysis revealed that 220°C is the optimum temperature to get pure phase CZTS with the targeted composition.

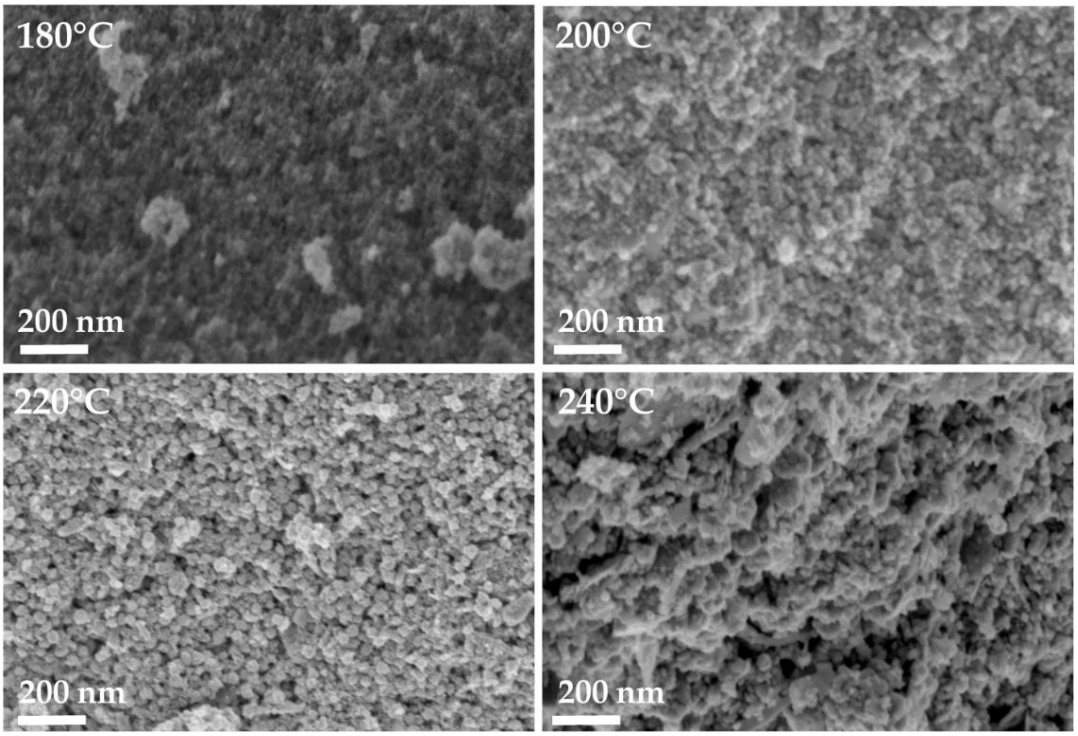

Fig.4.3. FE-SEM images of CZTS Nps synthesized at different reaction temperature.

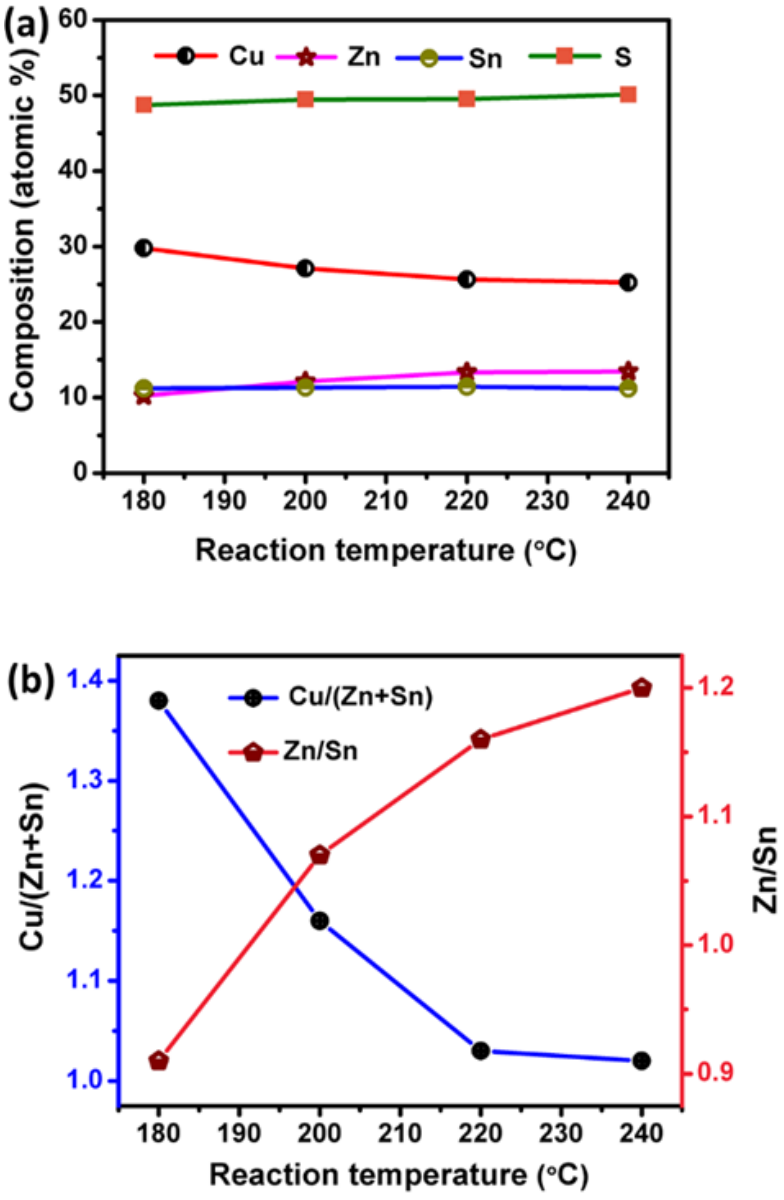

Fig.4.4. (a) The elemental composition and (b) the corresponding ratio of Cu/(Zn + Sn) and Zn/Sn of the CZTS Nps with different reaction temperature.

4.1.2. Influence of reaction time

4.1.2.1 Structural properties

In order to study the growth kinetics of CZTS Nps, aliquots were withdrawn at regular interval from the reaction mixture while the temperature was at 220°C which is the optimum temperature as we discussed in the previous

section. XRD patterns of the samples obtained at different reaction time are shown in Fig. 4.5(a). The peak observed at 2θ values of 28.45, 32.50, 47.20 and 56.50°, correspond to (112), (020), (220) and (312) diffraction planes respectively, of the kesterite crystal structure of CZTS (JCPDS 01-075-4122) for all the samples. Besides, Cu_2S peak observed when the reaction time was less than 30 mins. Further, increasing the reaction time above 30 mins, the Cu_2S peak was not observed by XRD. With increasing the reaction time, FWHM decreased from 0.81 to 0.31° as shown in Fig. 4.6, indicating the improvement in the crystallite and grain size. The crystallite size was calculated using the Scherrer formula as described in the previous section. The calculated crystallite size tend to increase from 10.09 to 25.46 nm with increases in the reaction time.

Raman analysis was further used to confirm the phase purity of the CZTS NPs. Raman spectra measurements of CZTS Nps for different reaction time are shown in Fig. 4.5(b). The spectra showed a prominent peak at around 335 cm^{-1} and two shoulder peaks at 285 and 374 cm^{-1} for all the samples which correspond to kesterite crystal structure of CZTS [1]. Besides, a secondary phase of Cu_2S peak was observed at 475 cm^{-1} [5] for the sample synthesized at different reaction time from 5 to 30 mins. Further increases in the reaction time, the intensity of the Cu_2S peak decreased which is due to the phase conversion from Cu_2S to CTS. Thus, CTS phase was observed at 296 cm^{-1} for 30 mins, 1 and 2 h. As the reaction proceeds for 4 and 8 h, pure phase kesterite CZTS was obtained. Hence, the structural analysis revealed that compositional phase evolved from Cu_2S, then to CTS intermediate compound, finally to pure kesterite CZTS Nps.

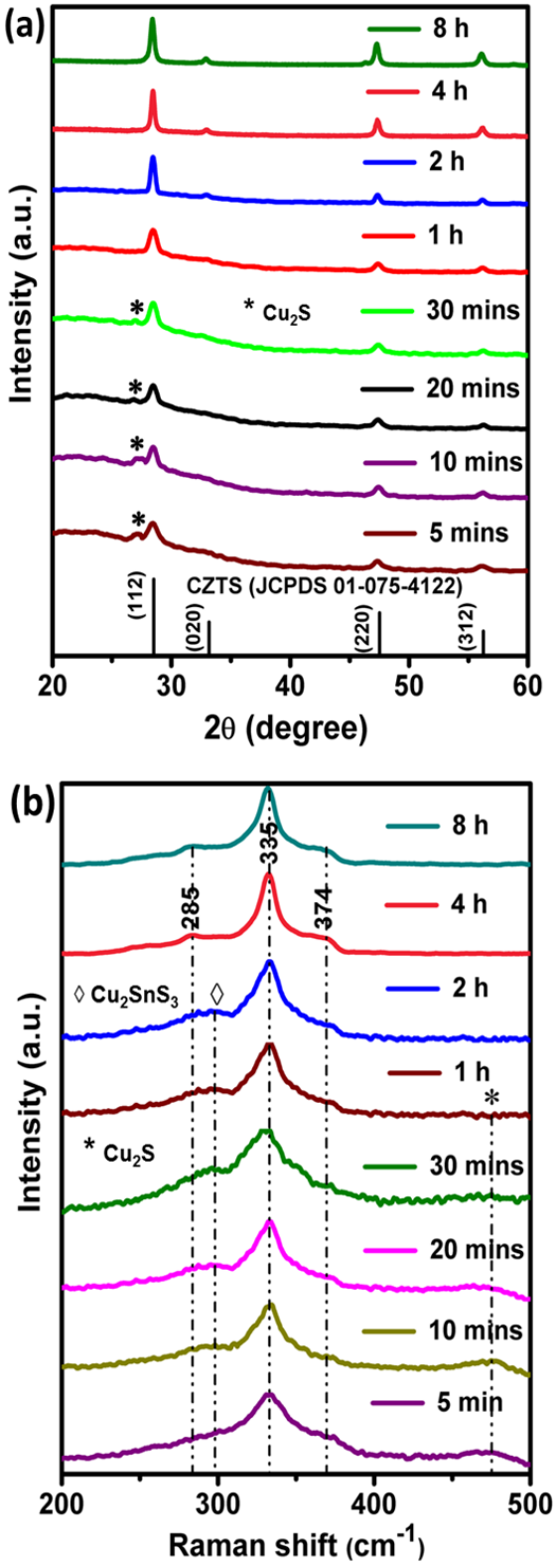

Fig.4.5. (a) XRD pattern and (b) Raman spectra of CZTS Nps synthesized at 220°C for different reaction time.

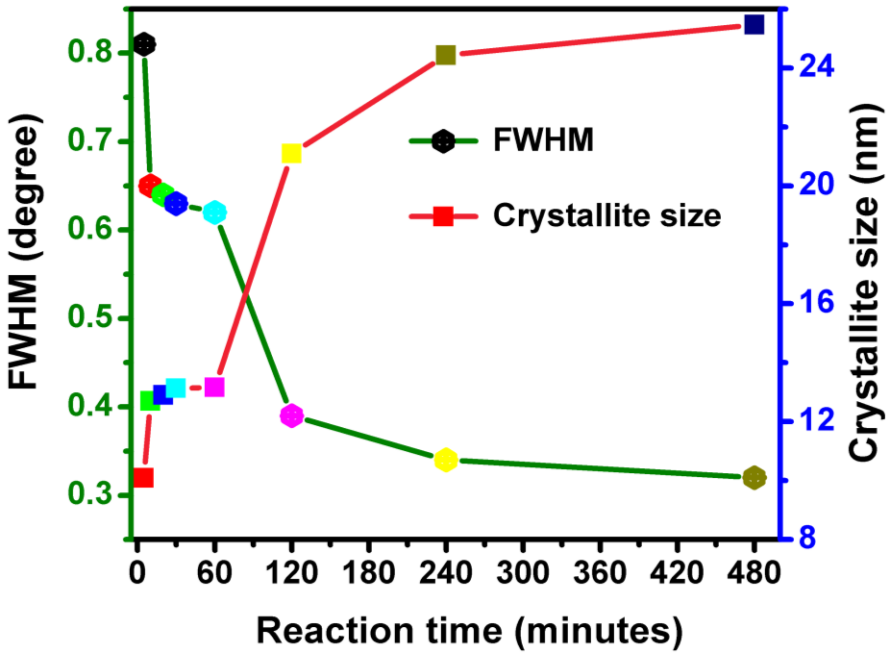

Fig.4.6. Variation in FWHM and crystallite size as a function of reaction time.

4.1.2.2 Morphological and compositional properties

In order to ascertain the growth of CZTS Nps, the time-dependent evolution of morphology was obtained by TEM. As can be seen in Fig. 4.7, Nps were formed even at 5 mins, indicating a fast reaction rate. The polydispersity of the Nps was observed at lesser reaction times from 5 mins to 2 h and size of the particles were in the range between 10 and 25 nm. When the reaction time increases up to 4h, the homogeneous size of the particles was obtained as compared to other reaction times and the particles size is about 30 nm. Further, increases the reaction time up to 8 h, particle size increased to 40 nm. Thus, the morphological analysis revealed that particles sizes are getting bigger with increasing reaction time. This behavior could be due to Ostwald ripening, in which the large particles grow at the expense of the dissolution of smaller particles.

Fig. 4.8, illustrated the elemental compositions and compositional ratios of Cu/(Zn+Sn) and Zn/Sn. As can be seen in Fig. 4.8(a), the elemental composition was varied with increasing reaction time. The amount of S increases while the

amount of Cu decreases as the reaction proceeds. When the reaction time was less than 30 mins, Cu- and Zn-rich composition was observed. With increases in reaction time, the amount of Sn increases. The Cu/(Zn+Sn) and Zn/Sn ratio were decreased as the reaction proceeds. Thus the compositional changes led to the formation of secondary and ternary phases of Cu_2S and CTS as can be detected by the structural analysis. When the reaction time increased to 4h, stoichiometric composition of pure phase CZTS was obtained which is very close to the targeted value of 2:1:1:4.

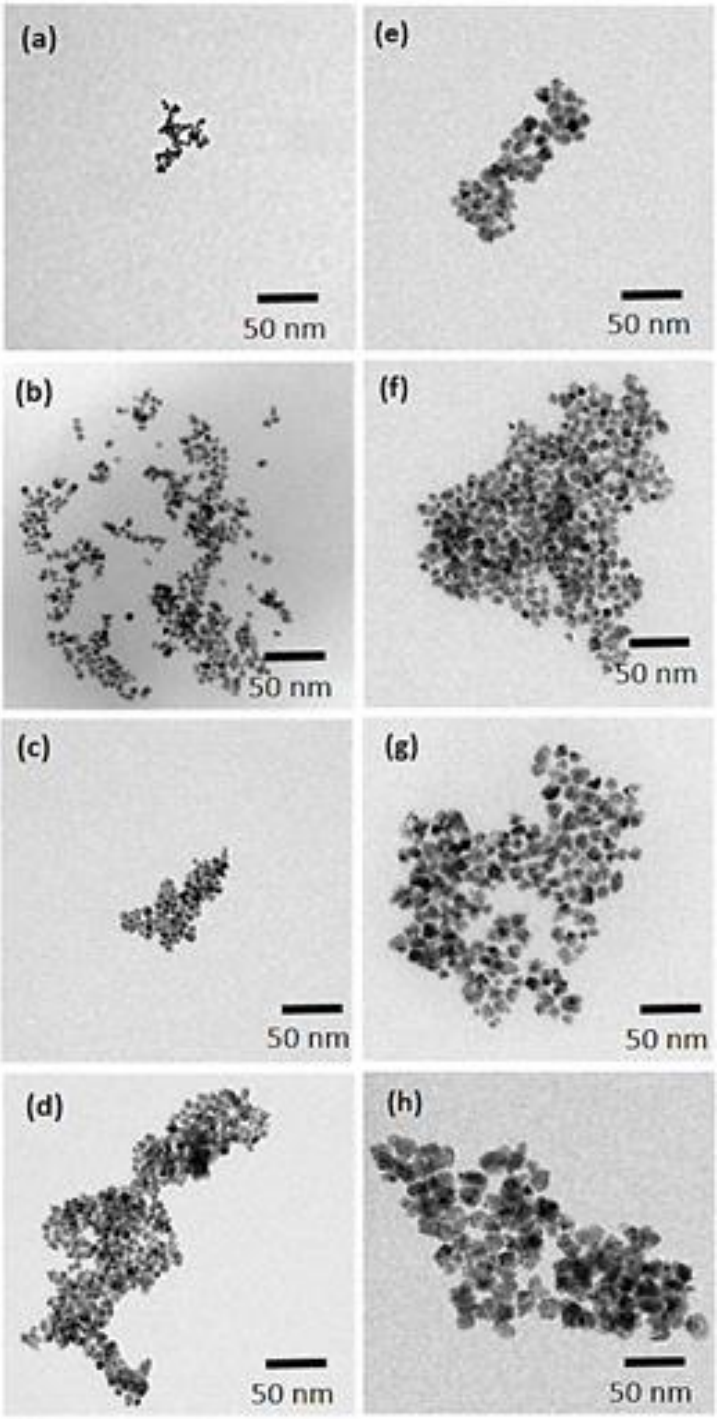

Fig.4.7. TEM images of CZTS Nps synthesized at 220°C for different reaction time: (a) 5 mins, (b) 10 mins, (c) 20 mins, (d) 30 mins, (e) 1 h, (f) 2 h, (g) 4 h and (h) 8 h.

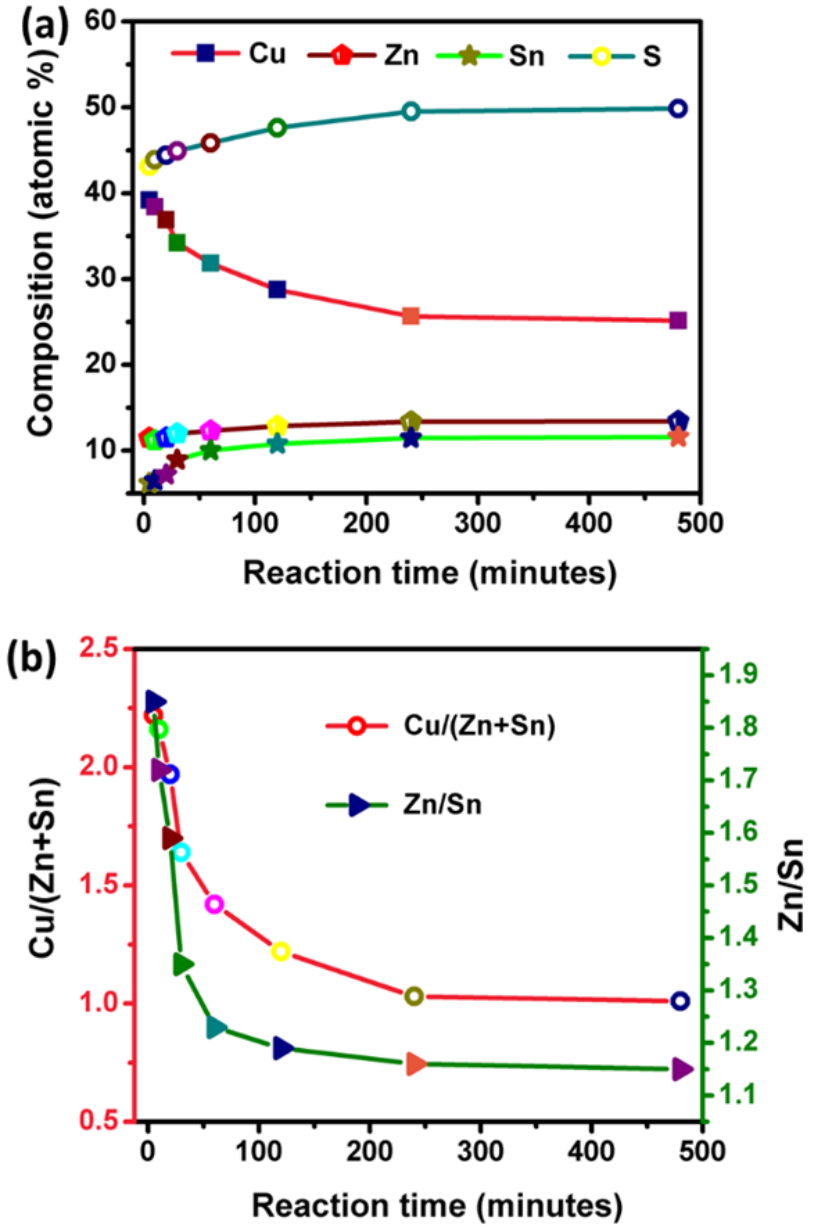

Fig.4.8. (a) The elemental composition and (b) the corresponding ratio of Cu/(Zn + Sn) and Zn/Sn of the CZTS Nps synthesized at 220°C for different reaction time.

FE-SEM-EDAX elemental mappings for CZTS Nps synthesized at 4 h are shown in Fig. 4.9(a). The Cu, Zn, Sn and S elements were homogeneously distributed in the selected area of the Nps which suggested that the nanoparticles have a uniform composition without any segregation of elements.

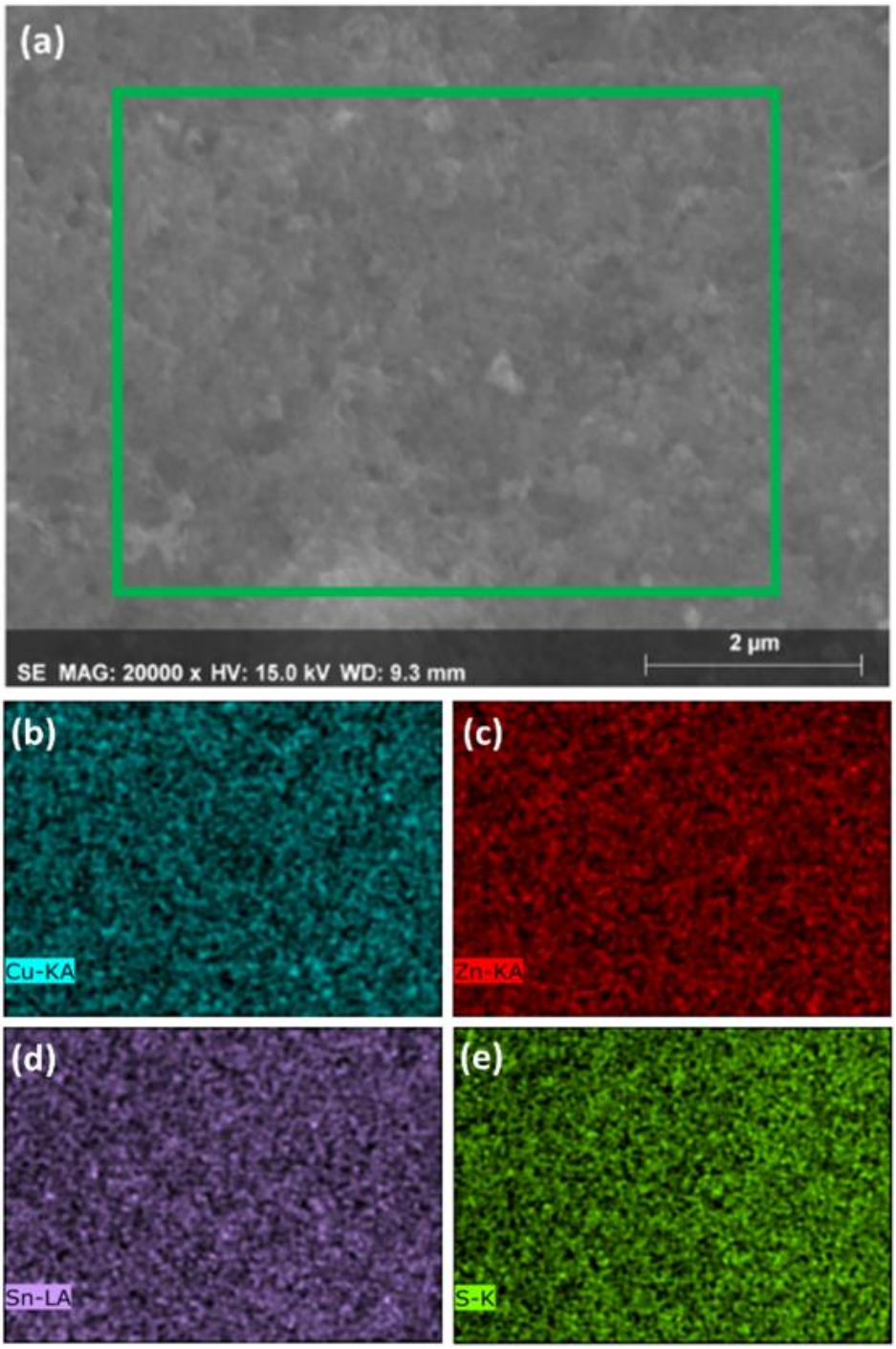

Fig. 4.9. (a) FE-SEM-EDAX image of the selected area, (b-e) elemental mapping of Cu, Zn, Sn and S respectively.

4.1.2.3 Optical properties

The UV-VIS-NIR absorption spectra of the CZTS Nps obtained at 4 h is shown in Fig. 4.10(f). The obtained CZTS Nps exhibited a strong optical absorption in the visible region. The optical band gap E_g was estimated from the following formula

$$(\alpha h\upsilon)^2 = \alpha(h\upsilon - E_g) \quad \text{----------} \quad (4.1)$$

Where, α=absorption coefficient, hυ=photon energy. The optical band gap was obtained by plotting $(\alpha h\upsilon)^2$ as a function of hυ as shown in Fig. 4.10(g). The calculated band gap was found to be 1.50 eV which is well consistent with the literature values [10,11].

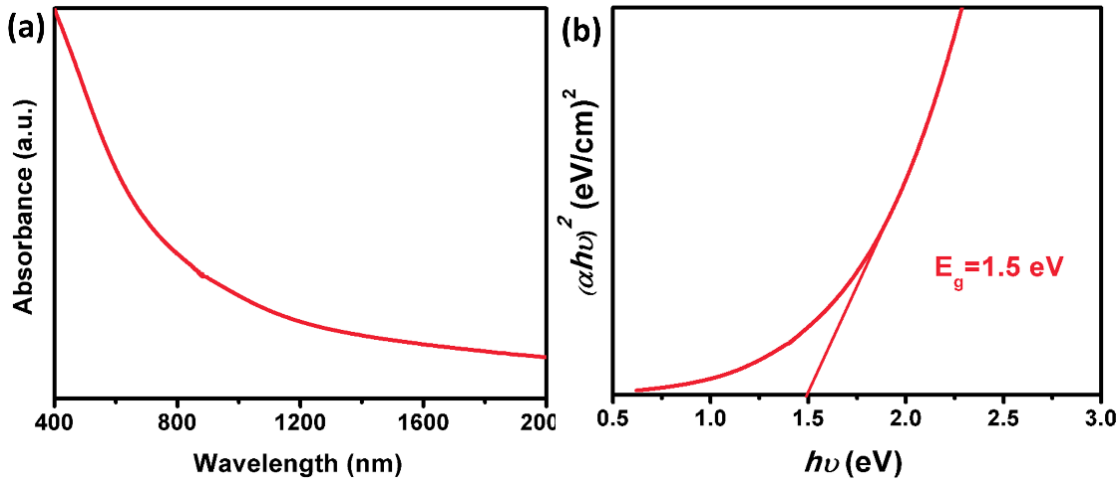

Fig.4.10. (a) UV-Vis-NIR absorption spectrum, (b) corresponding band gap of CZTS Nps synthesized at 4 h.

4.1.2.4 Growth and formation mechanism

On the basis of the above-mentioned detailed time-dependent structural and compositional evolutions, a possible growth mechanism was proposed. The evolution pathway of pure phase CZTS Nps can be divided into three steps.

(i) The rapid formation of Cu_2S nuclei was observed.

(ii) Then, the diffusion of Sn^{4+} ions into Cu_2S to form the intermediate compounds of CTS.

(iii) Finally, the pure phase of CZTS Nps was obtained followed by the diffusion of Zn^{2+} cations into CTS.

During the typical growth process, the precursors were mixed with OLA at room temperature and then heated to 220°C. With magnetic stirring, metal ions (Lewis acid) coordinated with S (Lewis base) to form a metal-S complexes, which would decompose into corresponding sulfides at a certain temperature. The Cu-rich composition was observed from the Fig. 4.8(a), which leads to the formation of Cu_2S phase at less reaction times from 5 to 30 mins. Generally, in Cu-based chalcogenides, the Cu_2S nuclei was observed in the initial stage by other researchers [12]. The Cu ions in Cu_2S have relatively high mobility, which can facilitate an exchange with other metal ions as the reaction time progress. When the reaction time increased to 1 and 2 h, Sn^{4+} was gradually incorporated into the Cu_2S crystal lattice to form the intermediate compound of Cu–Sn–S, which was confirmed from Cu/(Zn + Sn) ratio evolutions (Fig. 4.8(b)). At the same time, the CTS phase detected from structural analysis. Subsequently the diffusion of Zn^{2+} into Cu–Sn–S particles to form the CZTS Nps. When the time increased to 4 h, the stoichiometric composition was obtained. Morphology analysis showed more uniform sized particles at 4 h than lesser reaction times. Further increasing reaction time up to 8 h, a significant difference was not observed. Thus, the results suggested that 4 h is the optimum to get kesterite CZTS Nps with pure phase, controlled composition and homogeneous particle size.

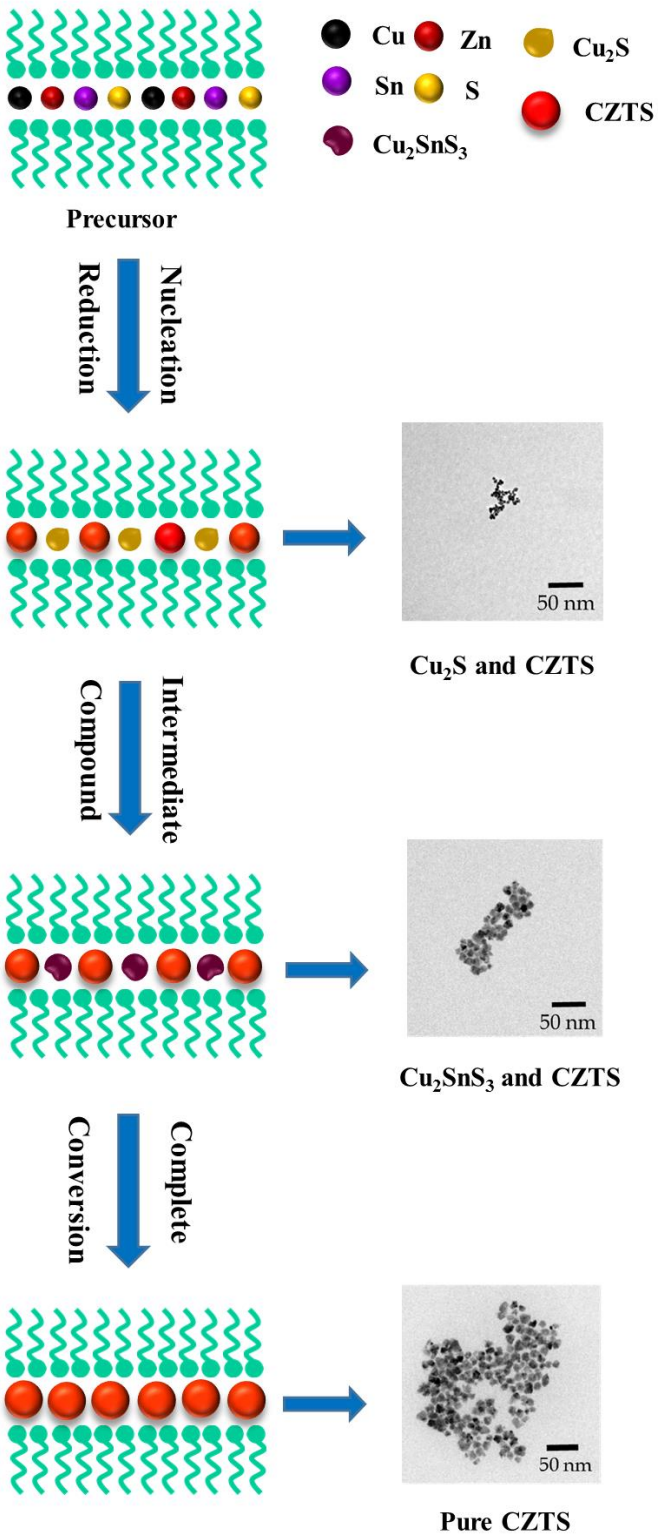

Fig.4.11. Growth and formation mechanism of CZTS Nps synthesized via heating-up approach.

4.2. Results and discussions for off-stoichiometric nanoparticles

4.2.1 Structural properties

XRD pattern of CZTS Nps synthesized at 220°C for 4 h is shown in Fig. 4.12(a). From the XRD spectrum, (112), (020), (220), (312) and (224) planes were observed, correspond to kesterite crystal structure of CZTS (JCPDS 01-075-4122). Raman analysis was performed to further confirm the phase purity of CZTS Nps. As can be seen in Fig. 4.12(b), Raman spectrum shows a prominent peak at around 332 cm^{-1} and two shoulder peaks at 284 and 370 cm^{-1}, related to the kesterite crystal structure of CZTS. The peak at 332 cm^{-1} ascribed to A_1 optical phonon vibrational mode of CZTS and this mode was originated from the vibration of S atoms in the CZTS lattice. The peak at 284 cm^{-1}, attributed to the vibration of Zn and S atoms with some contributions from Cu atoms. The peak at 370 cm^{-1} correspond to the vibration of Sn and S atoms in the CZTS lattice [26-28]. From the Raman spectrum, secondary and ternary phases such as Cu_2S (475 cm^{-1}), SnS_2 (315 cm^{-1}), ZnS (278 and 351 cm^{-1}), Cu_2SnS_3 (297 and 337 cm^{-1}), and Cu_3SnS_4 (318 cm^{-1}) were not observed suggesting the high purity of the synthesized CZTS material. Thus, the structural analysis revealed the formation of pure phase CZTS Nps.

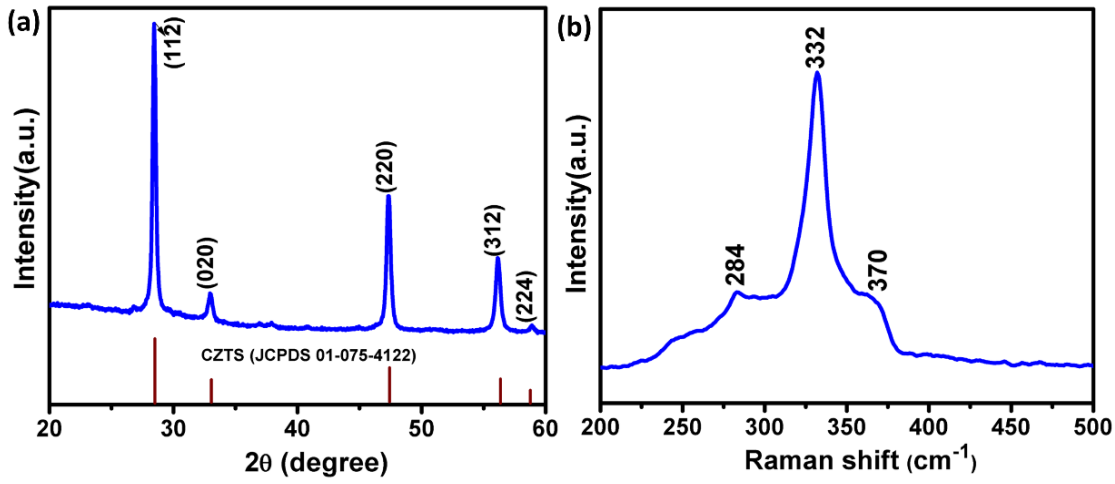

Fig.4.12. (a) XRD pattern and (b) Raman spectra of CZTS Nps synthesized at 220°C for 4 h.

4.2.2 Morphological and compositional properties

FE-SEM image of kesterite CZTS Nps synthesized at 220°C for 4 h is shown in Fig. 4.13(a). From the FE-SEM image, nearly spherical size of the particles were observed with size ranging from 25 to 30 nm. EDAX analysis was used to study the elemental composition of CZTS Nps. Fig. 4.13(b) showed the composition of Cu, Zn, Sn and S which is close to the targeted values. Moreover, the calculated Cu/(Zn+Sn) ratio is 0.83 and the Zn/Sn ratio is 1.16 which reveals the Cu-poor, Zn-rich composition. Here, it is worth to mention that the high efficiency solar cell is reported with Cu-poor, Zn-rich composition [13]. FE-SEM-EDAX elemental mapping was performed to identify the elemental distributions of CZTS Nps as shown in Fig. 4.13(c). From the Fig. 4.13(d-g), we could observe that the Cu, Zn, Sn and S elements were homogeneously distributed among the Nps which revealed that the nanoparticles have a uniform composition without existence of compositional gradients in the selected area.

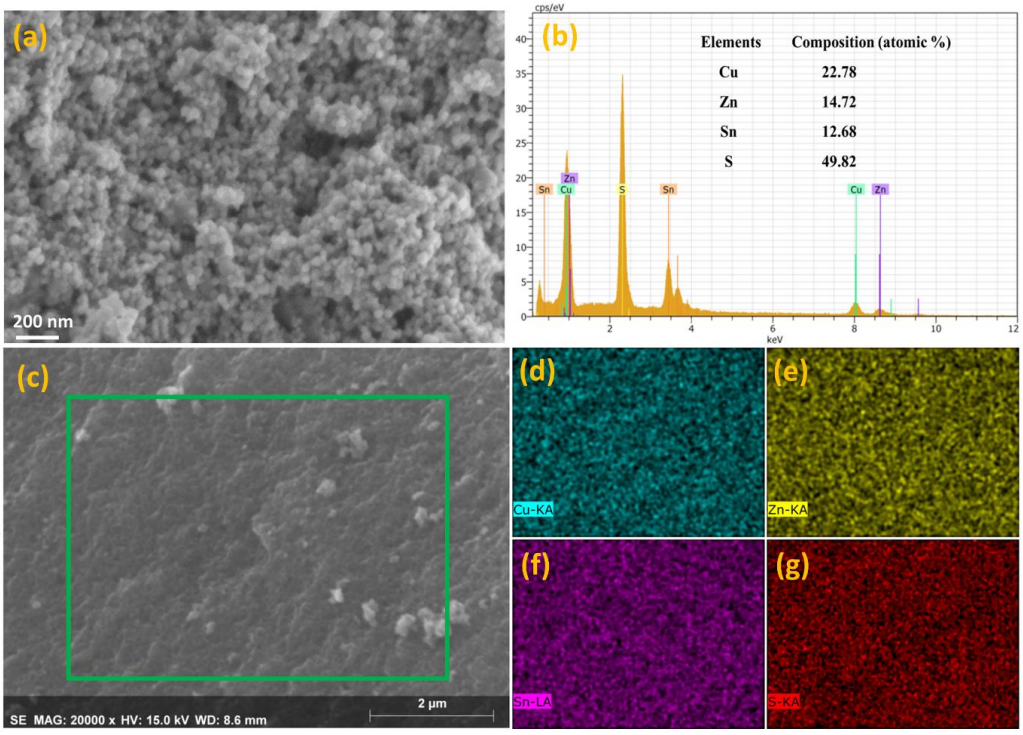

Fig.4.13. (a) FE-SEM image, (b) EDAX composition, (c) FE-SEM-EDAX image of the selected area, (d-g) elemental mapping of Cu, Zn, Sn and S respectively.

4.2.3 HR-TEM analysis

HR-TEM analysis was performed for CZTS Nps prepared under off-stoichiometric condition. From the Fig. 4.14(a), it is clearly seen that the formation of particles were spherical in shape and size of the particle is about 25 nm. These particles possess well crystalline domains as can be seen in Fig. 4.14(b), through the resolved crystal-lattice fringes for the consider samples. The lattice fringes give d-spacing of 0.31 nm which is closely related to (112) crystallographic plane.

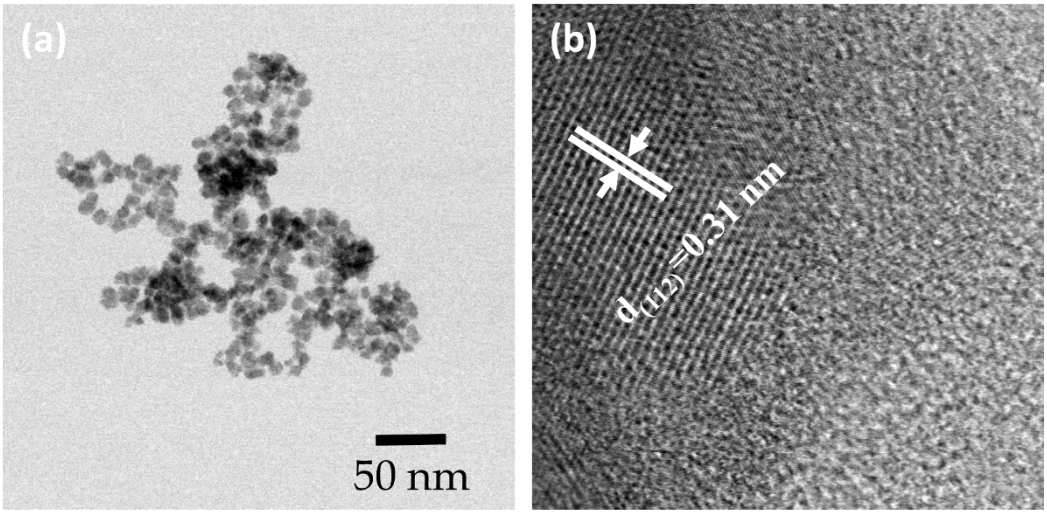

Fig.4.14. (a) HR-TEM image of CZTS Nps and (b) lattice inter-planar distances for the plane (112).

High angle annular dark-field (HAADF) experiments along with EDAX line mapping were carried out in scanning transmission electron microscope (STEM) for the CZTS Nps. The STEM image with corresponding EDAX mapping can be seen in Fig.4.15, where it can be seen clearly that Cu, Zn, Sn and S homogenously observed along particle with line profile mapping. STEM-EDAX reveled the elemental composition of CZTS Nps as shown in table 4.1, which is close to the targeted value.

Table 4.1. EDAX composition of CZTS Nps

CZTS	EDAX			
	Cu	Zn	Sn	S
	22.22	14.24	12.63	50.91

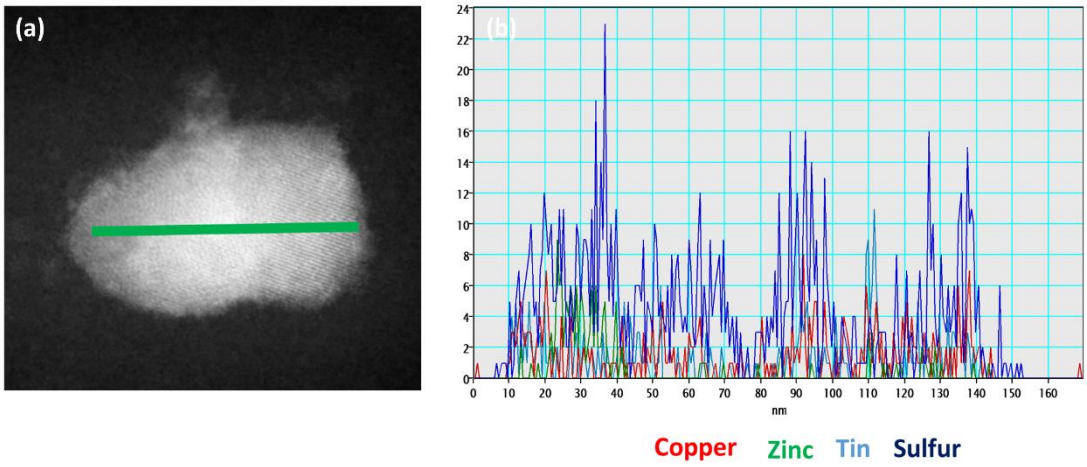

Fig.4.15. (a) EDAX line scan of the particle and (b) Line profile elemental mapping in STEM mode.

4.2.4 Optical analysis

The UV-VIS-NIR absorption spectroscopy was used to examine the optical properties of CZTS Nps. As can be seen in Fig. 4.16(a), the synthesized CZTS Nps revealed a broad absorption in the visible region, suggesting their potential application in the field of solar cells. The optical band gap (Eg) was calculated by extrapolating the linear part of the function $(\alpha h\upsilon)^2$ versus energy ($h\upsilon$) where, α = absorbance coefficient, $h\upsilon$=photon energy as shown in Fig. 4.16(b). The obtained optical band gap is about 1.49 eV which is in good agreement with the literature value [14]. Hence, the results suggested that pure phase CZTS Nps by the absence of secondary and ternary phases of ZnS (3.7 eV) and Cu_2SnS_3 (0.93 eV) [15,16].

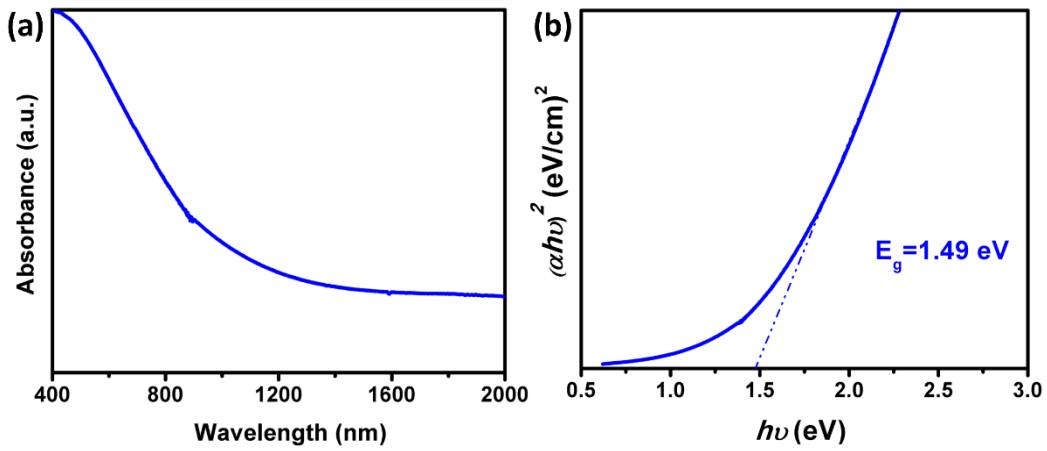

Fig.4.16. (a) UV-Vis-NIR absorption spectrum, (b) corresponding band gap of CZTS Nps synthesized at 4 h.

4.2.5 XPS analysis

XPS was employed to investigate the valence states of all four elements in the synthesized CZTS Nps at an optimized reaction time of 4 h. The XPS analysis shows the presence of Cu 2p, Zn 2p, Sn 3d and S 2p elements in the CZTS Nps. As can be seen in Fig. 4.16, Cu 2p spectrum shows two peaks at 951.52 and 931.65 eV with a splitting of 19.87 eV, which is in good agreement with the standard separation (19.9 eV) of Cu(I). The Zn 2p peaks located at 1045.16 and 1022.06 eV with a split orbit of 23.10 eV, which ascribed to Zn(II). The Sn 3d peaks appeared at 495.13 and 486.65 eV with a split orbit of 8.48 eV, indicates Sn (IV). The S 2p peaks showed binding energies at 162.38 and 161.26 eV with a split orbit of 1.12 eV, which is consistent with the binding energy of S in the sulfide state in CZTS. These results were in good agreement with the reported values of the binding state of the elements of CZTS [17][18][19].

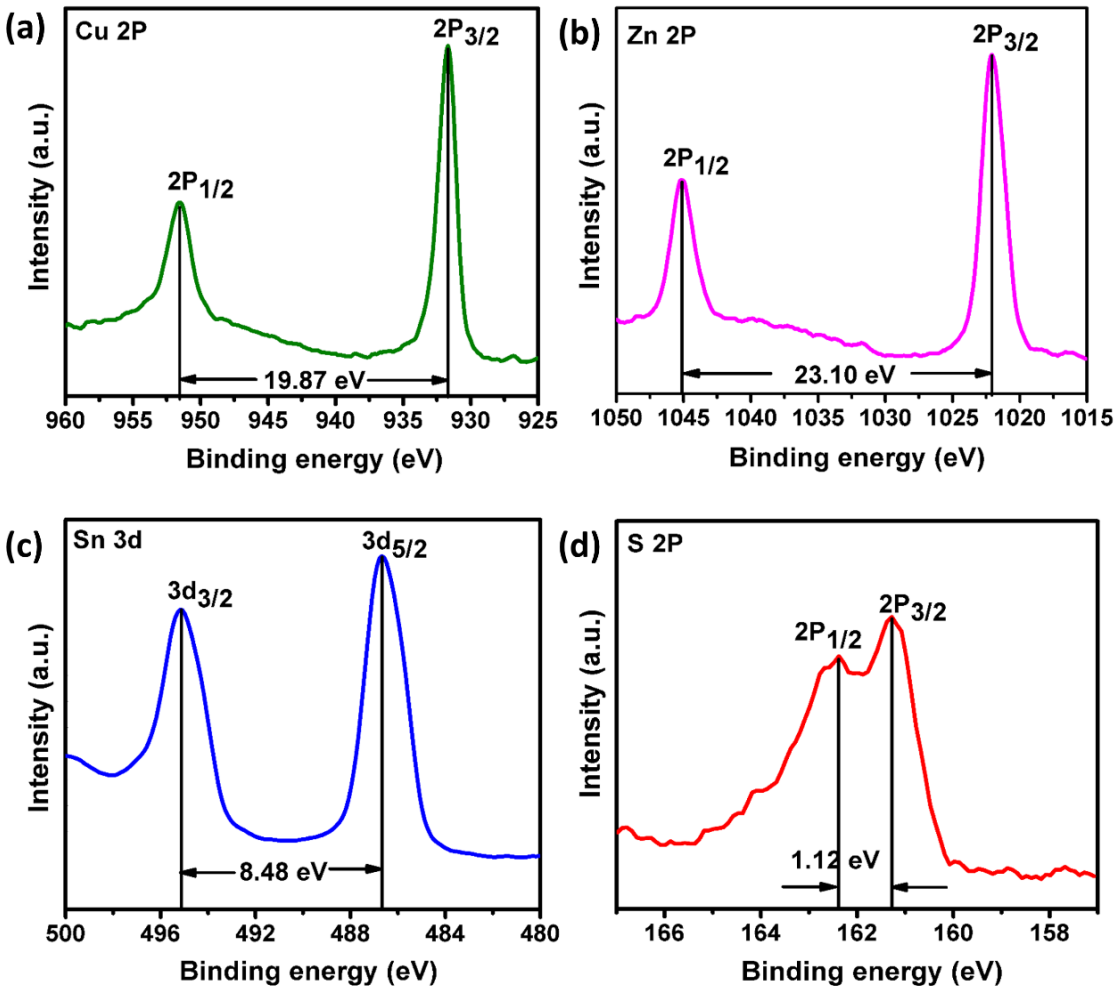

Fig.4.17 (a-d) XPS spectra of CZTS Nps for 4 h: Cu 2P, Zn 2P, Sn 3d, and S 2p respectively.

4.3. Summary

- Stoichiometric ($Cu_{2.05}Zn_{1.06}Sn_{0.91}S_{3.96}$) and off-stoichiometric ($Cu_{1.82}Zn_{1.17}Sn_{1.01}S_{3.98}$) composition of CZTS Nps were synthesized by heating-up approach. For the stoichiometric conditions, reaction temperatures such as temperature and time were varied to study their influences on the structural, morphological and compositional properties. On the basis of the detailed

time-dependent phase evolution, a plausible growth and formation mechanism was proposed.

- CZTS Nps were synthesized by varying the reaction temperatures such as 180, 200, 220 and 240^{0}C with constant reaction time of 4h. Structural analysis revealed that the secondary and ternary phases at low reaction temperatures. When the reaction temperature increased to 220°C, secondary and ternary phases vanished completely and pure phase of CZTS was obtained. Morphological analysis showed homogeneous size of the particles at 220°C as compared to other temperatures. From the compositional analysis, Cu- and Sn- rich composition was observed. Because of these compositional changes, Cu_2S and CTS phases were observed from the structural analysis at low reaction temperatures (180 to 200°C). When the reaction temperature increased to 220°C, stoichiometric composition of CZTS was obtained which is close to the targeted value of $Cu_{2.05}Zn_{1.06}Sn_{0.91}S_{3.96}$. Thus, the structural, morphological and compositional analysis revealed that 220°C is the optimum temperature to get pure phase CZTS with the targeted composition.
- In order to study the growth kinetics of CZTS Nps, aliquots were withdrawn from the reaction mixture at 220°C for different time such as 5 mins, 10 mins, 20 mins, 30 mins, 1 h, 2 h, 4 h and 8 h). From the structural analysis, secondary phase of Cu_2S peak was observed from 5 to 30 mins. Further increases in the reaction time, the intensity of the Cu_2S peak decreased which is due to the phase conversion from Cu_2S to CTS. As the reaction proceeds to 4 h, pure phase kesterite CZTS was obtained. The morphological analysis revealed that particles sizes are getting bigger with increasing reaction time which could be due to Ostwald ripening. When the reaction time was less than 30 mins, Cu- and Zn-rich composition was observed. With increases in the reaction time, the amount of Sn increases. Also, Cu and Zn composition reached the theoretical value. Further, increasing the reaction time to 4 h, stoichiometric composition of CZTS was obtained which is very close to the

targeted value. The time-dependent experiments revealed that the compositional phase evolved from Cu_2S through the Cu_2SnS_3 intermediate compound to kesterite CZTS NCs. Hence, the results suggested that 4 h is the optimum time to get pure phase CZTS Nps.

- We also synthesized off-stoichiometric (Cu-poor Zn-rich) CZTS Nps at 220°C for 4 h. Because, Cu-poor Zn-rich composition enhances the efficiency of the solar cell as compared to stoichiometric composition. Structural analysis revealed a pure phase CZTS Nps. FE-SEM analysis showed a spherical shape of the particles. From the EDAX analysis, off-stoichiometric composition was obtained which is close to the targeted value of $Cu_{1.82}Zn_{1.17}Sn_{1.01}S_{3.98}$. The observed binding energies from the XPS analysis is consistent with the literature. Optical analysis exhibited the band gap of 1.49 eV, which is an optimum value for solar cell applications.

References

[1] V.T. Tiong, J. Bell, H. Wang, One-step synthesis of high quality kesterite Cu_2ZnSnS_4 nanocrystals - a hydrothermal approach, Beilstein Journal of Nanotechnology. 5 (2014) 438–446. doi:10.3762/bjnano.5.51.

[2] R. Saravana Kumar, B.D. Ryu, S. Chandramohan, J.K. Seol, S.K. Lee, C.H. Hong, Rapid synthesis of sphere-like Cu_2ZnSnS_4 microparticles by microwave irradiation, Materials Letters. 86 (2012) 174–177. doi:10.1016/j.matlet.2012.07.059.

[3] K. Mokurala, P. Bhargava, S. Mallick, Single step synthesis of chalcogenide nanoparticles Cu_2ZnSnS_4, Cu_2FeSnS_4 by thermal decomposition of metal precursors, Materials Chemistry and Physics. 147 (2014) 371–374. doi:10.1016/j.matchemphys.2014.06.049.

[4] A. Khare, B. Himmetoglu, M. Johnson, D.J. Norris, M. Cococcioni, E.S. Aydil, Calculation of the lattice dynamics and Raman spectra of copper zinc tin chalcogenides and comparison to experiments, Journal of Applied Physics. 111 (2012). doi:10.1063/1.4704191.

[5] M. Zhou, Y. Gong, J. Xu, G. Fang, Q. Xu, J. Dong, Colloidal CZTS nanoparticles and films: Preparation and characterization, Journal of Alloys and Compounds. 574 (2013) 272–277. doi:10.1016/j.jallcom.2013.05.143.

[6] J. Han, S.W. Shin, M.G. Gang, J.H. Kim, J.Y. Lee, Crystallization behaviour of co-sputtered $CuZnSnS_4$ precursor prepared by sequential sulfurization processes., Nanotechnology. 24 (2013) 95706. doi:10.1088/0957-4484/24/9/095706.

[7] V.T. Tiong, Y. Zhang, J. Bell, H. Wang, Phase-selective hydrothermal synthesis of Cu_2ZnSnS_4 nanocrystals: the effect of the sulphur precursor, CrystEngComm. 16 (2014) 4306–4313. doi:10.1039/C3CE42606H.

[8] C. Steinhagen, M.G. Panthani, V. Akhavan, B. Goodfellow, B. Koo, B.A.

Korgel, Synthesis of Cu_2ZnSnS_4 Nanocrystals for Use in Low-Cost Photovoltaics, (2009) 12554–12555. doi:10.1021/ja905922j.

[9] Z. Li, A.L.K. Lui, K.H. Lam, L. Xi, Y.M. Lam, Phase-Selective Synthesis of Cu_2ZnSnS_4 Nanocrystals using Different Sulfur Precursors, Inorganic Chemistry. 53 (2014) 10874–10880. doi:10.1021/ic500956n.

[10] Q. Guo, H.W. Hillhouse, R. Agrawal, Synthesis of Cu_2ZnSnS_4 nanocrystal ink and its use for solar cells, Journal of the American Chemical Society. 131 (2009) 11672–11673. doi:10.1021/ja904981r.

[11] X. Wang, Z. Sun, C. Shao, D.M. Boye, J. Zhao, A facile and general approach to polynary semiconductor nanocrystals via a modified two-phase method., Nanotechnology. 22 (2011) 245605. doi:10.1088/0957-4484/22/24/245605.

[12] C. Coughlan, K.M. Ryan, Complete study of the composition and shape evolution in the synthesis of Cu_2ZnSnS_4 (CZTS) semiconductor nanocrystals, CrystEngComm. 17 (2015) 6914–6922. doi:10.1039/C5CE00497G.

[13] W. Wang, M.T. Winkler, O. Gunawan, T. Gokmen, T.K. Todorov, Y. Zhu, D.B. Mitzi, Device characteristics of CZTSSe thin-film solar cells with 12.6% efficiency, Advanced Energy Materials. 4 (2014) 1–5. doi:10.1002/aenm.201301465.

[14] W. Xie, X. Jiang, C. Zou, D. Li, J. Zhang, J. Quan, L. Shao, Synthesis of highly dispersed Cu_2ZnSnS_4 nanoparticles by solvothermal method for photovoltaic application, Physica E: Low-Dimensional Systems and Nanostructures. 45 (2012) 16–20. doi:10.1016/j.physe.2012.05.022.

[15] J.X. Ding, J.A. Zapien, W.W. Chen, Y. Lifshitz, S.T. Lee, X.M. Meng, Lasing in ZnS nanowires grown on anodic aluminum oxide templates, Applied Physics Letters. 85 (2004) 2361–2363. doi:10.1063/1.1791326.

[16] S.C. Riha, B.A. Parkinson, A.L. Prieto, Solution-Based Synthesis and Characterization of Cu_2ZnSnS_4 Nanocrystals, Journal of the American

Chemical Society. 131 (2009) 12054–12055. doi:10.1021/ja9044168.

[17] S. Zhang, C. Wang, L. Sun, A. Lu, X. Xu, H. Xing, X. Chen, Fabrication of single-crystal/phase Cu_2ZnSnS_4 nanorods via a two-step spin coating route, Applied Physics Express. 8 (2015). doi:10.7567/APEX.8.035202.

[18] M. Li, W.H. Zhou, J. Guo, Y.L. Zhou, Z.L. Hou, J. Jiao, Z.J. Zhou, Z.L. Du, S.X. Wu, Synthesis of pure metastable wurtzite CZTS nanocrystals by facile one-pot method, Journal of Physical Chemistry C. 116 (2012) 26507–26516. doi:10.1021/jp307346k.

[19] M.D. Regulacio, C. Ye, S.H. Lim, M. Bosman, E. Ye, S. Chen, Q.H. Xu, M.Y. Han, Colloidal nanocrystals of wurtzite-type Cu_2ZnSnS_4: Facile noninjection synthesis and formation mechanism, Chemistry - A European Journal. 18 (2012) 3127–3131. doi:10.1002/chem.201103635.

Chapter 5
Deposition and selenization of CZTS thin films using heating-up synthesis of CZTS nanoparticles

Herein, we deposit CZTS thin films using off-stoichiometric ($Cu_{1.82}Zn_{1.17}Sn_{1.01}S_{3.98}$ (Cu-poor Zn-rich)) CZTS Nps, synthesized by heating-up process as we discussed in chapter 4. For this purpose, CZTS ink has been formulated using hexanethiol as a solvent. Influence of powder concentration is studied on the morphological properties of the CZTS films. As well, the effect of annealing temperature on the properties of CZTS films are described. Furthermore, the optimum powder concentration (0.05 g) and annealing temperature (350°C) of CZTS films are used for selenization process. Besides, the influence of selenization temperature on the CZTS films is investigated by examining their structural, morphological, compositional, optical and electrical properties.

5.1. Formulation of $Cu_{1.82}Zn_{1.17}Sn_{1.01}S_{3.98}$ particle-based ink

We formulated the ink using CZTS Nps to deposit thin films by doctor-blade method. As-synthesized CZTS Nps were dispersed in hexanethiol by ultra-sonication. Besides, CZTS powder concentration was varied such as 0.2, 0.1 and 0.05 g in 1 mL hexanethiol to achieve the crack-free films. Then, the ink was coated as a thin film onto soda-lime glass substrates using the doctor-blade method. Experimental conditions were same as described in section 3.1.2.

5.2. Results and discussions

5.2.1. As-deposited thin films

5.2.1.1. Structural properties

CZTS films were deposited onto soda-lime glass substrates using the doctor-blade method with the powder concentration of 0.2, 0.1 and 0.05 g in 1 mL hexanethiol. The properties of as-deposited films were described.

Structural properties of as-deposited CZTS films for different powder concentrations are shown in Fig. 5.1. XRD pattern shows the (112), (220) and (312) planes of kesterite CZTS for all the samples as observed in the powder. It indicates that crystalline properties of CZTS powder were successfully transferred to the film. As can be seen in Fig. 5.1(a), intensity of the diffraction peaks were reduced with decreasing powder concentration.

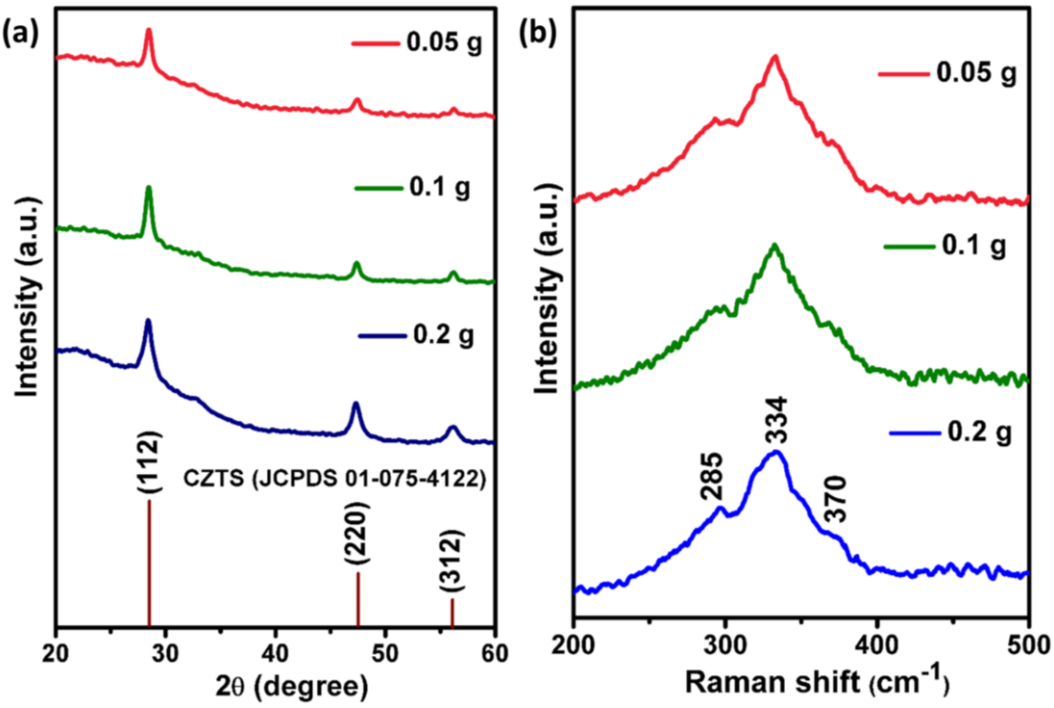

Fig.5.1. (a) XRD pattern and (b) Raman spectra of as-deposited CZTS films for different powder concentration.

This behavior could be due to the reduction in the thickness of the film. Raman analysis of CZTS film for different powder concentration was shown in 5.1(b), Raman spectra showed a prominent peak at around 334 cm^{-1} which correspond to A_1 optical phonon vibrational mode of kesterite CZTS. We could also observe two shoulder peaks at around 285 and 370 cm^{-1} which ascribed to kesterite CZTS as well [1–4].

5.2.1.2. Morphological and compositional properties

Fig. 5.2, shows the planar and cross-sectional morphology of as-deposited CZTS films for different powder concentration. Both planar and cross-sectional FE-SEM images showed the crack free and smooth surface for all the samples. From the cross-sectional images, thickness of the as-deposited film are 2.8, 1.7 and 1.3 µm for 0.2, 0.1 and 0.05 g of powder concentration respectively. Thus, revealed that the thickness of the films reduced as the powder concentration reduces. EDAX compositional analysis of as-deposited CZTS films is shown in table 5.1. The observed elemental composition from the EDAX analysis is close to the powder concentration as can be seen in chapter 4 for all the cases. Besides, the slight increment in the S content was observed which is because of the solvent (hexanethiol) used during the film preparation. It indicates that we could able to control the composition of the material which is one of the advantages of using particles based non-vacuum deposition of CZTS films. Thus, particulate deposition method could provide uniformity in composition over a large area, which is one of the limitations of vacuum techniques [5].

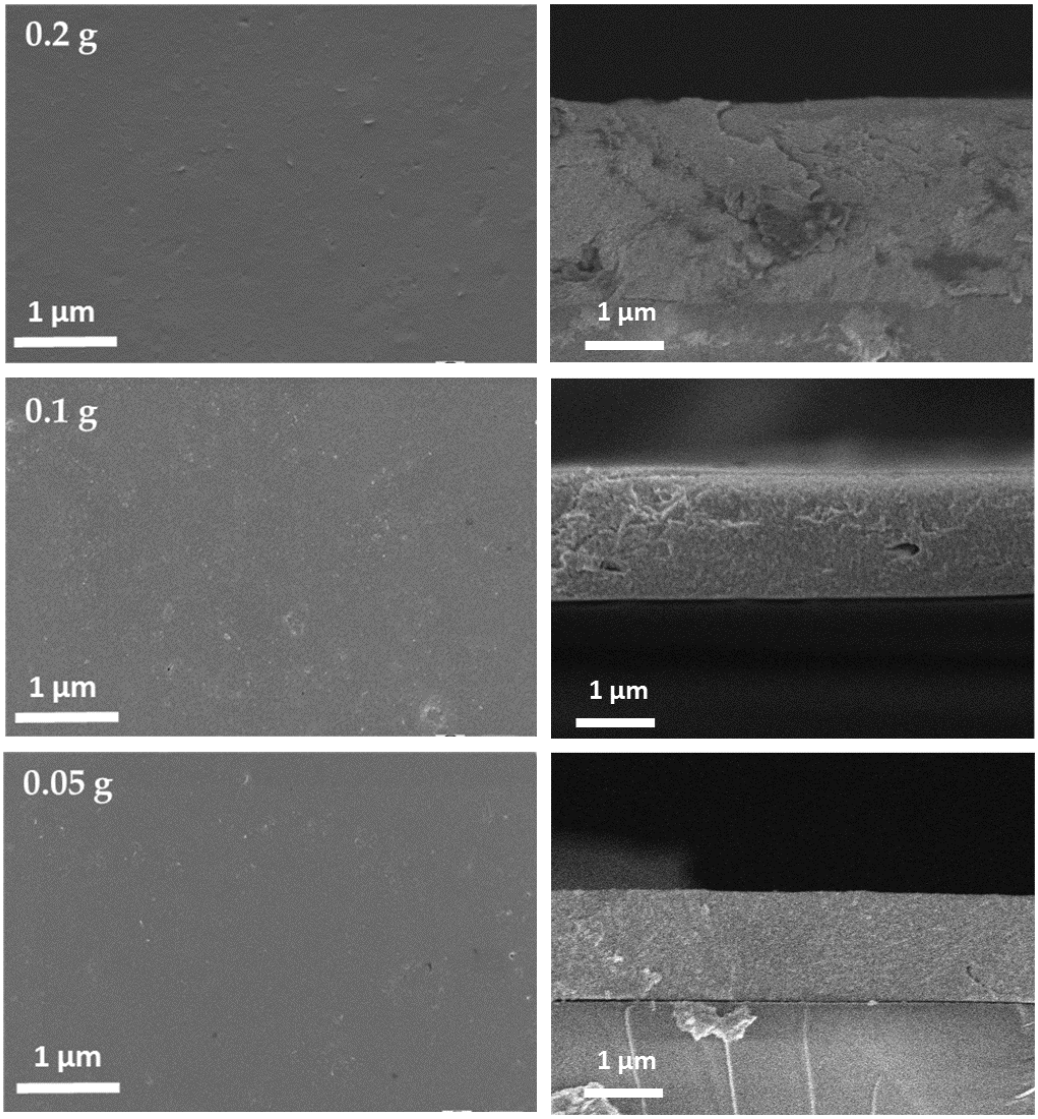

Fig.5.2. Planar and cross-sectional FE-SEM images of as-deposited CZTS films for different powder concentration.

Table.5.1. EDAX composition of as-deposited CZTS films for different powder concentration.

Powder concentration (g)	EDAX						
	Cu	Zn	Sn	S	Cu/(Zn+Sn)	Zn/Sn	C
0.2	21.81	13.67	12.22	52.30	0.84	1.12	48.10
0.1	21.19	14.29	12.35	52.17	0.80	1.15	46.16
0.05	21.70	14.16	12.30	51.84	0.82	1.15	45.50

5.2.2. Air annealing of CZTS thin films

5.2.2.1. Structural properties

The as-deposited CZTS films were annealed in an ambient atmosphere for 1 min to evaporate the carbon and the organic solvent one that used for film preparation. Annealing temperatures were varied such as 350°C and 400°C to study the effect of annealing temperature on the film properties.

XRD measurements were performed for the film annealed at 350°C of different powder concentration. It exhibited the crystalline structure similar to as-deposited CZTS films, whose diffraction peak appeared at (112), (220), (312) planes of kesterite CZTS. As can be seen in Fig. 5.3(a), the intensity of the films were decreased as the powder concentration decreases which could be due to the reduction in the thickness of the film.

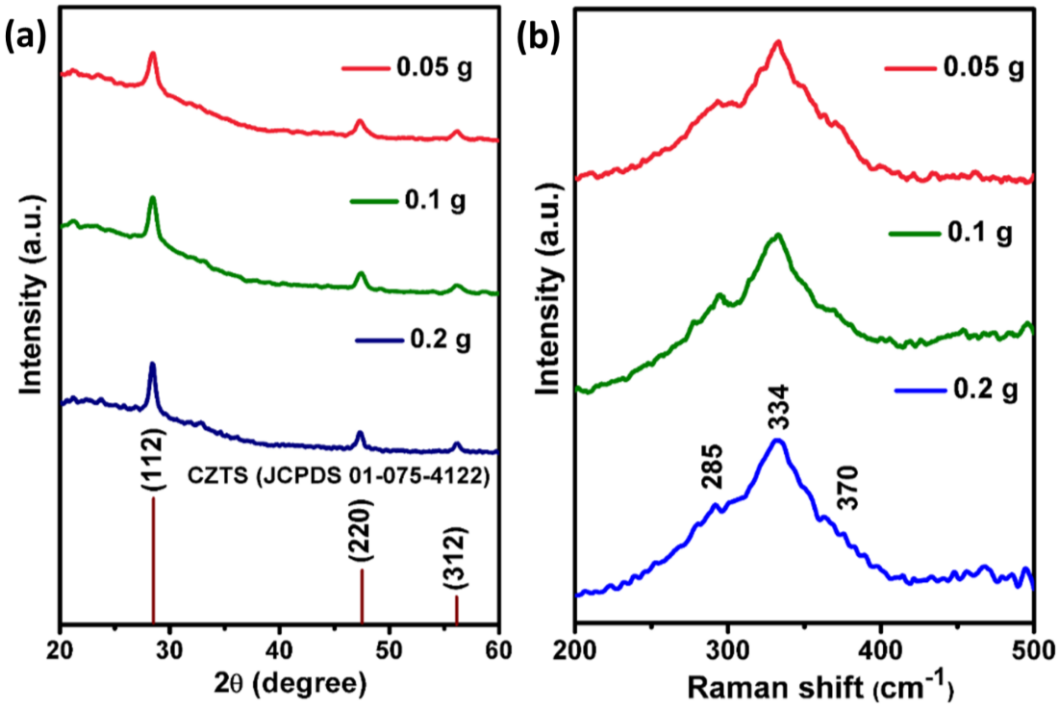

Fig.5.3. (a) XRD pattern and (b) Raman spectra of CZTS films annealed at 350°C for different powder concentration

Fig. 5.3(b), showed the Raman analysis for the film annealed at 350°C. Raman spectra showed the peak at around 334 cm^{-1} 285 and 370 cm^{-1} which has the similar peak position as observed in the as-deposited films.

5.2.2.2. Morphological and compositional properties

Planar and cross-sectional FE-SEM images of CZTS film annealed at 350°C are shown in Fig. 5.4. As can be seen in Fig, cracks were observed for the film prepared at the powder concentration of 0.2 and 0.1 g. These cracks should be avoided as it creates shunt path in the absorber thereby deteriorate solar cell performance. Formation of crack could be due to the differences in the thermal expansion (or shrinkage) between the glass substrate and the CZTS. The factors that affect the crack formation are film thickness, binder removal, temperature, solvent evaporation rate, and time. When the film allowed to anneal at certain temperatures, ligand molecules desorb and/or thermally decomposes into volatile species as can be seen in the sulfur and carbon content in table 5.2. The evaporation of solvent resulting volume shrinkage in the film. This volume reduction leads to stresses that induce cracks during annealing [6–8]. Besides, we could observe that the cracks were reduced as the film thickness reduces. This could be due to decrement in the volume shrinkage that reduces the stress as well. Finally, crack free film with the uniform thickness of 1.2 μm was obtained for 0.05 g of powder concentration. EDAX composition analysis of CZTS films for annealed at 350°C is shown in table 5.2. The film showed the similar composition as we observed in the powder. Sulfur and carbon contents were reduced as compared to the as-deposited films (table 5.1). The carbon content must be removed as it is detrimental to the solar cell performance.

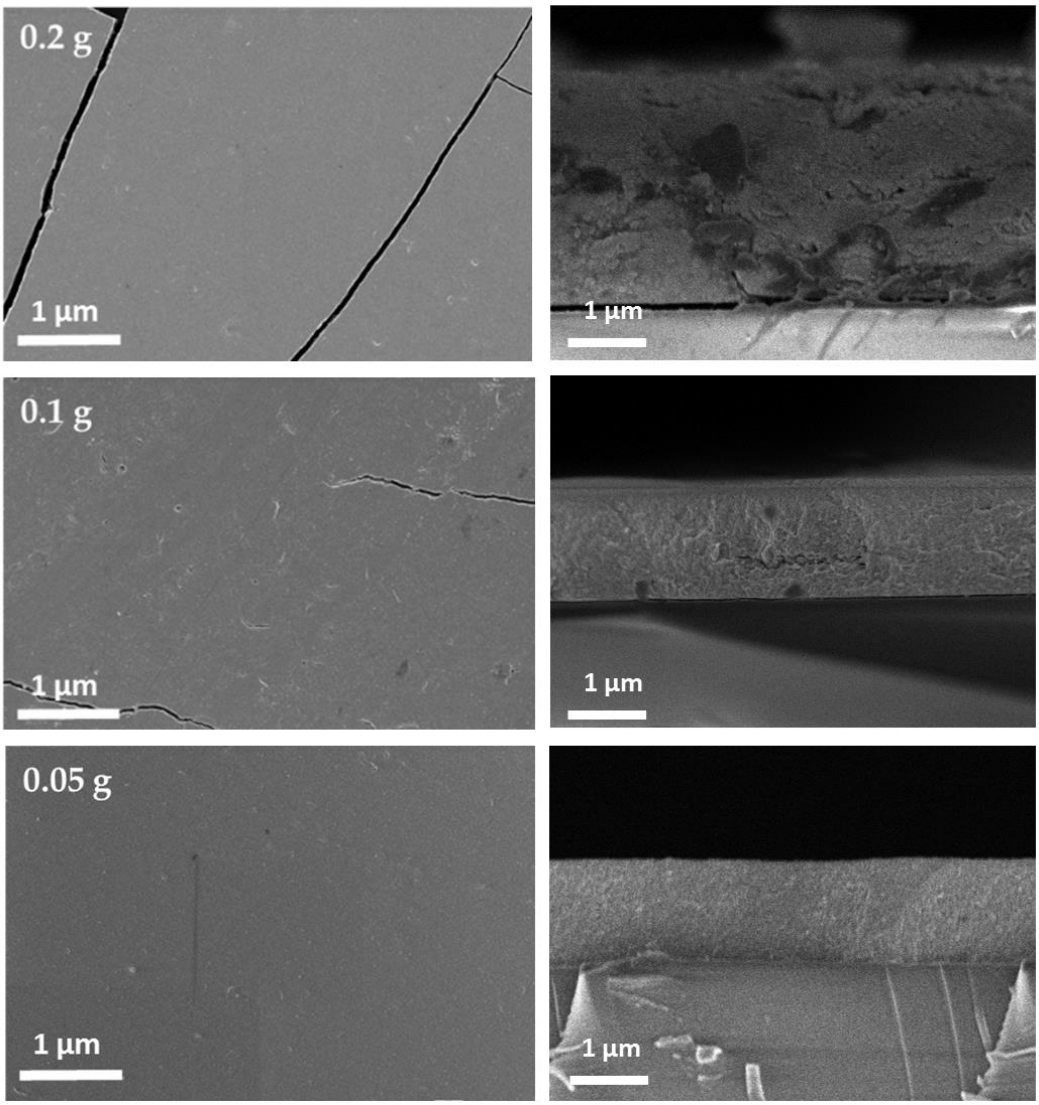

Fig.5.4. Planar and cross-sectional FE-SEM images of CZTS films annealed at 350°C for different powder concentration.

Table.5.2. EDAX composition of CZTS films annealed at 350°C for different powder concentration.

Powder concentration (g)	EDAX						
	Cu	Zn	Sn	S	Cu/Zn+Sn	Zn/Sn	C
0.2	21.98	14.22	12.25	51.56	0.83	1.16	44.76
0.1	22.06	14.37	12.23	51.33	0.82	1.17	42.06
0.05	21.96	14.68	12.43	50.93	0.81	1.18	41.76

We further annealed the film at 400°C to study their influences on the morphological properties. As can be seen in Fig. 5.5, cracks were increased for the film annealed at 400°C as compared to 350°C. This could be due to an increment in the thermal stress with increasing the annealing temperature. From the EDAX analysis, the similar composition was observed as shown in table 5.3. Also, the sulfur and carbon contents were further decreased.

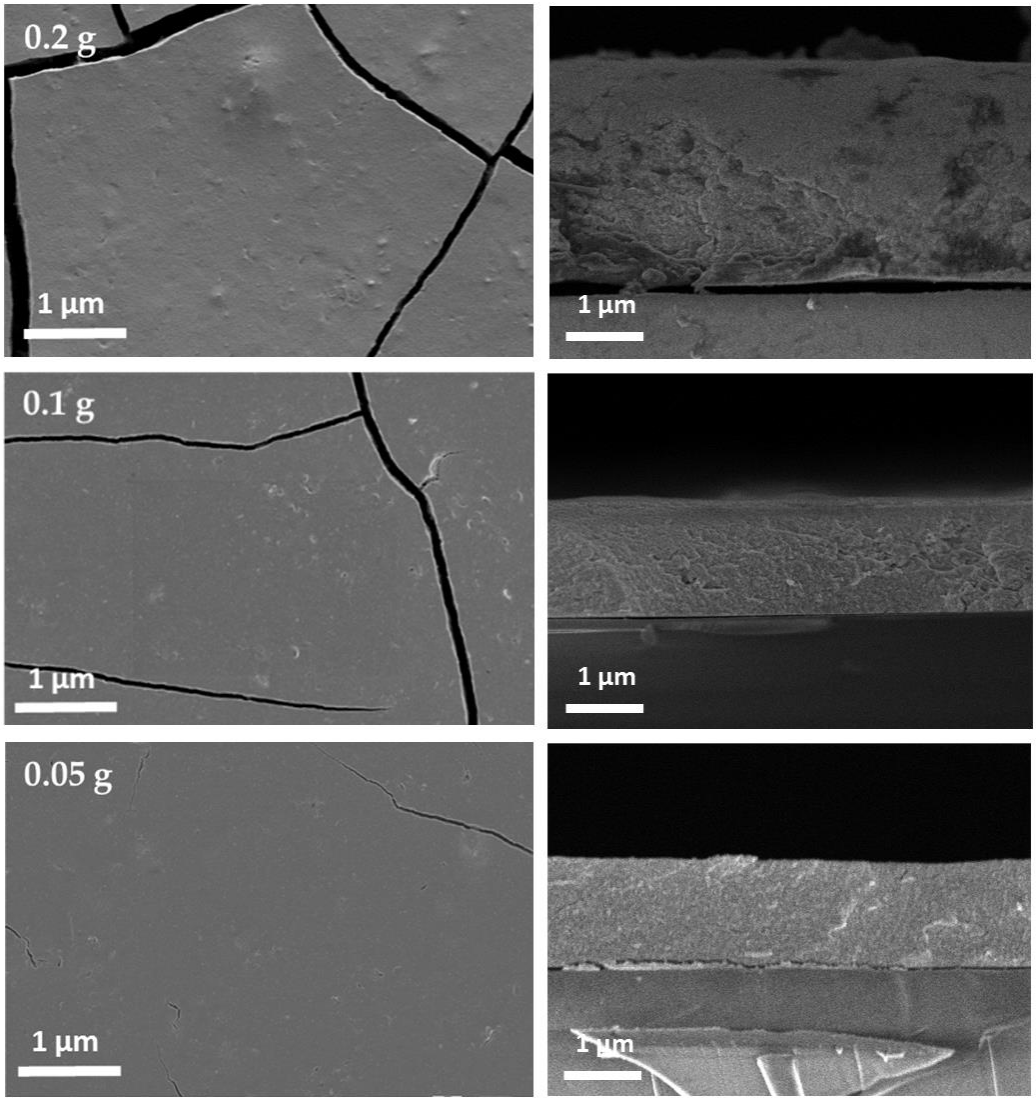

Fig.5.5. Planar and cross-sectional FE-SEM images of CZTS films annealed at 400°C for different powder concentration.

Table.5.3. EDAX composition of CZTS films annealed at 400°C for different powder concentration.

Powder concentration (g)	EDAX						
	Cu	Zn	Sn	S	Cu/(Zn+Sn)	Zn/Sn	C
0.2	22.19	14.72	12.39	50.70	0.82	1.18	41.96
0.1	22.32	14.82	12.42	50.44	0.81	1.19	39.96
0.05	22.18	14.79	12.85	50.18	0.80	1.16	38.56

5.2.3. Selenization of CZTS thin films

5.2.3.1. Structural properties

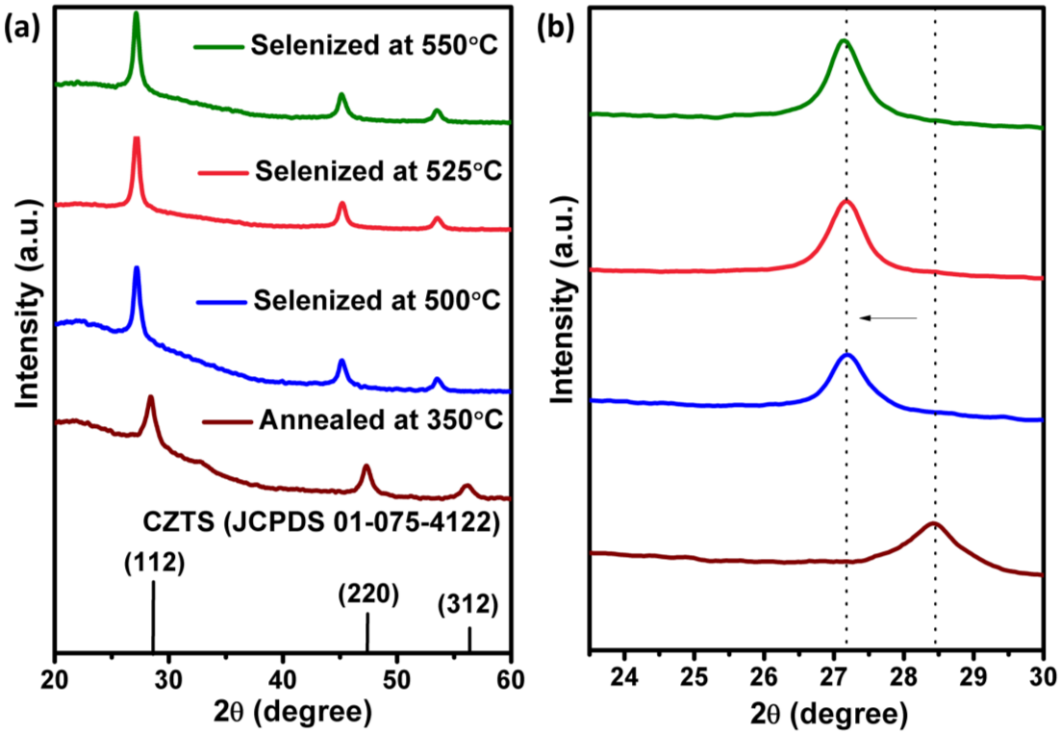

Fig.5.6. (a) XRD pattern and (b) enlarged view of (112) plane of annealed and selenized films for different temperature.

Films annealed at 350°C with powder concentration of 0.05 g were annealed under selenium atmosphere (selenization). The experimental conditions are same as discussed in section 3.1.4.2. Fig. 5.6(a) showed the XRD patterns of annealed and selenized CZTS films. Annealed film showed the

diffraction peaks at 2θ values of 28.45, 47.60 and 56.10°, correspond to (112), (220) and (312) planes of kesterite CZTS which is similar to the powder. After selenization, the peaks were shifted to lower 2θ values for all the cases. The same behavior was observed by other researchers [9,10]. In order to see the peak shift clearly, enlargement of the (112) plane is shown in Fig. 5.6(b), indicating peak shifts from 28.45 to 27.22^0. The peak shift is due to the replacement of the majority of smaller sized sulfur atoms (0.184 nm) by larger sized selenium (0.198 nm) atoms during the selenization process, resulting in larger lattice parameters for CZTSSe than for CZTS as shown in Fig. 5.7(c). The calculated lattice parameters are in good accordance with the literature [11]. The lattice parameters ***a*** and ***c*** were calculated from the XRD data using the following formula:

$$\frac{1}{d^2} = \frac{h^2+k^2}{a^2} + \frac{l^2}{c^2} \qquad (1)$$

where h, k and l are miller indices, *a* and *c* are lattice constants and d is the inter-planar distance.

The inter-planar distance was calculated using Bragg's diffraction equation:

$$d = \frac{n\lambda}{2\sin\theta} \qquad (2)$$

where n is a positive integer, λ is wavelength (1.5405 Å) and θ is Bragg's angle.

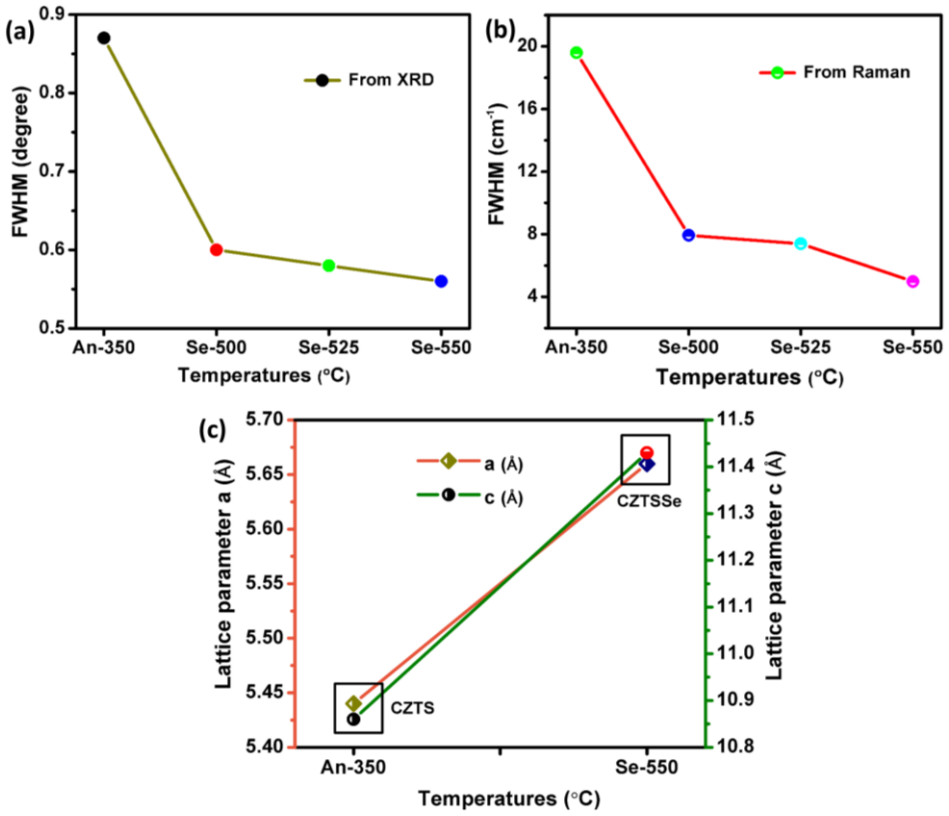

Fig.5.7. (a) FWHM from XRD, (b) FWHM from Raman and (c) lattice parameters for annealed and selenized temperatures.

In order to further confirm the phase purity, Raman measurements were carried out for CZTSSe films. As can be seen in Fig. 5.8, Raman peaks were observed at 334, 285 and 370 cm^{-1} for annealed films, agreeing well with the powder samples as can be seen in chapter 4 (Fig. 4.11(b)). The selenized film showed the A_1 mode shift of CZTSe at 171, 192 and 238 cm^{-1} for all the samples [12–14]. From the Raman spectra, secondary phases like Cu_2S, ZnS, ZnSe, CTS etc., were not observed. Thus, the results confirmed that the formation of pure CZTSSe phase. As can be seen in Fig. 5.7(a) and (b), FWHM from XRD and Raman spectra, were decreased for the CZTSSe films which indicates the improvement in the crystallinity.

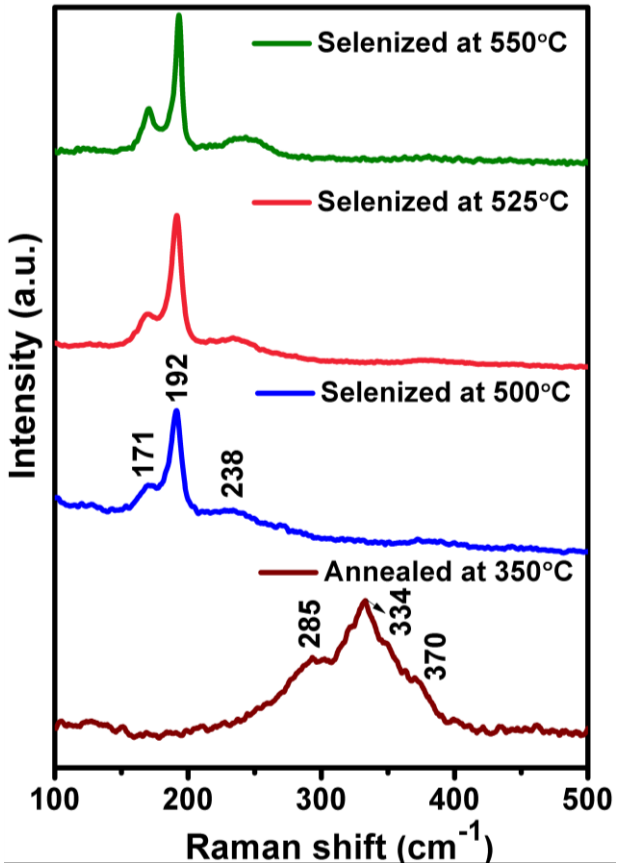

Fig.5.8. Raman spectra of annealed and selenized films for different temperature.

5.2.3.2. Morphological and compositional properties

FE-SEM images of CZTS films selenized at different temperatures are shown in Fig. 5.9. Film selenized at 500°C showed a few voids on the surface, which could be due to insufficient Se incorporation as can be observed from the EDAX analysis (Fig. 5.10(a)). When the selenization temperature increased to 525°C, voids were reduced. Further increasing the selenization temperature to 550°C, voids free and compact morphology of CZTSSe was observed, which is due to more Se incorporation into the films. Besides, film selenized at 550°C showed crack-free, smooth surface and slight increment in the grain size as compared to annealed film (Fig. 5.4).

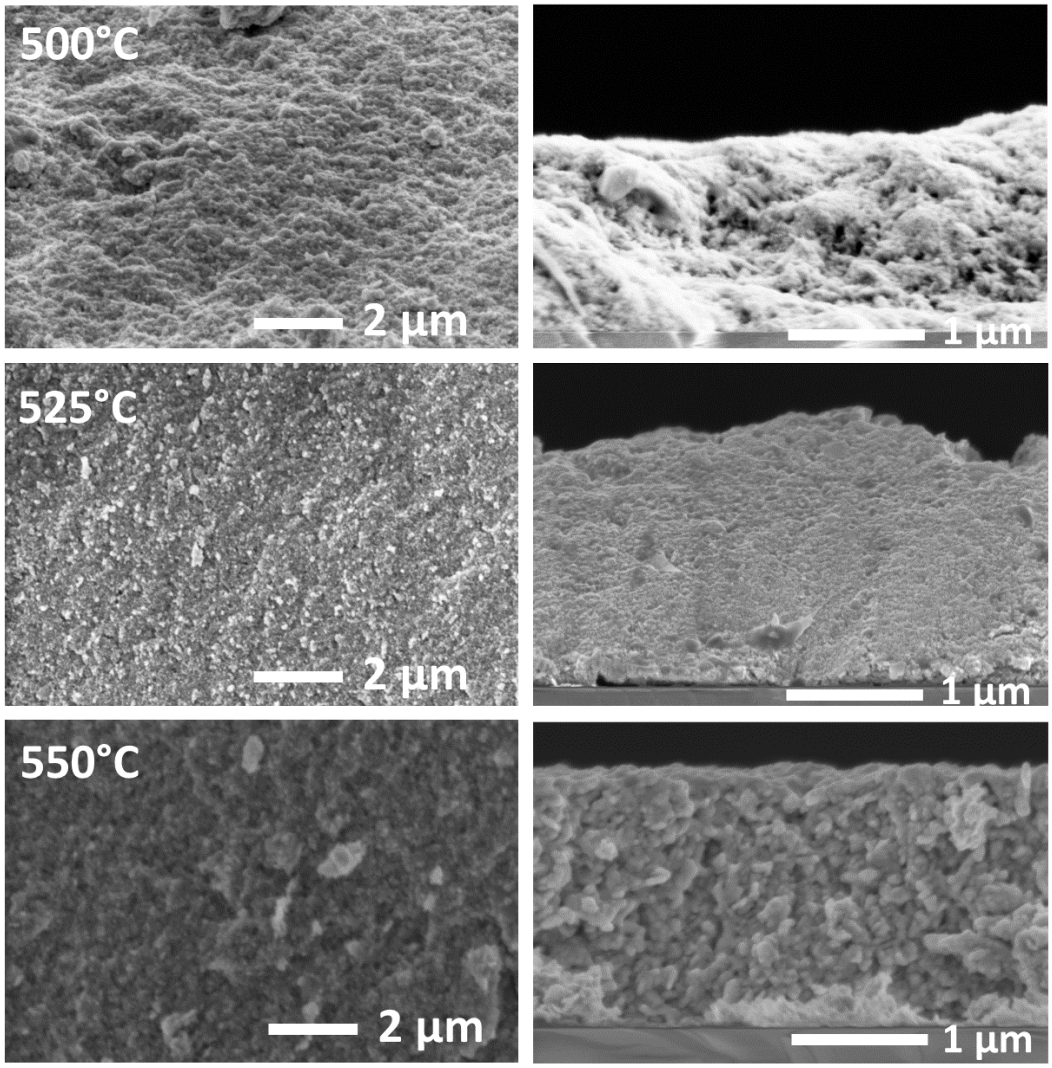

Fig.5.9. Planar and cross-sectional FE-SEM images of CZTSSe films for different selenization temperature.

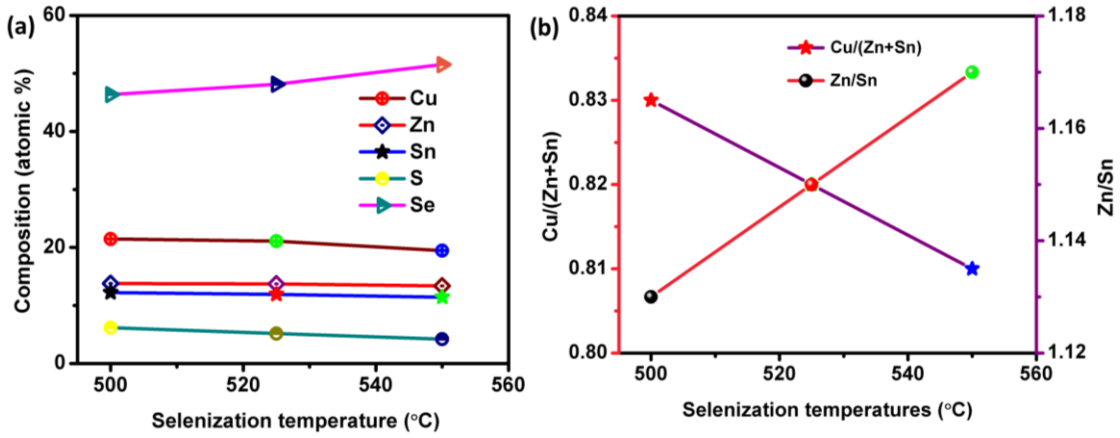

Fig.5.10. (a) The elemental composition and (b) the corresponding ratio of Cu/(Zn + Sn) and Zn/Sn of the CZTSSe films for different selenization temperature.

Thus, the morphology of the CZTSSe films evolves from voids to compact. It is interesting to note that the thickness of CZTSSe films increased to 1.9 µm as compared to annealed film (1.2 µm). This could be due to volume expansion in the unit cell when the selenium incorporated into the lattice as mentioned in the XRD analysis. Moreover, the obtained CZTSSe film thickness (1.9 µm) is suitable for solar cell applications.

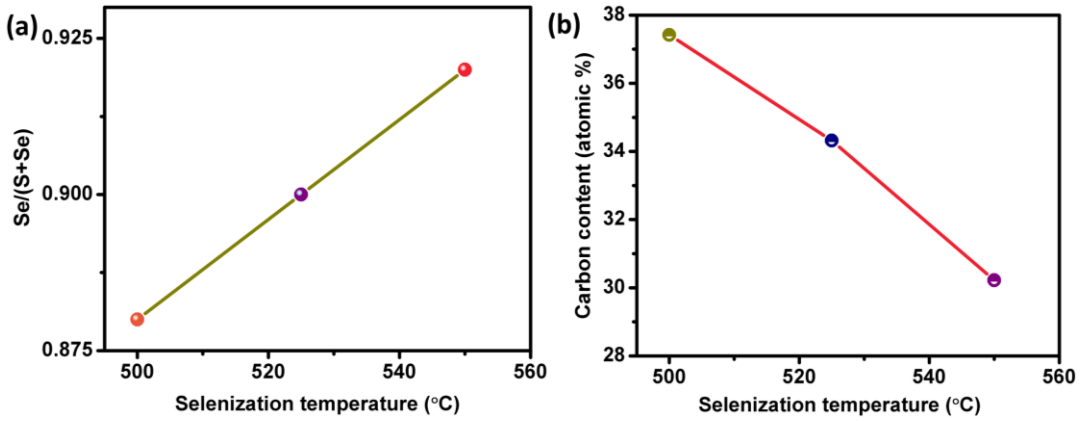

Fig.5.11. (a) The Se/(S+Se) ratio and (b) carbon content of the CZTSSe films for different selenization temperature.

EDAX compositional analysis was performed for the samples selenized at different temperature. Fig. 5.10, showed the elemental compositions and compositional ratios of Cu/(Zn+Sn) and Zn/Sn. The elemental composition varied with increasing the selenization temperature as shown in Fig. 5.10(a). The Cu/(Zn+Sn) ratio decreases while the Zn/Sn ratio increases as a function of selenization temperature (Fig. 5.10(b)). With increases in the selenization temperature, Se/(S+Se) ratio increases as the amount of S decreases, can be observed from the Fig. 5.11(a). Furthermore, the carbon content reduced from 41 at% (annealed) to 30 at% after selenization as shown in Fig. 5.11(b). The selenized films shows Cu-poor, Zn-rich composition, which is one of the prime conditions for highly efficient thin-film solar cells [15].

5.2.3.3. Optical properties

UV-Vis-NIR absorbance spectra measurements were performed for the film annealed and selenized at different temperature. The absorbance spectra and corresponding band gap for all the samples are shown in Fig. 5.12. The optical band gap was calculated using Tuac's relation as described in the equation (4.1). The estimated band gap energy for an annealed film without using a Se atmosphere is 1.52 eV, which is in good accordance with the powder as discussed in chapter 4. The band gap energy systematically decreases from 1.52 to 1.09 eV for CZTSSe films that were annealed in a Se atmosphere with an increasing selenization temperature (Fig. 5.12(b)). The observed band gap values were matches well with the reported values [16–19]. The replacement of the S atoms by Se atoms, resulting narrow band gap energy of the CZTSSe films. The band gap energy of the CZTSSe films is systematically tuned by varying the selenization temperature. The efficiency of CZTSSe can be enhanced by narrowing the band gap energy of CZTS thin films [20].

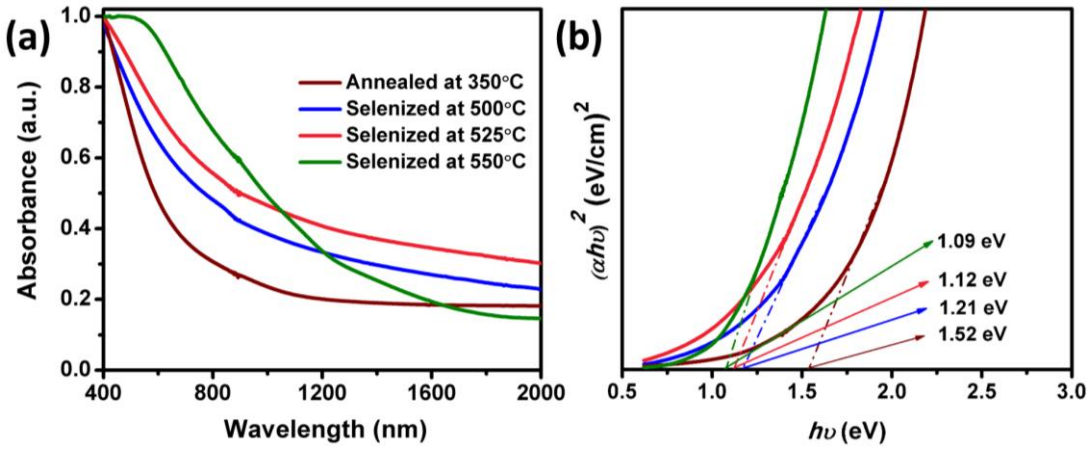

Fig.5.12. (a) UV-Vis-NIR absorption spectra and (b) corresponding band gap of annealed and selenized films for different temperature.

5.2.3.3. Electrical properties

The conductivity type, carrier concentration, mobility and resistivity of CZTS and CZTSSe films were measured by Hall-effect. The reported value of mobility and carrier concentration for CZTS absorber material are in the range of 1 to 10 $cm^2 \cdot V^{-1} \cdot s^{-1}$ and 10^{16} to 10^{18} cm^{-3} [21–23]. As can be seen in table 5.4, all the films showed P-type conductivity. Compared to CZTS film, the hole concentration and mobility were increased while resistivity decreased for the CZTSSe films. From the cross-sectional FE-SEM images (Fig. 5.4), it can be seen that CZTS film consists of smaller grains which contributes high density of grain boundaries that act as a barrier to the flow of charge carriers. This leads to higher resistivity and lower mobility of charge carriers. Selenization process helps to attain enhanced crystallization which results in improved carrier concentration and lowers the resistivity. As the selenization temperature increases, mobility increased while resistivity decreased. The increase in carrier concentration for CZTSSe films can be due to the slight increment in the grain size as observed from the FE-SEM images (Fig. 5.9). The increment in the mobility could be due to improvement in the crystallite and grain size as observed from XRD, Raman, and FE-SEM analyses. Increase in crystallite size reduces the grain boundary density

and thus the grain boundary barrier [24]. Hence, the mobility of charge carrier increases. Thus, the observed mobility and carrier concentration were consistent with the literature values as discussed above. Therefore, the film selenized at 550°C showed higher mobility and less resistivity compared to other films which suggest that the obtained CZTSSe film is suitable for solar cell applications.

Table.5.4. Carrier type, carrier concentration, mobility, and resistivity of annealed and selenized films for different temperature.

Experimental conditions	Type of conductivity	Carrier concentration (cm^{-3})	Mobility (cm^2/Vs)	Resistivity (Ωcm)
Annealed at 350°C	P	1.13×10^{16}	0.05	147
Selenized at 500°C	P	2.17×10^{17}	0.8	131
Selenized at 525°C	P	4.32×10^{17}	1.9	98
Selenized at 550°C	P	7.52×10^{17}	3	70

5.2.3.4. Current-voltage characteristics

The photo-response behavior of CZTS and CZTSSe films were studied in order to examine their potential applications in the field of solar cells.

I-V characteristic of films was measured under dark as well as under illumination as described in section 3.2.9. To perform the I-V characteristics, Au contacts in the circular shape of 0.1 cm diameter is deposited on a film. I-V measurements were carried out between two contacts separated by 0.2 cm. The thickness of the CZTS and CZTSSe films were 1.2, 1.4, 1.8 and 1.9 μm respectively. A voltage of 10 V is applied across the two Au contacts as shown in Fig. 5.13. The resulting current flowing across the film between two contacts were measured. Subsequently, the experiment was repeated under a light source of 300 W.

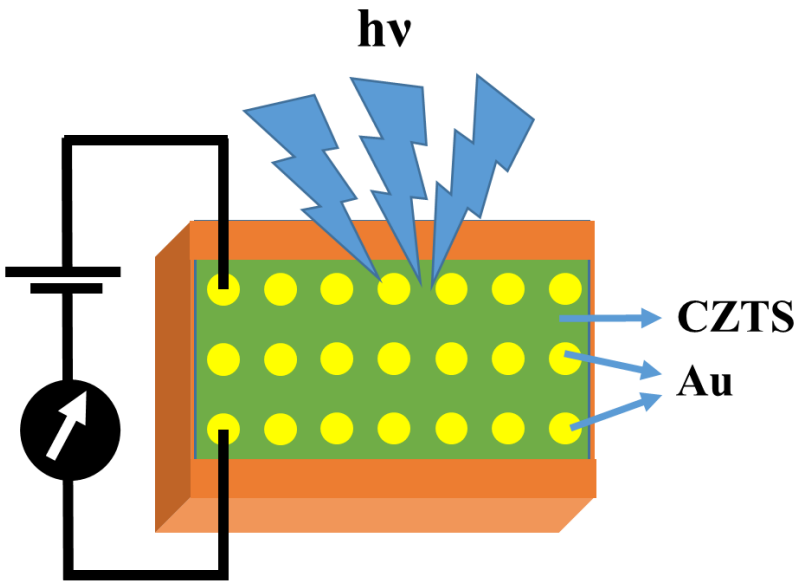

Fig.5.13. Schematic representation of I-V measurements.

Fig. 5.14, shows I–V measurements of the CZTS and CZTSSe films under dark and illumination of light. Films exhibited linear I-V curves, due to ohmic nature of the metal contacts as reported by other researchers [25,26]. Photoconductivity of the films increased under the illumination of light as compared to dark conditions. This is because, the lumination excites electrons from valence band to the conduction band. The excitation of electrons increases the holes in the CZTS and CZTSSe films and thus enhances the conductivity. The photoconductivity of films can be expressed by ΔI (current difference in the dark and under illumination of light at a given bias voltage). The photocurrent ΔI is calculated by I_{photon}/I_{dark} in CZTS and CZTSSe thin films were 1.07, 1.35, 1.48 and 1.74 μA respectively. The film selenized at 550°C showed higher photoconductivity than other films which is due to an increment in the grain size that reduces the defects and enhances the properties of the film. Hence, the obtained CZTSSe film, indicating their potential application in the field of solar cells.

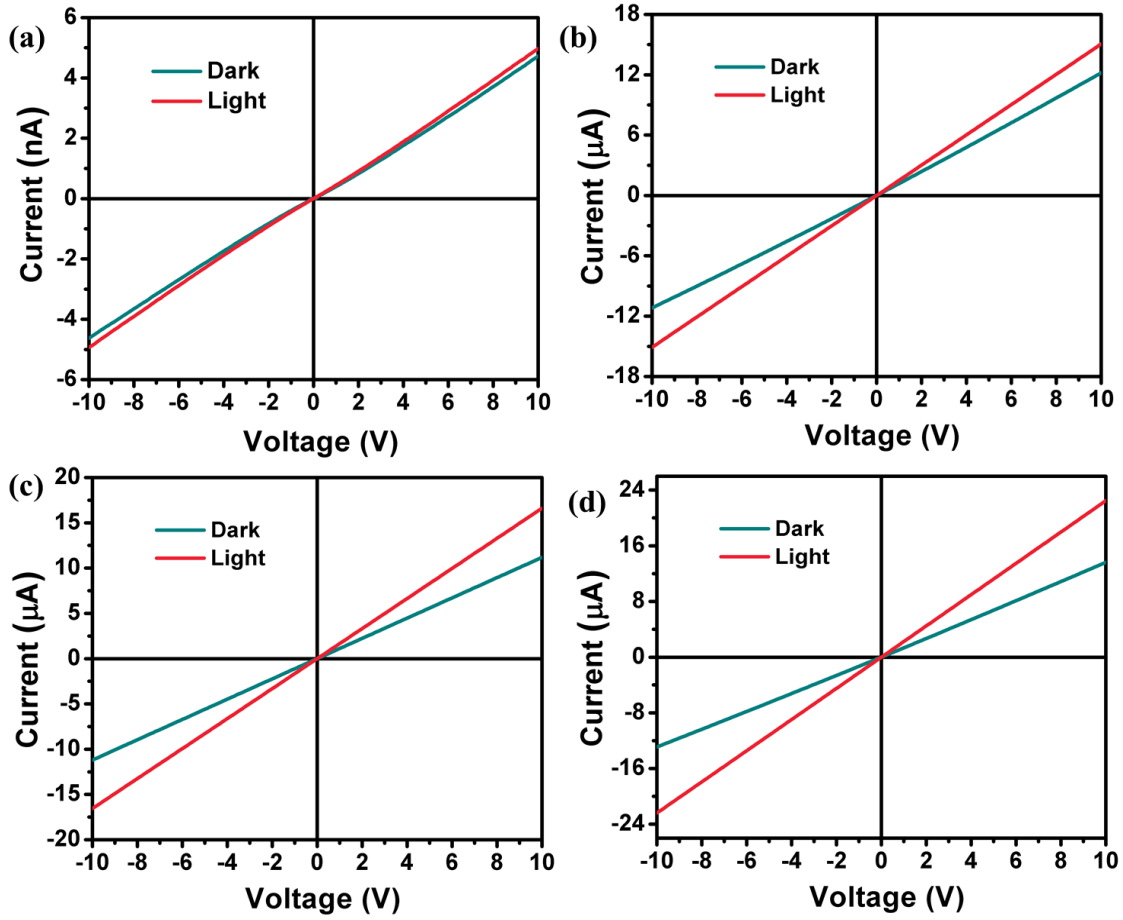

Fig.5.14. Dark and light I-V characteristics of annealed and selenized films for different temperature.

5.3. Summary

- Heating-up synthesized Nps was used for film preparation. For this purpose, CZTS ink was formulated using hexanethiol as a solvent. Then, the ink was coated as a thin film using doctor-blade method. CZTS powder concentration was varied such as 0.2, 0.1 and 0.05 g to achieve the crack-free films.
- Properties of as-deposited CZTS films for different powder concentration were studied using XRD, Raman, FE-SEM and EDAX analyses. Structural analysis exhibited similar properties of powder which revealed that the CZTS powder has successfully transformed into the film. FE-SEM images showed crack-free and smooth surface of film. The observed elemental composition

from the EDAX analysis is close to the powder concentration. Besides, the slight increment in the sulfur content was observed which is because of the solvent used during the film preparation.

- CZTS films prepared at different powder concentration were annealed at 350°C and 400°C to evaporate the solvent and carbon. Structural, morphological and compositional properties were investigated for the annealed films. From the FE-SEM images, cracks were observed for the annealed films with the powder concentration of 0.2 and 0.1 g. Formation of cracks could be due to thermal stress (shrinkage) created in the film. As the annealing temperature increases, cracks increased which is due to increment in the thermal stress. Besides, we could observe that the cracks were reduced as the film thickness reduced from 2.7 to 1.2 μm. This could be due to decrement in the volume shrinkage that reduces the stress. Finally, crack free and uniform thickness of 1.2 μm film was obtained for 0.05 g of powder concentration. As the annealing temperature increases, the amount of sulfur and carbon were reduced.
- CZTS films annealed at 350°C with powder concentration of 0.05 g were selenized at different temperatures such as 500, 525 and 550°C. Structural analysis showed a peak shift towards lower wavelength for the CZTSSe films which is due to the replacement of the majority of smaller sized sulfur atoms (0.184 nm) by larger sized selenium (0.198 nm) atoms during the selenization process. Thus, enlarges the unit cell as we observed increment in the lattice parameters for CZTSSe than CZTS. After selenization, narrow and sharp peaks were observed, indicating improvement in the crystallinity.
- With increases in the selenization temperature, voids were decreased. Film selenized at 550°C showed void-free, smooth surface with slight increment in the grain size. Compositional analysis revealed Cu-poor, Zn-rich composition which is optimal for solar cell applications. With increase in the selenization

temperature, selenium content increased while sulfur content decreased. Besides, carbon content decreased as a function of selenization temperature.

- Hall effect studies revealed the improvement in the mobility and carrier concentration for the CZTSSe films as compared to annealed film. This could be due to improvement in the crystallite size as observed from the XRD, Raman and FE-SEM images. Also, film selenized at 550°C showed higher photoconductivity than other films, which indicates their suitability in the filed of low-cost thin film solar cells.

References

[1] R. Saravana Kumar, B.D. Ryu, S. Chandramohan, J.K. Seol, S.K. Lee, C.H. Hong, Rapid synthesis of sphere-like Cu_2ZnSnS_4 microparticles by microwave irradiation, Materials Letters. 86 (2012) 174–177. doi:10.1016/j.matlet.2012.07.059.

[2] V.T. Tiong, J. Bell, H. Wang, One-step synthesis of high quality kesterite Cu_2ZnSnS_4 nanocrystals - A hydrothermal approach, Beilstein Journal of Nanotechnology. 5 (2014) 438–446. doi:10.3762/bjnano.5.51.

[3] K. Mokurala, P. Bhargava, S. Mallick, Single step synthesis of chalcogenide nanoparticles Cu_2ZnSnS_4, Cu_2FeSnS_4 by thermal decomposition of metal precursors, Materials Chemistry and Physics. 147 (2014) 371–374. doi:10.1016/j.matchemphys.2014.06.049.

[4] A. Khare, B. Himmetoglu, M. Johnson, D.J. Norris, M. Cococcioni, E.S. Aydil, Calculation of the lattice dynamics and Raman spectra of copper zinc tin chalcogenides and comparison to experiments, Journal of Applied Physics. 111 (2012). doi:10.1063/1.4704191.

[5] J. Han, S.W. Shin, M.G. Gang, J.H. Kim, J.Y. Lee, Crystallization behaviour of co-sputtered Cu_2ZnSnS_4 precursor prepared by sequential sulfurization processes., Nanotechnology. 24 (2013) 95706. doi:10.1088/0957-4484/24/9/095706.

[6] C. Liewhiran, S. Phanichphant, Improvement of flame-made ZnO nanoparticulate thick film morphology for ethanol sensing, Sensors. 7 (2007) 650–675. doi:Doi 10.3390/S7050650.

[7] G.C.A.M. Janssen, Stress and strain in polycrystalline thin films, Thin Solid Films. 515 (2007) 6654–6664. doi:10.1016/j.tsf.2007.03.007.

[8] P. Xu, A.S. Mujumdar, B. Yu, Drying-Induced Cracks in Thin Film Fabricated from Colloidal Dispersions, Drying Technology. 27 (2009) 636–652. doi:10.1080/07373930902820804.

[9] K. V. Gurav, S.W. Shin, U.M. Patil, M.P. Suryawanshi, S.M. Pawar, M.G. Gang, S.A. Vanalakar, J.H. Yun, J.H. Kim, Improvement in the properties of CZTSSe thin films by selenizing single-step electrodeposited CZTS thin films, Journal of Alloys and Compounds. 631 (2015) 178–182. doi:10.1016/j.jallcom.2014.12.253.

[10] Z. Li, J.C.W. Ho, K.K. Lee, X. Zeng, T. Zhang, L.H. Wong, Y.M. Lam, Environmentally friendly solution route to kesterite $Cu_2ZnSn(S,Se)_4$ thin films for solar cell applications, RSC Advances. 4 (2014) 26888. doi:10.1039/c4ra03349c.

[11] H. Reshak, K. Nouneh, I. V Kityk, J. Bila, S. Auluck, H. Kamarudin, Z. Sekkat, Structural , Electronic and Optical Properties in Earth- Abundant Photovoltaic Absorber of Cu_2ZnSnS_4 and $Cu_2ZnSnSe_4$ from DFT calculations, International Journal of Electrochemical Science. 9 (2014) 955–974.

[12] X. Zeng, K.F. Tai, T. Zhang, C.W.J. Ho, X. Chen, A. Huan, T.C. Sum, L.H. Wong, $Cu_2ZnSn(S,Se)_4$ kesterite solar cell with 5.1% efficiency using spray pyrolysis of aqueous precursor solution followed by selenization, Solar Energy Materials and Solar Cells. 124 (2014) 55–60. doi:10.1016/j.solmat.2014.01.029.

[13] D.B. Khadka, S.Y. Kim, J.H. Kim, Effects of Ge Alloying on Device Characteristics of Kesterite-Based CZTSSe Thin Film Solar Cells, Journal of Physical Chemistry C. 120 (2016) 4251–4258. doi:10.1021/acs.jpcc.5b11594.

[14] J. Guo, Y. Pei, Z. Zhou, W. Zhou, D. Kou, S. Wu, Solution-Processed $Cu_2ZnSn(S,Se)_4$ Thin-Film Solar Cells Using Elemental Cu, Zn, Sn, S, and Se Powders as Source., Nanoscale Research Letters. 10 (2015) 1045. doi:10.1186/s11671-015-1045-6.

[15] W. Wang, M.T. Winkler, O. Gunawan, T. Gokmen, T.K. Todorov, Y. Zhu, D.B. Mitzi, Device characteristics of CZTSSe thin-film solar cells with 12.6%

efficiency, Advanced Energy Materials. 4 (2014) 1–5. doi:10.1002/aenm.201301465.

[16] Q. Guo, H.W. Hillhouse, R. Agrawal, Synthesis of Cu_2ZnSnS_4 nanocrystal ink and its use for solar cells, Journal of the American Chemical Society. 131 (2009) 11672–11673. doi:10.1021/ja904981r.

[17] X. Wang, Z. Sun, C. Shao, D.M. Boye, J. Zhao, A facile and general approach to polynary semiconductor nanocrystals via a modified two-phase method., Nanotechnology. 22 (2011) 245605. doi:10.1088/0957-4484/22/24/245605.

[18] F. Liu, F. Zeng, N. Song, L. Jiang, Z. Han, Z. Su, C. Yan, X. Wen, X. Hao, Y. Liu, Kesterite $Cu_2ZnSn(S,Se)_4$ Solar Cells with beyond 8% Efficiency by a Sol-Gel and Selenization Process, ACS Applied Materials and Interfaces. 7 (2015) 14376–14383. doi:10.1021/acsami.5b01151.

[19] Y. Sun, Y. Zhang, H. Wang, M. Xie, K. Zong, H. Zheng, Y. Shu, J. Liu, H. Yan, M. Zhu, W. Lau, Novel non-hydrazine solution processing of earth-abundant $Cu_2ZnSn(S,Se)_4$ absorbers for thin-film solar cells, Journal of Materials Chemistry A. 1 (2013) 6880–6887. doi:10.1039/c3ta10566k.

[20] K.R. Choudhury, Y. Cao, J. V. Caspar, Q. Guo, L.K. Johnson, I. Malajovich, D. Radu, H. David Rosenfeld, L. Silverman, W. Wu, Effect of the selenization process on structural and device properties of nanoparticle-derived CZTSSe thin films, Conference Record of the IEEE Photovoltaic Specialists Conference. (2013) 43–46. doi:10.1109/PVSC.2013.6744095.

[21] V.G. Rajeshmon, C.S. Kartha, K.P. Vijayakumar, C. Sanjeeviraja, T. Abe, Y. Kashiwaba, Role of precursor solution in controlling the opto-electronic properties of spray pyrolysed Cu_2ZnSnS_4 thin films, Solar Energy. 85 (2011) 249–255. doi:10.1016/j.solener.2010.12.005.

[22] N. Muhunthan, O.P. Singh, V.N. Singh, Growth of CZTS by co-sputtering and sulfurization for solar cell applications, SPIE Micro+Nano Materials, Devices, and Applications. 8923 (2013) 89232H. doi:10.1117/12.2032433.

[23] T. Tanaka, T. Nagatomo, D. Kawasaki, M. Nishio, Q. Guo, A. Wakahara, A. Yoshida, H. Ogawa, Preparation of Cu_2ZnSnS_4 thin films by hybrid sputtering, Journal of Physics and Chemistry of Solids. 66 (2005) 1978–1981. doi:10.1016/j.jpcs.2005.09.037.

[24] K.-C. Wang, P. Chen, C.-M. Tseng, Facile one-pot synthesis of Cu_2ZnSnS_4 quaternary nanoparticles using a microwave-assisted method, CrystEngComm. 15 (2013) 9863. doi:10.1039/c3ce41691g.

[25] S. Sarkar, K. Bhattacharjee, G.C. Das, K.K. Chattopadhyay, Self-sacrificial template directed hydrothermal route to kesterite-Cu_2ZnSnS_4 microspheres and study of their photo response properties, CrystEngComm. 16 (2014) 2634. doi:10.1039/c3ce42229a.

[26] B. Ananthoju, A. Kushwaha, F.J. Sonia, M. Aslam, Structural and optical properties of electrochemically grown highly crystalline Cu_2ZnSnS_4 (CZTS) thin films, AIP Conference Proceedings. 1512 (2013) 706–707. doi:10.1063/1.4791233.

Chapter 6
Hot-injection synthesis of CZTS nanoparticles and deposition of thin films

In this chapter, we synthesize kesterite CZTS nanoparticles (Nps) by hot-injection process. Herein, we discuss about the off-stoichiometric [$Cu_{1.79}Zn_{1.16}Sn_{0.95}S_{4.08}$ (Cu-poor Zn-rich)] composition of CZTS Nps. Furthermore, the influence of reaction temperature and time on the structural, morphological, compositional and optical properties are examined. Besides, based on the detailed time dependent evolution, possible growth mechanism is proposed for the CZTS Nps. Afterwards, the optimized CZTS Nps (220°C for 2 h) are used to deposit films by doctor blade method. Subsequently, annealing and selenization process are carried out for the films.

6.1. Synthesis of CZTS Nps

6.1.1 Influence of reaction temperature

6.1.1.1 Structural properties

Fig. 6.1(a) shows the XRD patterns of CZTS Nps synthesized at different reaction temperature. From the XRD pattern, (112), (020), (220) and (312) planes were observed for all the samples, correspond to kesterite crystal structure of CZTS (JCPDS 01-075-4122). Besides, sample synthesized at 180˚C showed Cu_2S phase which is due to incomplete reaction at this temperature. As can be seen in Fig.6.2, full-width half maximum (FWHM) decreased from 0.55 to 0.32° which indicates the improvement in the crystallite size. The crystallite size was calculated using the Scherrer formula as described in the chapter 4 (equation 4.1). The calculated crystallite size was found to increase from 14.74 to 27.92 nm with

increases in the reaction temperature. These results are in good agreement with FE-SEM images.

To further confirm the phase purity of the CZTS Nps, Raman measurements were taken as shown in Fig. 6.1(b). Raman spectra exhibited a prominent peak at around 333 cm^{-1} and two shoulder peaks at 284 and 372 cm^{-1}, related to kesterite crystal structure of CZTS [1]. Besides, the samples synthesized at 180 and 200°C showed peaks at 477 and 296 cm^{-1}, attributed to Cu_2S and (Cu_2SnS_3) CTS phases, respectively [2–5]. As the reaction temperature increased to 220°C, secondary phases disappeared completely and pure phase of CZTS was obtained. A significant difference was not observed, further increasing the reaction temperature to 240°C. Therefore, the structural analysis indicated the secondary and ternary phases at less reaction temperatures (180-200°C) and the pure phase of CZTS was attained at 220°C.

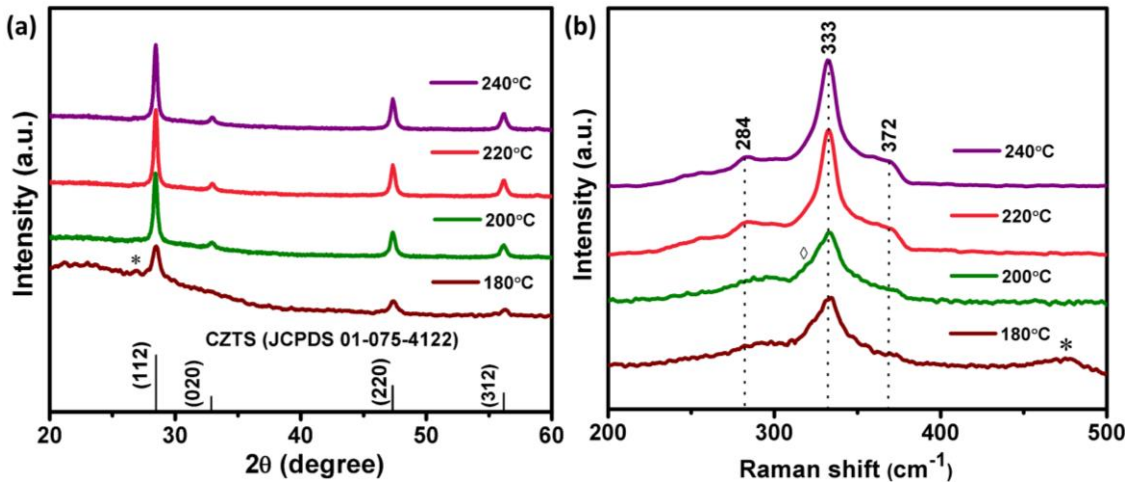

Fig. 6.1. (a) XRD pattern and (b) Raman spectra of CZTS Nps synthesized at different reaction temperature.

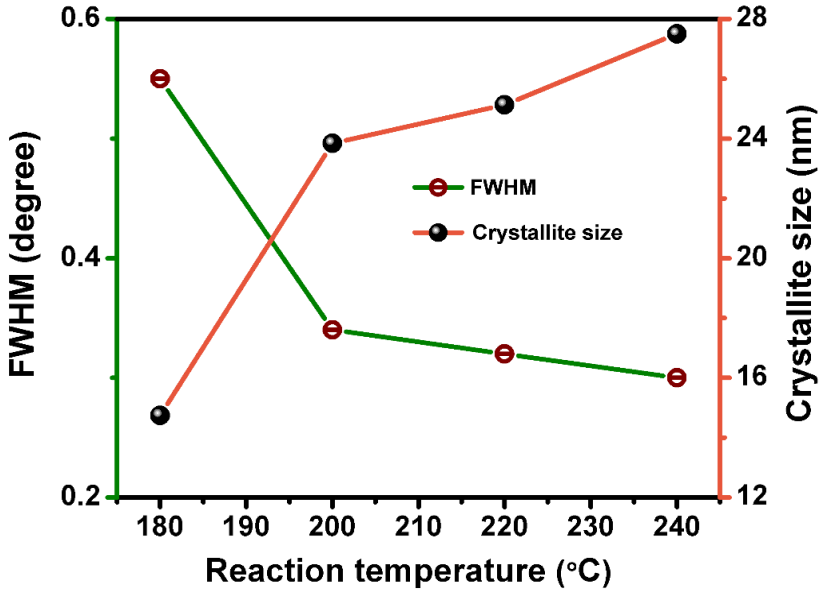

Fig.6.2. Changes in FWHM and crystallite size as a function of reaction temperature.

6.1.1.2 Morphological and compositional properties

From the FE-SEM images (Fig.6.3), homogeneous size of the particles was observed at 220°C as compared to other temperatures. The size of the CZTS Nps increased from 15 to 35 nm with increases in the reaction temperature. The elemental compositions of CZTS Nps are examined using EDAX analysis. The elemental compositions and compositional ratios of Cu/(Zn+Sn) and Zn/Sn are shown in Fig. 6.4. The elemental composition was varied with increasing reaction temperature as shown in Fig. 6.4(a). The amount of Cu decreases while the amount of S increases with increases in the reaction temperature. The Cu- and Sn- rich composition was obtained, when the temperature less than 220°C. The Cu/(Zn+Sn) ratio decreases while Zn/Sn ratio increases as a function of reaction temperature as can be seen in Fig. 6.4(b). These compositional changes led to form Cu_2S and CTS phases at low reaction temperatures (180 to 200°C) as we observed in the structural analysis. When the reaction temperature increased to 220°C, Cu-poor, Zn-rich composition of CZTS was obtained which is beneficial

for solar cell applications [6]. From the structural, morphological and compositional analysis, we conclude that 220°C is the optimum temperature to get pure phase CZTS with Cu-poor, Zn-rich composition.

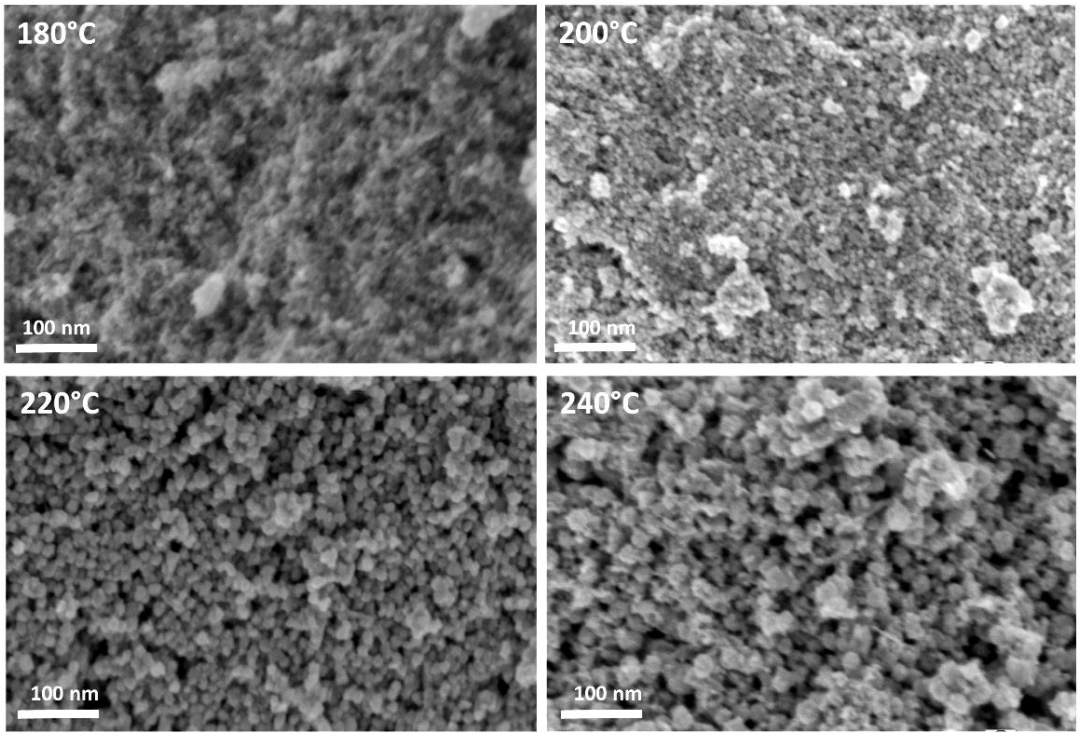

Fig.6.3. FE-SEM images of CZTS Nps synthesized at different reaction temperature.

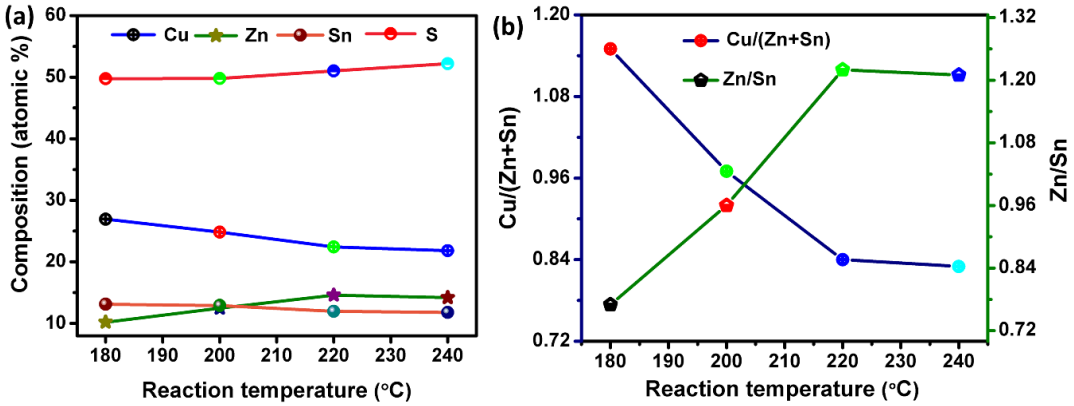

Fig.6.4. (a) The elemental composition and (b) the corresponding ratio of Cu/(Zn + Sn) and Zn/Sn of the CZTS Nps with different reaction temperature.

6.1.2 Influence of reaction time

6.1.2.1 Structural properties

To study the growth mechanism of the CZTS Nps, aliquots were withdrawn at regular interval from the reaction mixture at 220°C which is the optimum temperature as mentioned in earlier. Fig. 6.5(a) shows the XRD patterns of CZTS Nps synthesized at different reaction time. From the spectra, (112), (020), (220) and (312) planes were observed, related to the kesterite crystal structure of CZTS (JCPDS 01-075-4122) for all the samples. When the reaction time less than 1 h, Cu_2S peak was observed. As can be seen in Fig. 6.6, FWHM decreased from 0.63 to 0.31°, which indicates the improvement in the crystallite and grain size. The crystallite size was calculated using the Scherrer formula. The calculated crystallite size increased from 12.88 to 26.43 nm with increases in the reaction time.

Raman measurements were further used to confirm the phase purity of the CZTS Nps. Raman spectra measurements of CZTS Nps for different reaction time are shown in Fig. 6.5(b). The spectra showed a prominent peak at around 334 cm^{-1} and two shoulder peaks at 286 and 374 cm^{-1} for all the samples, correspond to kesterite crystal structure of CZTS [2]. In addition to that, a secondary phase of Cu_2S peak was observed at 474 cm^{-1} [3] for the sample synthesized between 10 and 30 mins. The CTS phase observed at 297 cm^{-1} for 1 h. When the reaction time between 2 and 4 h, pure phase kesterite CZTS was obtained. Therefore, the structural analysis suggested that pure phase of CZTS evolved from Cu_2S, then to CTS intermediate compound, finally to kesterite CZTS Nps.

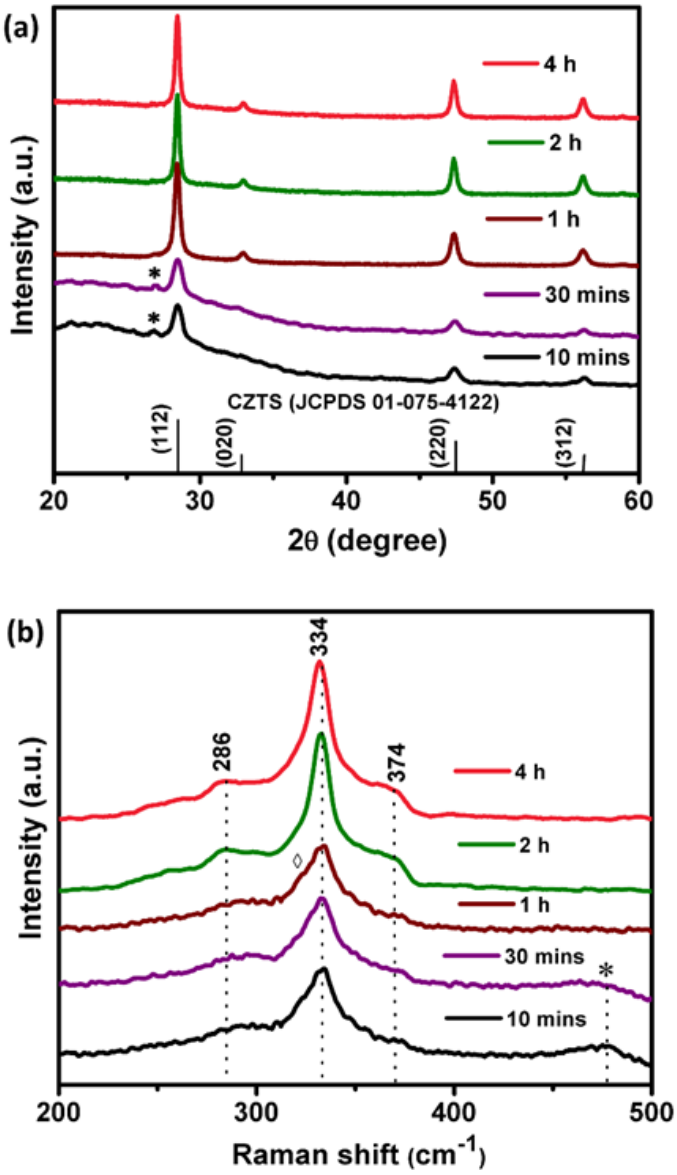

Fig.6.5. (a) XRD pattern and (b) Raman spectra of CZTS Nps synthesized at 220°C for different reaction time.

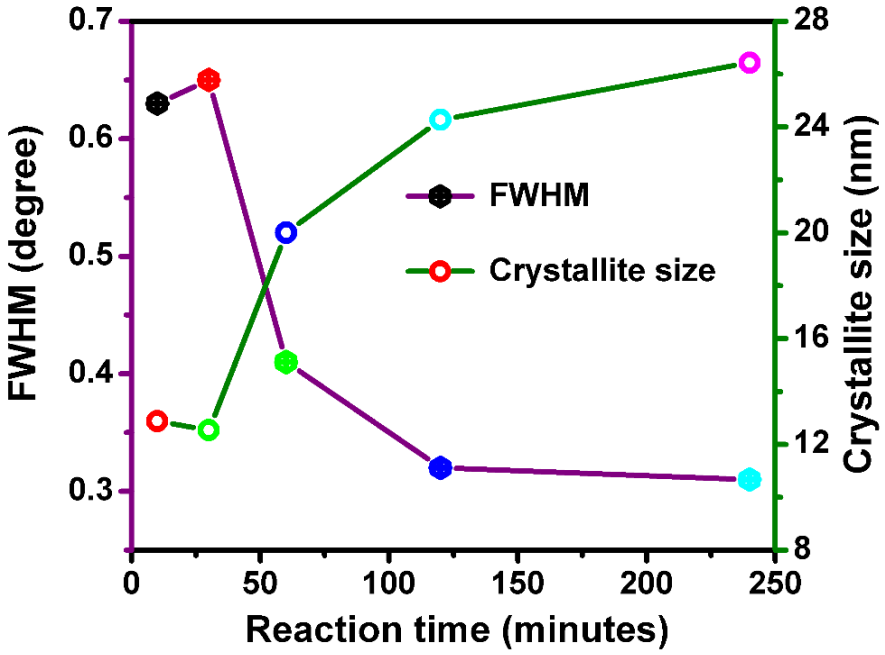

Fig.6.6. Variation in FWHM and crystallite size as a function of reaction time.

6.1.2.2 Morphological and compositional properties

The time-dependent evolution of morphology was obtained by TEM. As can be seen in Fig. 6.7, the Nps were formed even at 10 mins which indicates a fast reaction rate. The polydispersity of the Nps was observed for 30 mins and 1 h with size ranging from 10 to 35 nm.

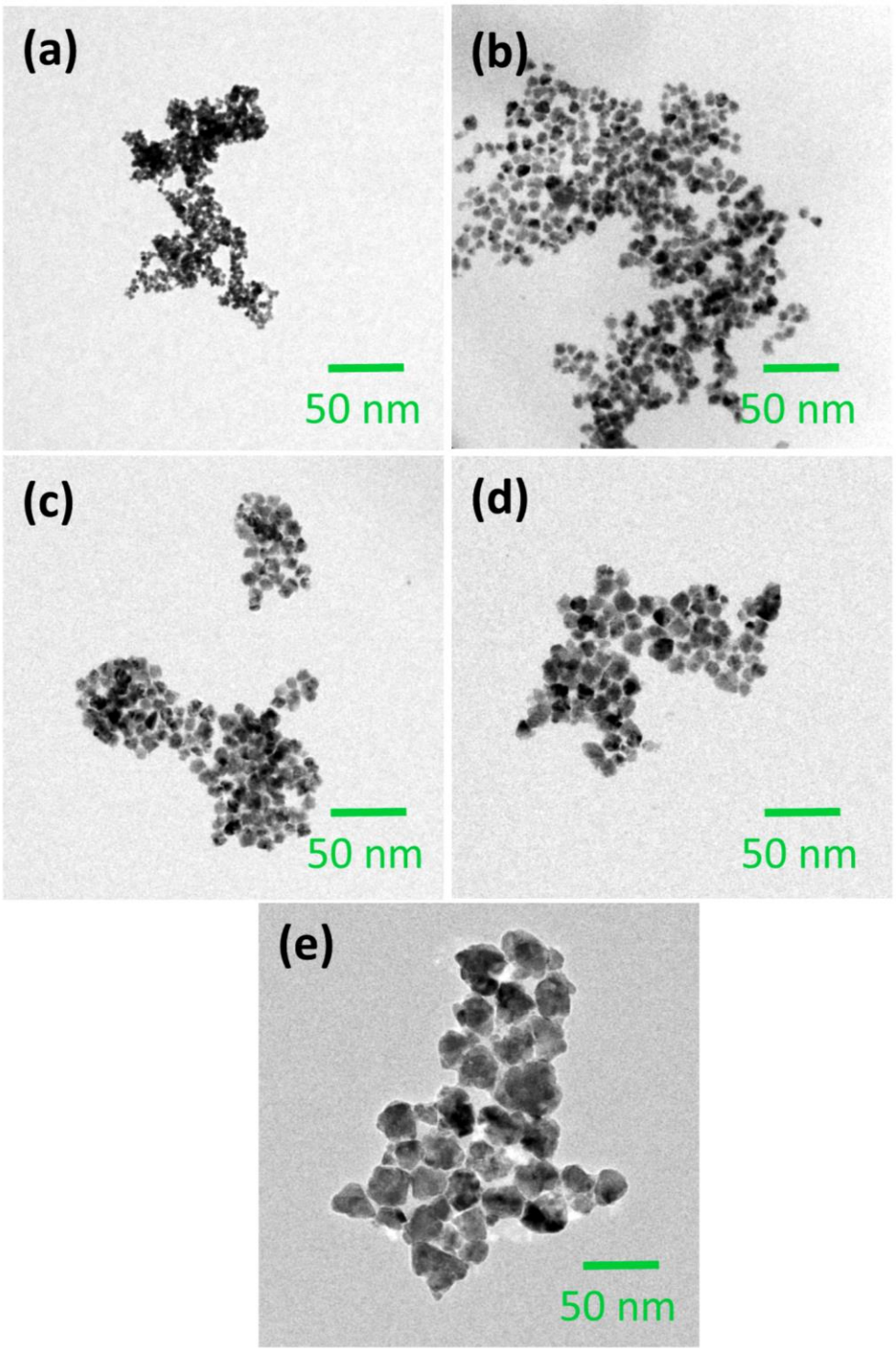

Fig.6.7. TEM images of CZTS Nps synthesized at 220°C for different reaction time: (a) 10 mins, (b) 30 mins, (c) 1 h, (d) 2 h and (e) 4 h.

When the reaction time increases up to 2 h, the homogeneous size of the particles was obtained as compared to other reaction times and the particles size is at around 20 nm. Further, increase the reaction time up to 4 h, particle size increased up to 35 nm. As a result, particle sizes increased with respect of reaction time, could be due to Ostwald ripening. The elemental compositions and compositional ratios of Cu/(Zn+Sn) and Zn/Sn are shown in Fig. 6.8. With increases in the reaction time, the elemental composition was varied as shown in Fig. 6.8(a). The amount of S increases while the amount of Cu decreases as the reaction proceeds. When the reaction time less than 1 h, Cu- and Sn-rich composition was observed. The Cu/(Zn+Sn) decreased while Zn/Sn ratio increased as the reaction proceeds. Because of these compositional changes, secondary and ternary phases of Cu_2S and CTS were seen in the structural analysis. Further increasing the reaction time to 2 h, Cu-poor, Zn-rich composition was obtained which is very close to the targeted value of $Cu_{1.79}Zn_{1.16}Sn_{0.95}S_{4.08}$.

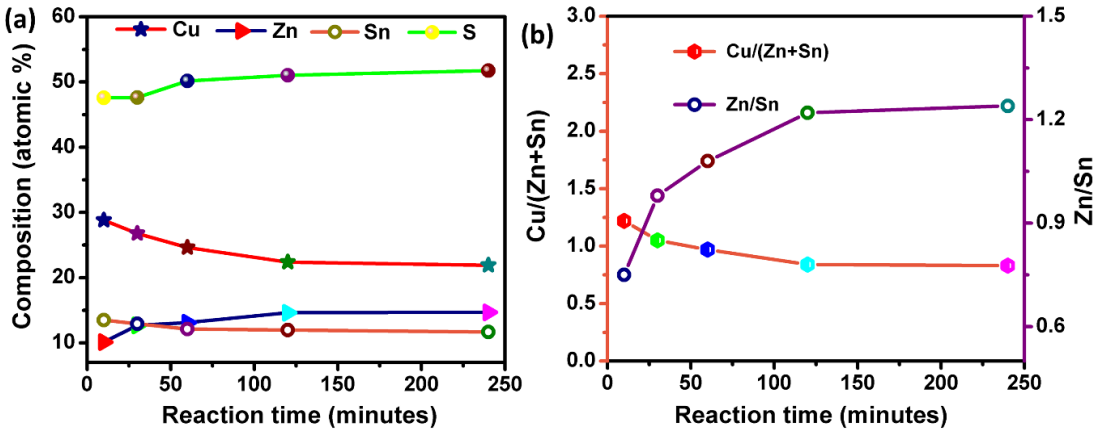

Fig.6.8. (a) The elemental composition and (b) the corresponding ratio of Cu/(Zn + Sn) and Zn/Sn of the CZTS Nps synthesized at 220°C for different reaction time.

FE-SEM-EDAX elemental mappings are performed for CZTS Nps synthesized at 2 h. From the Fig. 6.9, we could observe that Cu, Zn, Sn and S elements were consistently spread in the selected area of the Nps. These results, suggested that the nanoparticles have a uniform composition without existence of compositional gradients.

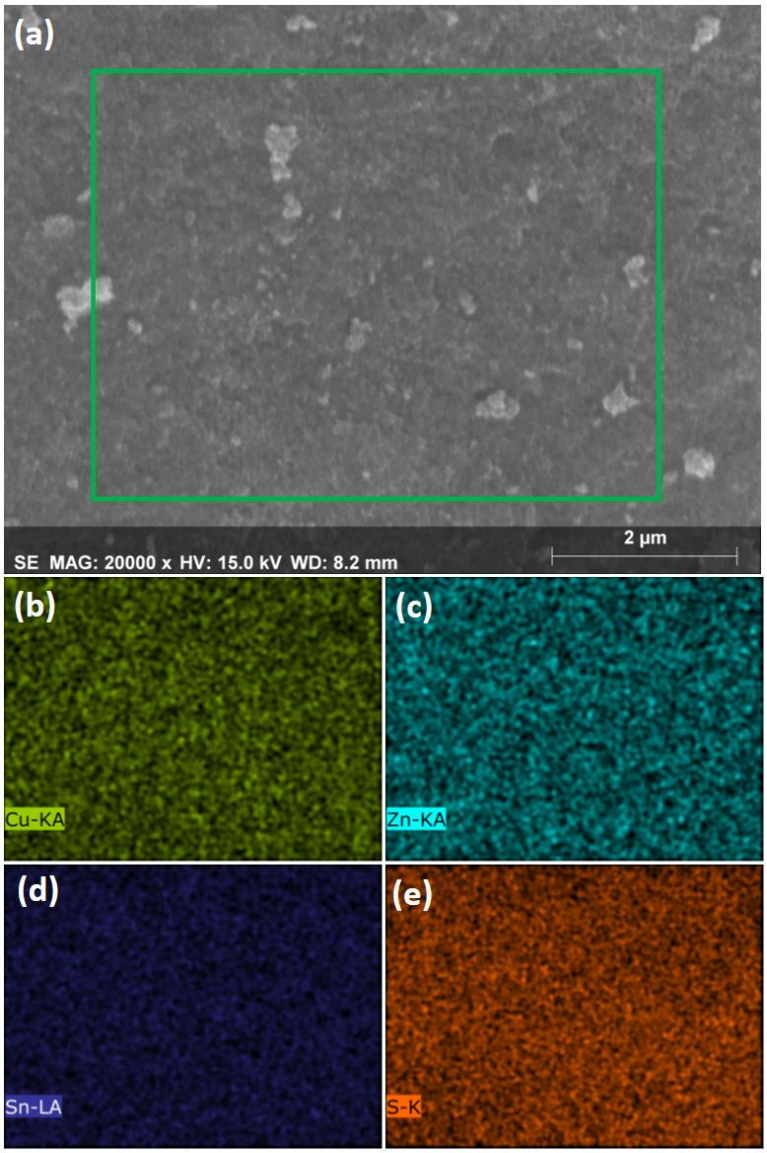

Fig.6.9. (a) FE-SEM-EDAX image of the selected area, (b-e) elemental mapping of Cu, Zn, Sn and S respectively.

6.1.2.3 Optical properties

Fig. 6.10(a) exhibits the UV-VIS-NIR absorption spectra of the CZTS Nps for 2 h. The obtained CZTS Nps presented a strong optical absorption in the visible region. The optical band gap E_g was estimated using the formula as described in the chapter 4 (equation 4.2). The optical band gap was obtained by plotting $(\alpha h\upsilon)^2$ as a function of $h\upsilon$ as shown in Fig. 6.10(b). The calculated band gap was found to be 1.52 eV which is well consistent with the literature values [7,8].

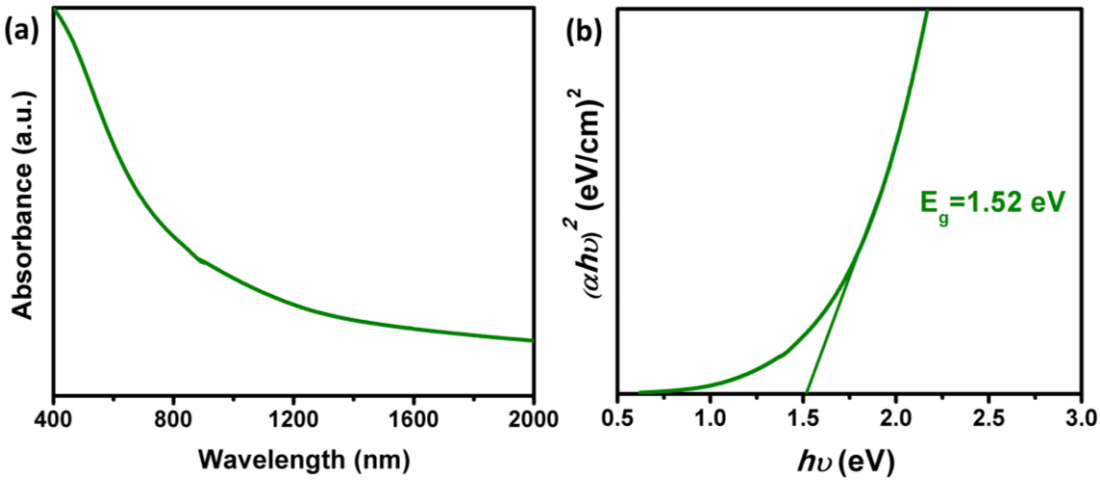

Fig.6.10. (a) UV-Vis-NIR absorption spectrum and (b) corresponding band gap of CZTS Nps synthesized at 2 h.

To study the valence states of all four elements in the synthesized CZTS Nps, XPS analysis was performed for the optimized reaction time of 2 h. As can be seen in Fig. 6.11(a-d), XPS analysis exhibits the presence of Cu 2p, Zn 2p, Sn 3d and S 2p elements in the CZTS Nps. The Cu 2p spectrum illustrates two peaks at 952.12 and 932.20 eV with a splitting of 19.92 eV, correspond to Cu(I). The Zn 2p peaks located at 1046.10 and 1022.99 eV with a split orbit of 23.11 eV, attributed to Zn(II). The Sn 3d peaks appeared at 496.10 and 487.64 eV with a split orbit of 8.46 eV, represents Sn (IV). The S 2p peaks revealed binding

energies at 162.30 and 161.20 eV with a split orbit of 1.10 eV, which is in good agreement with the binding energy of S in the sulfide state in CZTS. These results were well consistent with the reported values of the binding state of the elements of CZTS [9–12].

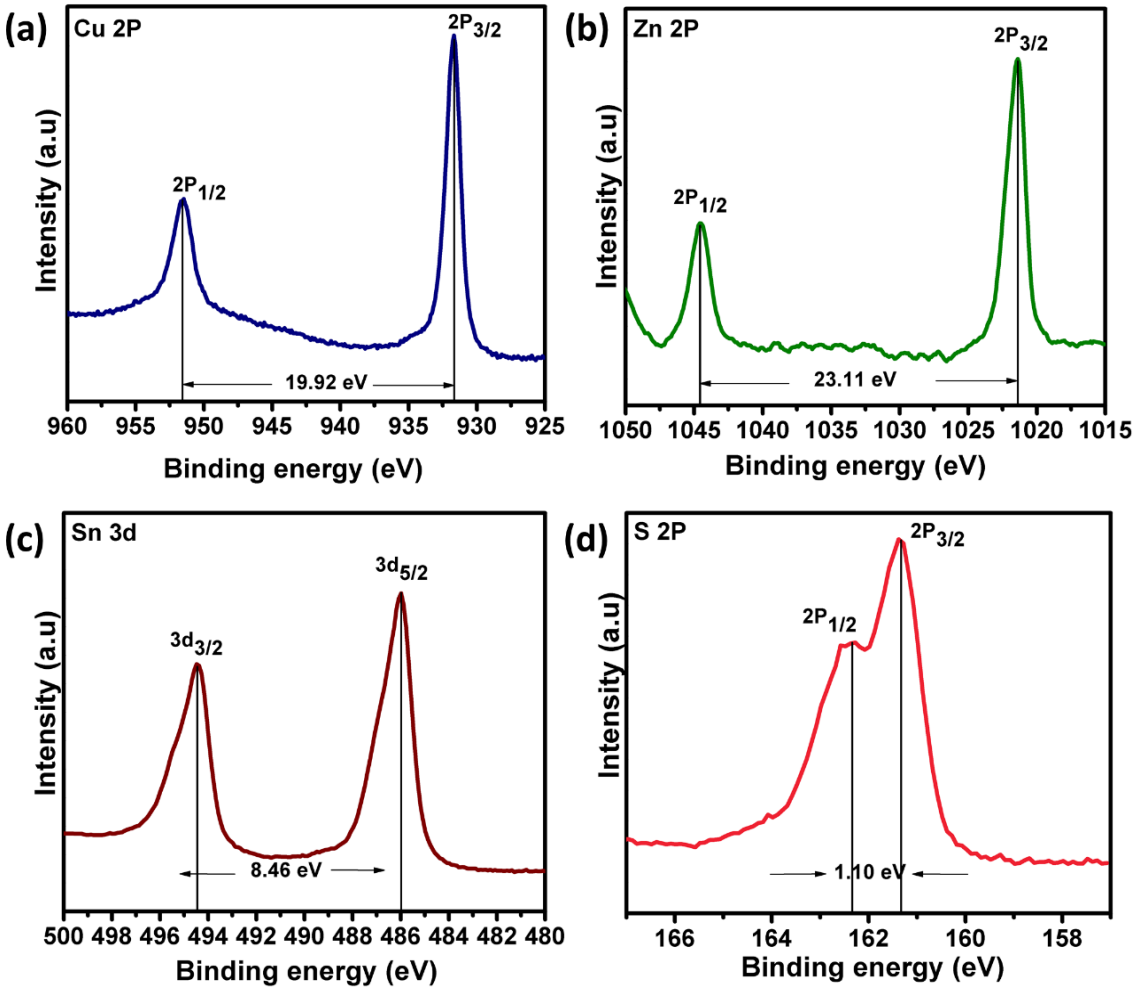

Fig.6.11. (a-d) XPS spectra of CZTS Nps for 4 h: Cu 2P, Zn 2P, Sn 3d, and S 2p respectively.

6.1.2.4. Growth and formation mechanism

On the basis of above results, a possible growth mechanism was proposed for the CZTS Nps prepared by hot-injection process as shown in Fig. 6.12. The evolution pathway of pure phase CZTS Nps was explained as follows:

(a) Firstly, Cu_2S nuclei was formed.

(b) Then, CTS formation was observed by the incorporation of Sn^{4+} ions into Cu_2S nuclei.

(c) Finally, the pure phase of CZTS Nps was obtained followed by diffusion of Zn^{2+} cations into CTS.

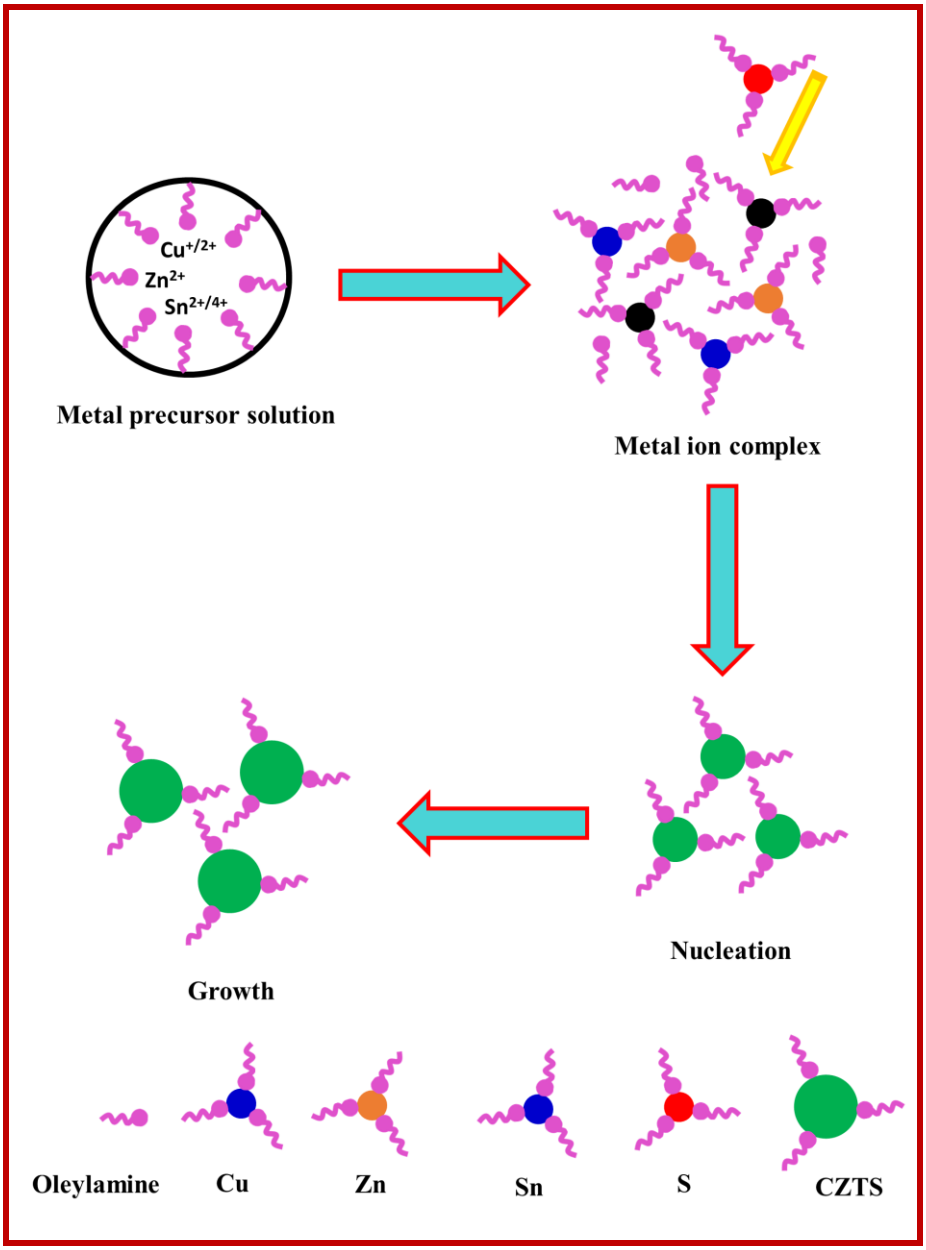

Fig. 6.12. Evolution pathway of CZTS Nps synthesized by hot-injection process.

The Cu_2S phase observed at less reaction times from 10 to 30 mins, which could be due to the Cu-rich composition as can be seen in the Fig. 6.8(a). The Cu ions in Cu_2S have relatively high mobility, which can facilitate an exchange with other metal ions as the reaction proceeds. When the reaction time increased to 1 h, Sn^{4+} was gradually incorporated into the Cu_2S crystal lattice to form the intermediate compound of Cu–Sn–S. This behavior could be evident from Cu/(Zn+Sn) ratio evolutions (Fig. 6.8(b)) and structural analysis (Fig. 6.5). Consequently, the diffusion of Zn^{2+} into Cu–Sn–S nanoparticles to form the CZTS Nps. When the reaction time increased to 2 h, the targeted composition was obtained. Morphology analysis showed homogeneous size of the particles at 2 h as compared to less reaction times. Further increasing reaction time up to 4 h, a significant difference was not observed. Hence, the results revealed that 2 h is the optimum time to get pure phase kesterite CZTS Nps with controlled composition and homogeneous particles size.

6.2. Deposition of CZTS films

Based on the above results, the optimum powder conditions (220°C for 2 h) were used for further film deposition. The CZTS ink was formulated using the optimized powder concentration of 0.05 g nanopowders in 1 mL hexanethiol as we discussed in the chapter 5. Then, the CZTS ink was coated onto SLG substrate by doctor blade method as mentioned in chapter 3.

6.2.1 Properties of annealed and selenized films

The prepared CZTS films are annealed at 350^0C and selenized at 550^0C, which are the optimum parameters as we discussed in chapter 5.

Fig. 6.13(a) shows the XRD patterns of annealed and selenized CZTS films. From the XRD pattern, the (112), (220) and (312) planes were observed for annealed film which is similar to the powder. After selenization, the peaks were shifted to lower 2θ values. The peak shift is due to the replacement of the

majority of smaller sized sulfur atoms (0.184 nm) by larger sized selenium (0.198 nm) atoms during the selenization process which increases the lattice parameters [13,14]. As can be seen in Fig. 6.13(b), Raman peaks were observed at 335, 286 and 372 cm^{-1} for CZTS films, agreeing well with the powder samples (Fig. 6.5(b)). The selenized film exhibits the A_1 mode shift of CZTSe at 171, 193 and 242 cm^{-1} which are consistent with the literature [15–17]. From the Raman spectra, secondary phases like Cu_2S, ZnS, ZnSe, CTS etc., were not observed. Thus, the results confirmed that the formation of pure phase CZTSSe.

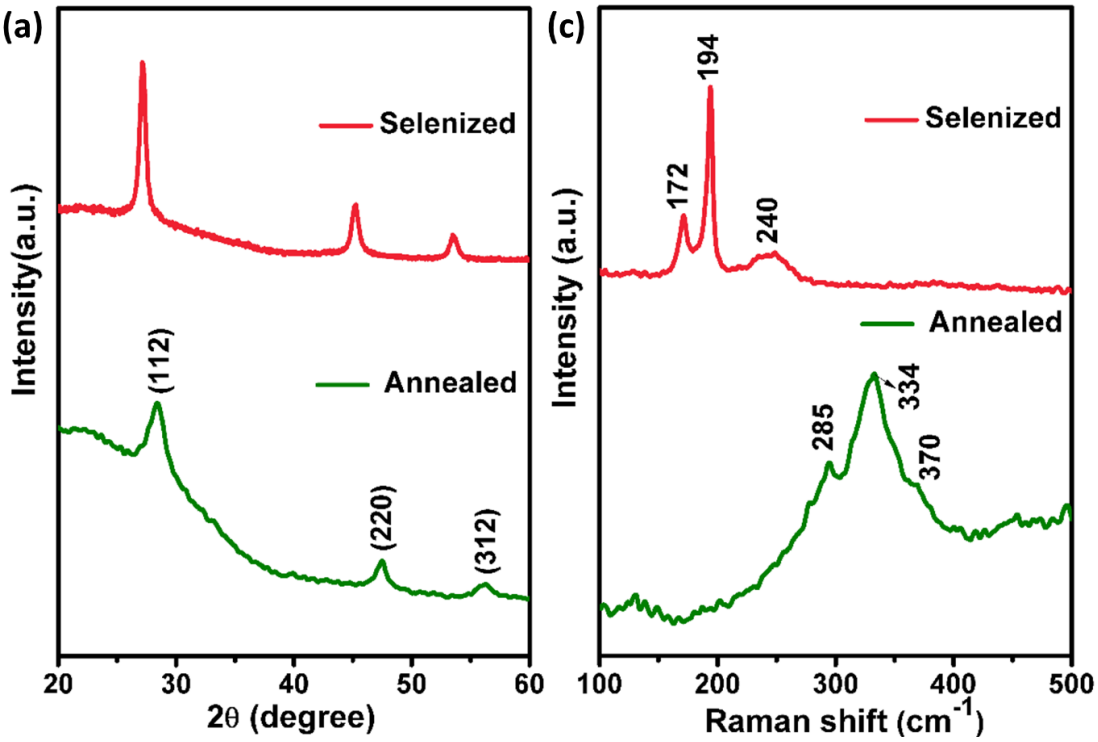

Fig.6.13. (a) XRD pattern, (b) Raman spectra of annealed and selenized films.

FE-SEM images of annealed and selenized films are shown in Fig. 6.14. The planar view of CZTS film shows a smooth surface and similar composition to the powder (Fig. 6.8(a)). CZTS films were selenized under selenium atmosphere to improve the properties of the film. After selenization, crack-free and slight increment in the grain size of the film was obtained. From the cross-

sectional image, densely packed grains of CZTSSe film was observed with uniform thickness of ~3 μm. The thickness of the film increased from 2 to 3 μm which could be due to the volume expansion in the unit cell as the smaller sized sulfur is replaced by larger sized selenium atoms. After selenization, the sulfur content decreased while selenium increased. As well, the carbon content decreased from 43.12 to 32.53 (atomic %) as can be seen in table 6.1. Furthermore, the selenized film revealed the Cu-poor, Zn-rich composition which is suitable for solar cell applications.

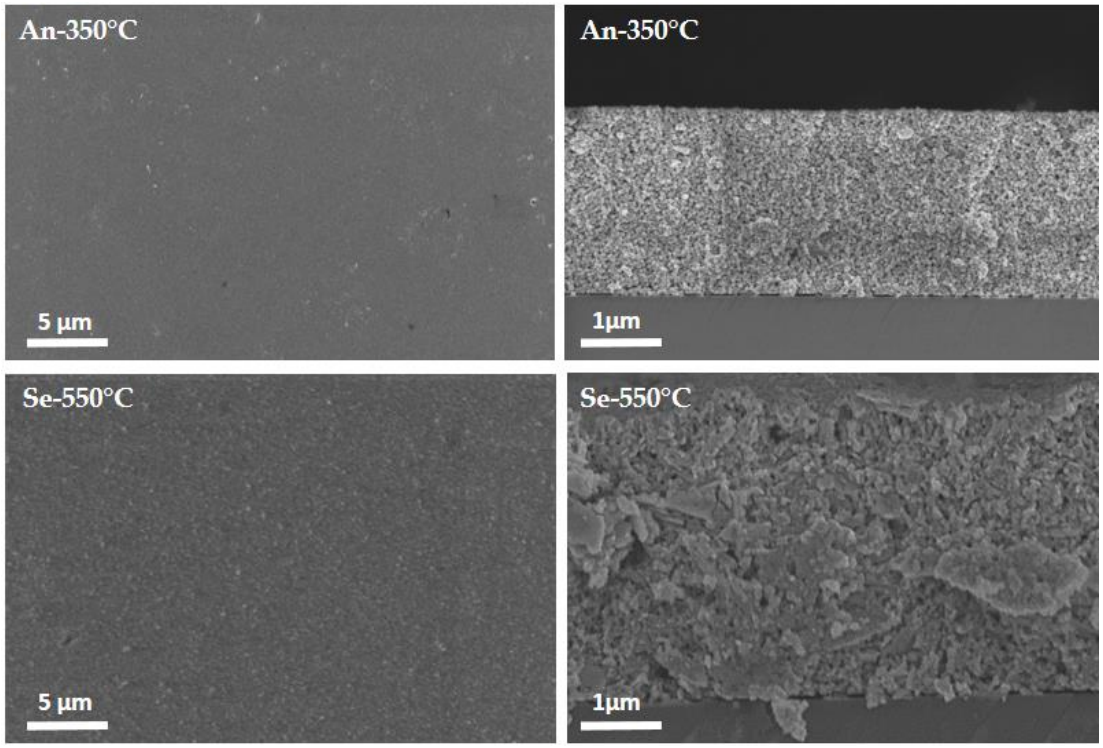

Fig.6.14. Planar and cross-sectional images of annealed and selenized films.

Table 6.1. EDAX compositional analysis of annealed and selenized films.

Film conditions	EDAX								
	Cu	Zn	Sn	S	Se	Cu/ (Zn+Sn)	Zn/ Sn	Se/ (S+Se)	C
Annealed	21.98	14.22	12.25	51.55	-	0.83	1.15	-	43.12
Selenized	19.83	13.13	11.32	4.19	51.53	0.81	1.16	0.92	32.53

UV-Vis-NIR absorbance spectra measurements were performed for annealed and selenized films as can be seen in Fig. 6.15. The optical band gap was calculated using Tuac's relation as described in the equation (4.2). The estimated band gap energy of annealed CZTS film is 1.50 eV. The band gap energy decreased from 1.52 to 1.16 eV for CZTSSe film. These values were matches well with the reported values [18–20]. The replacement of the sulfur atoms by selenium atoms in the film results in the narrow band gap energy of the CZTSSe film.

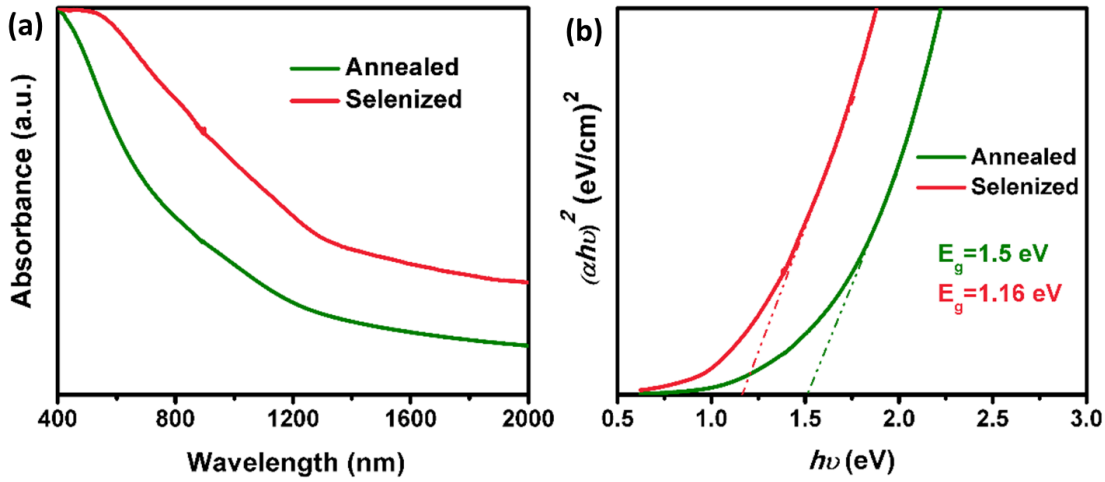

Fig.6.15. (a) UV-Vis-NIR absorption spectra and (b) corresponding band gap of annealed and selenized films.

The conductivity type, carrier concentration, mobility and resistivity of annealed and selenized films were measured by Hall-effect. The reported value

of mobility and carrier concentration for CZTS absorber material are in the range of 1 to 10 $cm^2.V^{-1}.s^{-1}$ and 10^{16} to 10^{18} cm^{-3} [21–23]. As can be seen in table 6.2, the annealed and selenized films revealed P-type conductivity. Compared to annealed film, the carrier concentration and mobility were increased while resistivity decreased for the selenized films. After selenization, slight increment in the grain size was observed as compared to annealed film, which could enhance the carrier concentration and mobility of the film.

Table 6.2. Electrical properties of annealed and selenized films measured using Hall Effect measurement system.

Experimental conditions	Type of conductivity	Carrier concentration (cm^{-3})	Mobility (cm^2/Vs)	Resistivity (Ωcm)
Annealed	P	3.12×10^{16}	0.04	145
Selenized	P	7.52×10^{17}	3.2	70

Fig. 6.16, shows I–V measurements of the annealed and selenized films under dark and illumination of light. Films exhibited linear I-V curves, due to ohmic nature of the metal contacts as reported by other researchers [21,24]. Photoconductivity of the films increased under an illumination of light as compared to dark conditions. This is because the lumination excites electrons from valence band to the conduction band. The photoconductivity of films can be expressed by ΔI (current difference in the dark and under illumination of light at a given bias voltage). The photocurrent ΔI is calculated by I_{photon}/I_{dark} for annealed and selenized films were 1.1 and 1.5 μA respectively. The selenized film exhibited higher photoconductivity than annealed film, could be due to slight increment in the grain size.

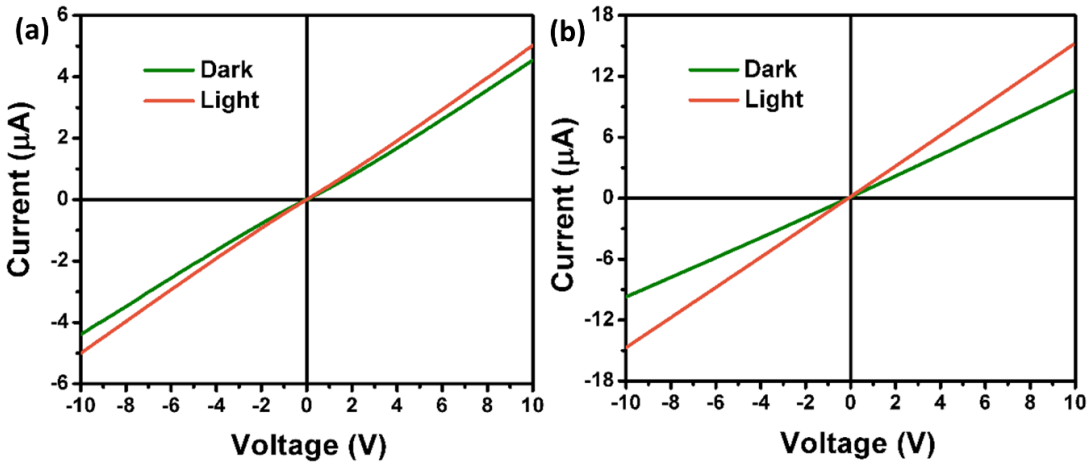

Fig.6.16. I-V characteristics of annealed and selenized films.

6.3. Summary

- CZTS Nps were synthesized under Cu-poor, Zn-rich conditions by hot-injection process. Reaction temperatures and time were varied to study their influences on the properties of Nps. Formation mechanism of the Nps were systematically investigated by examining their structural, morphological, compositional and optical properties.
- CZTS Nps were synthesized by changing the reaction temperatures from 180 to 240^{0}C for 2 h. From the structural analysis, secondary and ternary phases were observed at low reaction temperatures. As the reaction temperature increases, secondary and ternary phases dissappeared and pure phase of CZTS was observed at 220°C. Compositional analysis revealed Cu- and Sn-rich composition at low reaction temperatures which is consistent with the structural analysis where we observed Cu_2S and CTS. When the reaction temperature increased to 220°C, stoichiometric composition of CZTS was obtained which is close to the targeted value of $Cu_{1.79}Zn_{1.16}Sn_{0.95}S_{4.08}$. Morphological analysis showed homogeneous size of the particles at 220°C as compared to other temperatures. Based on the above results, we confirm that

220°C is the optimum temperature to get pure phase CZTS with the targeted composition.

- To study the growth mechanism of CZTS Nps, aliquots were taken at regular interval from 10 mins to 4 h. Structural analysis revealed the secondary phase of Cu_2S peak between 10 and 30 mins. Further increases in the reaction time, the intensity of the Cu_2S peak was decreased and pure phase kesterite CZTS was obtained at 2 h. The particle sizes were increased with increases in the reaction time because of Ostwald ripening. When the reaction time was less than 30 mins, Cu- and Sn-rich composition was observed. Further, increasing the reaction time to 2 h, Cu-poor, Zn-rich composition was obtained which is very close to the targeted value. Time-dependent experiments suggested that the phase conversion of CZTS occurs from Cu_2S through the Cu_2SnS_3 intermediate compound, finally to pure phase kesterite CZTS. These results suggested that 2 h is the optimum time to get pure phase CZTS Nps. Besides, the observed binding energies from the XPS analysis is well consistent with the literature. Optical analysis showed the band gap of 1.49 eV, suitable for solar cell applications.
- The optimum powder condition of 220°C for 2 h is further used for film preparation. The ink was formulated using 0.05 g of CZTS powders in 1 mL hexanethiol. Then, the ink was coated as a thin films by doctor blade method and annealed at 350°C for 1 min. The annealed films were selenized at 550°C for 15 mins.
- XRD analysis showed (112), (220) and (312) planes of kesterite CZTS for all the films. After selenization, the peaks were shifted to lower 2θ values, due to the replacement of majority of smaller sized sulfur atoms by larger sized selenium atoms. Besides, Raman spectra showed the peak shift towards lower wavenumber after selenization. Morphological analysis showed crack free

surface for both annealed and selenized films. After selenization, slight improvement in the grain size was observed. The thickness of the film increased from 2 to 3 μm which could be due to the volume expansion in the unit cell as the sulfur is replaced by selenium atoms. After selenization, the carbon content was decreased from 43.12 to 32.53 (atomic %). Moreover, the selenized film showed Cu-poor, Zn-rich composition which is optimal for solar cell applications. The band gap energy decreased from 1.52 to 1.16 eV for selenized film. Besides, the carrier concentration and mobility were increased. The higher photoconductivity was observed for CZTSSe film than CZTS, could be due to an improvement in the grain size.

References

[1] V.T. Tiong, J. Bell, H. Wang, One-step synthesis of high quality kesterite Cu_2ZnSnS_4 nanocrystals - a hydrothermal approach, Beilstein Journal of Nanotechnology. 5 (2014) 438–446. doi:10.3762/bjnano.5.51.

[2] R. Saravana Kumar, B.D. Ryu, S. Chandramohan, J.K. Seol, S.K. Lee, C.H. Hong, Rapid synthesis of sphere-like Cu_2ZnSnS_4 microparticles by microwave irradiation, Materials Letters. 86 (2012) 174–177. doi:10.1016/j.matlet.2012.07.059.

[3] M. Zhou, Y. Gong, J. Xu, G. Fang, Q. Xu, J. Dong, Colloidal CZTS nanoparticles and films: Preparation and characterization, Journal of Alloys and Compounds. 574 (2013) 272–277. doi:10.1016/j.jallcom.2013.05.143.

[4] J. Han, S.W. Shin, M.G. Gang, J.H. Kim, J.Y. Lee, Crystallization behaviour of co-sputtered Cu_2ZnSnS_4 precursor prepared by sequential sulfurization processes., Nanotechnology. 24 (2013) 95706. doi:10.1088/0957-4484/24/9/095706.

[5] V.T. Tiong, Y. Zhang, J. Bell, H. Wang, Phase-selective hydrothermal synthesis of Cu_2ZnSnS_4 nanocrystals: the effect of the sulphur precursor, CrystEngComm. 16 (2014) 4306–4313. doi:10.1039/C3CE42606H.

[6] H. Chen, Q. Ye, X. He, J. Ding, Y. Zhang, J. Han, J. Liu, C. Liao, J. Mei, W. Lau, Electrodeposited CZTS solar cells from Reline electrolyte, Green Chemistry. 16 (2014) 3841. doi:10.1039/C4GC00142G.

[7] X. Wang, Z. Sun, C. Shao, D.M. Boye, J. Zhao, A facile and general approach to polynary semiconductor nanocrystals via a modified two-phase method., Nanotechnology. 22 (2011) 245605. doi:10.1088/0957-4484/22/24/245605.

[8] Q. Guo, H.W. Hillhouse, R. Agrawal, Synthesis of Cu_2ZnSnS_4 nanocrystal

ink and its use for solar cells, Journal of the American Chemical Society. 131 (2009) 11672–11673. doi:10.1021/ja904981r.

[9] S. Zhang, C. Wang, L. Sun, A. Lu, X. Xu, H. Xing, X. Chen, Fabrication of single-crystal/phase Cu_2ZnSnS_4 nanorods via a two-step spin coating route, Applied Physics Express. 8 (2015). doi:10.7567/APEX.8.035202.

[10] M.D. Regulacio, C. Ye, S.H. Lim, M. Bosman, E. Ye, S. Chen, Q.H. Xu, M.Y. Han, Colloidal nanocrystals of wurtzite-type Cu_2ZnSnS_4: Facile noninjection synthesis and formation mechanism, Chemistry - A European Journal. 18 (2012) 3127–3131. doi:10.1002/chem.201103635.

[11] M. Li, W.H. Zhou, J. Guo, Y.L. Zhou, Z.L. Hou, J. Jiao, Z.J. Zhou, Z.L. Du, S.X. Wu, Synthesis of pure metastable wurtzite CZTS nanocrystals by facile one-pot method, Journal of Physical Chemistry C. 116 (2012) 26507–26516. doi:10.1021/jp307346k.

[12] W.C. Liu, B.L. Guo, X.S. Wu, F.M. Zhang, C.L. Mak, K.H. Wong, Facile hydrothermal synthesis of hydrotropic Cu_2ZnSnS_4 nanocrystal quantum dots: band-gap engineering and phonon confinement effect, Journal of Materials Chemistry A. 1 (2013) 3182–3186. doi:10.1039/c3ta00357d.

[13] K. V. Gurav, S.W. Shin, U.M. Patil, M.P. Suryawanshi, S.M. Pawar, M.G. Gang, S.A. Vanalakar, J.H. Yun, J.H. Kim, Improvement in the properties of CZTSSe thin films by selenizing single-step electrodeposited CZTS thin films, Journal of Alloys and Compounds. 631 (2015) 178–182. doi:10.1016/j.jallcom.2014.12.253.

[14] Z. Li, J.C.W. Ho, K.K. Lee, X. Zeng, T. Zhang, L.H. Wong, Y.M. Lam, Environmentally friendly solution route to kesterite $Cu_2ZnSn(S,Se)_4$ thin films for solar cell applications, RSC Advances. 4 (2014) 26888. doi:10.1039/c4ra03349c.

[15] X. Zeng, K.F. Tai, T. Zhang, C.W.J. Ho, X. Chen, A. Huan, T.C. Sum, L.H.

Wong, $Cu_2ZnSn(S,Se)_4$ kesterite solar cell with 5.1% efficiency using spray pyrolysis of aqueous precursor solution followed by selenization, Solar Energy Materials and Solar Cells. 124 (2014) 55–60. doi:10.1016/j.solmat.2014.01.029.

[16] J. Guo, Y. Pei, Z. Zhou, W. Zhou, D. Kou, S. Wu, Solution-Processed $Cu_2ZnSn(S,Se)_4$ Thin-Film Solar Cells Using Elemental Cu, Zn, Sn, S, and Se Powders as Source., Nanoscale Research Letters. 10 (2015) 1045. doi:10.1186/s11671-015-1045-6.

[17] D.B. Khadka, S.Y. Kim, J.H. Kim, Effects of Ge Alloying on Device Characteristics of Kesterite-Based CZTSSe Thin Film Solar Cells, Journal of Physical Chemistry C. 120 (2016) 4251–4258. doi:10.1021/acs.jpcc.5b11594.

[18] Y. Sun, Y. Zhang, H. Wang, M. Xie, K. Zong, H. Zheng, Y. Shu, J. Liu, H. Yan, M. Zhu, W. Lau, Novel non-hydrazine solution processing of earth-abundant $Cu_2ZnSn(S,Se)_4$ absorbers for thin-film solar cells, Journal of Materials Chemistry A. 1 (2013) 6880–6887. doi:10.1039/c3ta10566k.

[19] F. Liu, F. Zeng, N. Song, L. Jiang, Z. Han, Z. Su, C. Yan, X. Wen, X. Hao, Y. Liu, Kesterite $Cu_2ZnSn(S,Se)_4$ Solar Cells with beyond 8% Efficiency by a Sol-Gel and Selenization Process, ACS Applied Materials and Interfaces. 7 (2015) 14376–14383. doi:10.1021/acsami.5b01151.

[20] V.G. Rajeshmon, C.S. Kartha, K.P. Vijayakumar, C. Sanjeeviraja, T. Abe, Y. Kashiwaba, Role of precursor solution in controlling the opto-electronic properties of spray pyrolysed Cu_2ZnSnS_4 thin films, Solar Energy. 85 (2011) 249–255. doi:10.1016/j.solener.2010.12.005.

[21] N. Muhunthan, O.P. Singh, V.N. Singh, Growth of CZTS by co-sputtering and sulfurization for solar cell applications, SPIE Micro+Nano Materials, Devices, and Applications. 8923 (2013) 89232H. doi:10.1117/12.2032433.

[22] T. Tanaka, T. Nagatomo, D. Kawasaki, M. Nishio, Q. Guo, A. Wakahara, A.

Yoshida, H. Ogawa, Preparation of Cu_2ZnSnS_4 thin films by hybrid sputtering, Journal of Physics and Chemistry of Solids. 66 (2005) 1978–1981. doi:10.1016/j.jpcs.2005.09.037.

[23] B. Ananthoju, A. Kushwaha, F.J. Sonia, M. Aslam, Structural and optical properties of electrochemically grown highly crystalline Cu_2ZnSnS_4 (CZTS) thin films, AIP Conference Proceedings. 1512 (2013) 706–707. doi:10.1063/1.4791233.

[24] S. Sarkar, K. Bhattacharjee, G.C. Das, K.K. Chattopadhyay, Self-sacrificial template directed hydrothermal route to kesterite-Cu_2ZnSnS_4 microspheres and study of their photo response properties, CrystEngComm. 16 (2014) 2634. doi:10.1039/c3ce42229a.

Chapter 7
Conclusions

- The aim of the work presented in this thesis, towards preparation of CZTS films using Nps. CZTS Nps were synthesized by two different approaches such as heating-up and hot-injection. The ink was formulated using synthesized CZTS Nps to deposit films by doctor-blade method. Subsequently, annealing and selenization process were carried out to improve the properties of the film. Various properties were studied for CZTS Nps and films. Selenized films showed an improved structural, morphological, optical, and electrical properties as compared to annealed films.

- The stoichiometric and off-stoichiometric (Cu-poor, Zn-rich) CZTS Nps were synthesized by heating-up approach. It is found that both reaction temperature and time play a crucial role to obtain pure phase CZTS Nps with controlled composition. Time-dependent phase evolution and the formation mechanism of the kesterite CZTS Nps were systematically investigated by examining their structural, morphological, compositional and optical properties. Also, the time-dependent experiments revealed that the compositional phase evolved from Cu_2S through the intermediate Cu_2SnS_3 compound to finally form kesterite CZTS Nps. These results revealed that the optimum reaction temperature and time for pure phase CZTS Nps was found to be 220°C and 4 h respectively, as aforementioned in chapter 4. These optimum conditions were employed to synthesize Cu-poor, Zn-rich composition of CZTS Nps, which is one of the prime condition to achieve highly efficient CZTS solar cells. Furthermore, the ink was formulated using

Cu-poor, Zn-rich composition of Nps. Afterwards, the ink was coated as a thin film by doctor blade method followed by annealing. The CZTS powder concentrations were varied to accomplish crack free films. Annealing process was carried out to reduce the solvent and carbon content in the film. Selenization temperatures were varied to study the role of selenium on the film properties. After selenization, band gap was decreased from 1.5 to 1.09 eV, because of replacement of sulfur atoms by selenium atoms. Film selenized at 550°C, exhibited superior structural, morphological, optical and electrical properties.

- Using hot-injection approach, the Cu-poor, Zn-rich composition of CZTS Nps were synthesized. The reaction temperature and time were found to play a determining role to get pure phase CZTS with controlled composition. Hence, the sample synthesized at 220°C for 2 h, showed the pure phase kesterite CZTS Nps with the targeted composition. Consequently, these Nps were employed to prepare CZTS thin films. Moreover, annealing and selenization processes were performed to enhance the film properties. Selenized film exhibited a slight improvement in the photoconductivity. Therefore, the film prepared from heating-up approach revealed superior photoconductivity than hot-injection-approach. Moreover, heating-up approach is applicable for large scale production. Hence, the obtained CZTSSe films are suitable to be employed as an absorber layer in low-cost thin film solar cells.

Future work

- Deposition of CZTSSe film on Molybdenum substrate followed by annealing and selenization.
- To optimize the selenization parameters such as selenium content, selenium temperature and time to further enhance the grain growth.

- To complete the device structure of Mo/CZTSSe/CdS/ZnO/iZnO-Al.
- Study the device properties.

Publications and conference presentations

Publications

1. **R. Aruna Devi**, M. Latha, P. Reyes-Figueroa, M. Rohini, S. Velumani, Adolfo Tavira Fuentes, Miguel Galván Arellano F. Javier Ramírez Aponte and Jaime Santoyo-Salazar "Facile One Pot Synthesis of Single Phase Kesterite Cu_2ZnSnS_4 Nanocrystals" 10.1109/ICEEE.2016.7751250.
2. **R. Aruna Devi**, M. Latha, S. Velumani, Goldie Oza, P. Reyes-Figueroa, M. Rohini, I. G. Becerril-Juarez, Jae-Hyeong Lee and Junsin Yi "Synthesis and characterization of cadmium sulfide nanoparticles by chemical precipitation method" Journal of Nanoscience and Nanotechnology 15 (2015) 8434–8439.
3. M. Latha, **R. Aruna Devi**, S. Velumani, Goldie Oza, P. Reyes-Figueroa, M. Rohini, I. G. Becerril-Juarez, and Junsin Yi "Synthesis of $CuIn_{1-x}Ga_xSe_2$ Nanoparticles by Thermal Decomposition Method with Tunable Ga Content" Journal of Nanoscience and Nanotechnology 15 (2015) 8388–8394.
4. M. Latha, **R. Aruna Devi**, P. Reyes-Figueroa, M. Rohini, S. Velumani, Adolfo Tavira Fuentes, Miguel Galván Arellano and F. Javier Ramírez Aponte "Influence of Reaction Time on Cu(In,Ga)Se_2 Particles Synthesis by Thermal Decomposition Method". 10.1109/ICEEE.2016.7751251.
5. **R. Aruna Devi**, M. Latha, S. Velumani, Jaime Santoyo-Salazar, Quaternary kesterite Cu_2ZnSnS_4 nanocrystals synthesis by heating-up approach. **Submitted** to IOP Nanotechnology.
6. **R. Aruna Devi**, M. Latha, S. Velumani, F.A. Pulgarín, Osvaldo Vigil-Galán, José Álvaro Chávez Carvayar, Deposition and selenization of CZTS films by doctor blade method. **To be communicated.**

7. **R. Aruna Devi**, M. Latha, S. Velumani, Phase controlled synthesis of kesterite Cu_2ZnSnS_4 nanocrystals by hot-injection approach. **To be communicated.**

Oral and poster presentations

1. **R. Aruna Devi**, M. Latha, P. Reyes-Figueroa, M. Rohini, S. Velumani, Adolfo Tavira Fuentes, Miguel Galván Arellano F. Javier Ramírez Aponte and Jaime Santoyo-Salazar "Facile One Pot Synthesis of Single Phase Kesterite Cu_2ZnSnS_4 Nanocrystals" 13th International conference on Electrical Engineering, Computing Science and Automatic Control, September 26-30 2016, Mexico City, Mexico. (**Oral**)

2. **R. Aruna Devi**, M. Latha and S. Velumani "Tuning the Optical Properties of $Cu_2ZnSn(S,Se)_4$ Nanoparticles Synthesized by Hot Injection Method" MRS FALL MEETING & EXHIBIT, November 27 - December 2, 2016, Boston, Massachusetts. (**Oral**)
3. **R. Aruna Devi**, M. Latha, P. Reyes-Figueroa, M. Rohini, Goldie Oza and S. Velumani "OPTIMIZATION OF $Cu_2ZnSn(S,Se)_4$ THIN FILMS USING CZTS NANOPOWDERS BY KNIFE COATING METHOD" XXV International Materials Research Congress, IMRC 2016 August 14-19, Cancun, Mexico. (**Oral**)
4. **R. Aruna Devi**, M. Latha, P. Reyes-Figueroa, M. Rohini, Goldie Oza and S. Velumani "SYNTHESIS OF PRISTINE KESTERITE Cu_2ZnSnS_4 NANOPARTICLES BY HOT-INJECTION METHOD FOR SOLAR CELL APPLICATIONS" XXV International Materials Research Congress, IMRC 2016 August 14-19, Cancun, Mexico. (**Poster**)
5. **R. Aruna Devi**, M. Latha, Minha Kim, Donguk Kim, Wonkyu Chae, Jae-Hyeong Lee, Goldie Oza, Junsin Yi and S. Velumani "TIME DEPENDENT CZTS NANOCRYSTAL SYNTHESIS BY THERMAL DECOMPOSITION

METHOD" XXIV International Materials Research Congress, IMRC 2015 August 16-20, Cancun, Mexico. (**Poster**)

6. **R. Aruna Devi**, M. Latha, Minha Kim, Donguk Kim, Wonkyu Chae, Jae-Hyeong Lee, Goldie Oza, Junsin Yi and S. Velumani "SYNTHESIS AND CHARACTERIZATION OF CZTS NANOCRYSTALS BY THERMAL DECOMPOSITION METHOD" XXIV International Materials Research Congress, IMRC 2015 August 16-20, Cancun, Mexico. (**Poster**)
7. **R.Aruna Devi**, M. Latha, S. Velumani, I.G. Becerril-Juarez, Jae-Hyeong Lee, Donguk Kim, Wonkyu Chae, Minha Kim and Junsin Yi "SYNTHESIS AND CHARACTERIZATION OF CdS NANOPARTICLES BY CO-PRECIPITATION METHOD" Global Photovoltaic Conference, International Symposium on Photovoltaics (ISP 2014) November 10-11, BEXCO, Busan, Korea. (**Poster**)
8. **R. Aruna Devi**, M. Latha, S. Velumani, I. G. Becerril-Juarez, R. Asomoza and Junsin Yi "TIME DEPENDENT CdS NANOPARTICLE SYNTHESIS BY CHEMICAL PRECIPITATION METHOD" XXIII International Materials Research Congress, IMRC 2014, August 17-21, Cancun, Mexico. (**Oral**)
9. **R. Aruna Devi**, M. Latha, S. Velumani, I. G. Becerril-Juarez, R. Asomoza and Junsin Yi "EFFECT OF TEMPERATURE ON CdS NANOPARTICLES BY CO-PRECIPITATION METHOD" XXIII International Materials Research Congress, IMRC 2014, August 17-21, Cancun, Mexico. (**Poster**)
10. **R.Aruna Devi**, M.Latha, S.Velumani, I. G. Becerril-Juarez and Junsin Yi "SYNTHESIS AND CHARACTERIZATION OF CdS NANOPARTICLES BY CO-PRECIPITATION METHOD" International Conference on Microelectronics and Plasma Technology, ICMAP 2014, July 8-11, Gunsan, Korea. (**Poster**)